An Inverse Design Methodology for Long Last-Stage Steam Turbine Blades

Pietro Boselli

Department of Engineering

University College London

A thesis submitted for the degree of

Philosophiae Doctor

November 2014

Acknowledgements

I would like to express my gratitude to Professor Mehrdad Zangeneh for his supervision and support throughout the course of this project and is his ability to be encouraging at all times. He introduced me to research starting from my last year as an undergraduate, and I learned from him, directly or indirectly, all I know about turbomachinery design. His success as a professor and as a pioneer of commercial inverse design software has been an inspiration for my career in Engineering.
I would also like to sincerely thank Doctor Shigeki Senoo for his helpful advice during his visits, and for creating the opportunity of this project through the kind sponsorship provided by Hitachi Ltd. His genuine enthusiasm for research in the field of steam turbines has provided an example of how great design challenges should be tackled.
I feel privileged having shared my experience as a research student in the company of my colleagues in Roberts Building and Gower Street. In particular Wang Peng, who worked on his project at the same time as I did, and helped me mature my research skills thanks to consistent mutual support.
A final but nonetheless important and sincere expression of gratitude to my parents who always believed in what I did, and raised me with the will to achieve my aspirations.

Abstract

The last stage of an axial steam turbine is characterized by transonic flow and high volume flow rates. The resulting turbine blades are very large in size and complex in shape. This poses great design challenges, which last-stage blades are infamous for amongst steam turbine designers. Additionally, two-phase flows of condensing steam are always the case, and accurate numerical predictions of performance become often arduous.

Inverse design has been used for several years and with great success in a variety of turbomachinery applications. However, no specific inverse design strategy has been developed for large axial steam turbines, and last-stage blades in particular. The first requirement that comes to mind for a steam-turbine specific inverse method is the inclusion of two-phase effects. However, several other problems arise when dealing with the geometries typical of the last stage. The aim of this project is to identify and analyse the problems and requirements, and then develop some specific solutions which will allow the creation of a dedicated inverse design procedure. The first part of the project deals with a traditional inverse method and the inclusion of two-phase effects. The problems are then highlighted and two attempts are made to create a methodology that would work for last-stage blades. After devising a new way of describing blade profiles, the first method is introduced, based on a *transpiration* model. The second method is *circulation* based, and works through the prescription of circumferentially averaged swirl velocity. Finally, a design strategy is suggested for the whole redesign of a last stage rotor [1].

[1]The manufacturer of this rotor requested to be anonymous, and in many diagrams the dimensions have been posthumously removed for confidentiality

Contents

List of Figures

Nomenclature

Roman Symbols

a	Speed of sound
C	Generic control surface (curve in 2D)
c_p	Specific isobaric heat capacity
c_v	Specific isochoric heat capacity
E	Total energy (specific)
e	Total (internal) energy (specific)
$\mathbf{F}$	Generic flux vector of governing equations
G	Gibbs free energy
H	Total enthalpy (specific)
h	Computational cell area
h	Specific enthalpy (static)
$\mathbf{J}$	Generic source vector of governing equations
k_b	Ludwig Boltzmann's constant
Kn	Knudsen number
p	Pressure

T	Temperature
Pr	Prandtl number
$\mathbf{r}$	Generic parametric curve
r_*	Critical radius
S	Supersaturation ratio
s	Specific entropy
$\mathbf{U}$	Generic solution vector of governing equations
U	Blade speed
u	x-component of velocity
u	Specific internal energy
v	y-component of velocity
v	Specific volume
w	Speed of sound
y	Water liquid mass fraction

Greek Symbols

α_r	Heat transfer coefficient for droplet of radius r
β	Coefficient of thermal expansion
Ω	Generic control volume (surface in 2D)
γ	Dimensionless Gibbs free energy
γ	Specific heat ratio
κ	Coefficient of compressibility
λ	Mean free path of a vapour molecule

μ Dynamic viscosity

ω Blade angular speed

ϕ Potential function

π Reduced pressure $\pi = P/P^*$, reducing quantity varies (see IF97 [2007])

ψ Stream function

ρ Density

σ Liquid surface tension

θ Isothermal correction factor

θ Inverse reduced temperature $\theta = T^*/T$

Subscripts

0 Stagnation values

f Saturated liquid

g Gas phase

g Saturated gas

k Values at computational cell sides (faces in 3D)

l Liquid phase

s Saturation value

Acronyms

CD Convergent-Divergent

CFD Computational fluid dynamics

LE Leading edge

LP Low pressure

LSB Last stage blade

$NINT$ Nearest integer

ODE Ordinary Differential Equation

TE Leading edge

Chapter 1

Last-stage steam turbine blades: overview of design challenges

1.1 Introduction

Steam turbines are employed in a variety of power generating applications, most notably coal-fired power plants, nuclear power plants and in the combined power cycle. Figure 1.1 shows the world's total electricity production by fuel. Coal and nuclear alone provide 50% of the electrical power in the world, and considering that a large share of the old gas and oil power stations are being upgraded or replaced with combined cycle plants, steam turbines become relevant to over 60% of power generation in the world. The current project deals specifically with the last stage of the low pressure (LP) turbine which, as will be elucidated later, has very similar design requirements in all the above power cycles, since the boiler technology tends to affect more the high (HP) and intermediate pressure (IP) turbines. Even more specifically, the focus of the present research will be on LP turbine technology intended for employment in modern ultra-supercritical coal-fired power plants. Coal is at present the primary fuel for electricity production, with a share of almost 40% of the total. Furthermore it is the fossil fuel with the highest reserve to production (R/P) ratio across the world as shown in figure 1.2, while figure 1.3 reveals that the majority of the reserves are distributed evenly across the most heavily industrialized parts of the world, making coal a very

attractive option for electricity production for years to come. This places even more pressure into making coal-fired power plants an acceptable option under an environmental sustainability viewpoint. It is therefore essential to maximise their efficiency in order to reduce CO_2 emissions substantially. The tendency in modern coal-fired power plants is to increase thermal efficiency by increasing the average temperature at which heat is transferred to the steam, which results in achieving supercritical steam at the HP turbine inlet.

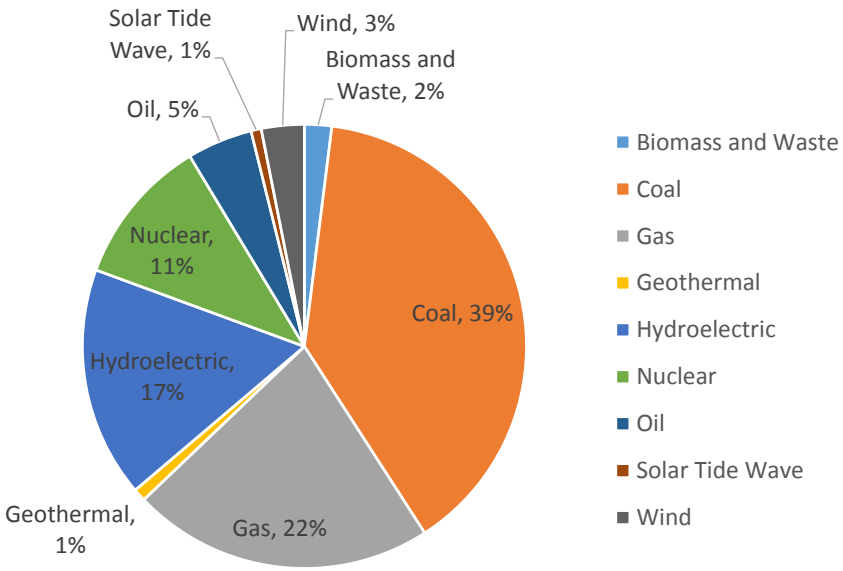

Figure 1.1: World electricity production by fuel (mtoe), end of 2014. Data taken from www.tsp-data-portal.org

Major improvements in cycle efficiency can be achieved also though careful design of the LP turbine and specifically the last rotor gives the largest contribution since in a typical modern plant about 15% of the turbine work is extracted at the last stage. Even though some of the kinetic energy at the outlet of the LP turbine is recovered as pressure in the exhaust hood, most of it is dissipated and constitutes a loss in overall efficiency. Increasing the annulus area of the last stage helps extracting as much energy from the fluid as possible. As a consequence modern last stage rotors are becoming increasingly large, in an effort to reduce leaving axial velocity. Switching from a 40in to a 50in last rotor blade,

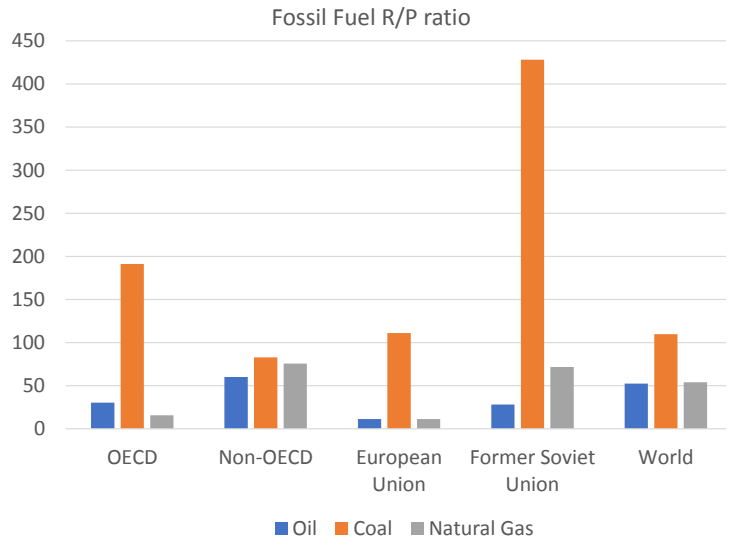

Figure 1.2: Fossil fuel Reserves to Production ratios, end of 2014. Data taken from www.tsp-data-portal.org

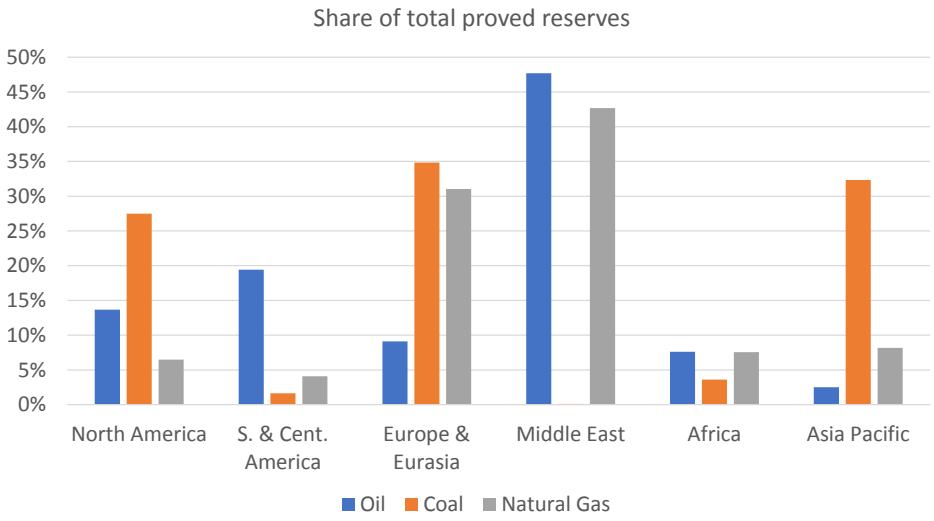

Figure 1.3: Share of fossil fuel reserves across different regions, end of 2014. Data taken from www.tsp-data-portal.org

together with an increase in reheat temperature can produce improvements in cycle efficiency up to 2.5%. Increasing the size of the rotor introduces numerous design challenges, such as supersonic inlet and outlet flow at high span sections, rapid expansion rates, wet flow, and high levels of blade load, which will be described in more details in the following sections.
All of the above considerations demonstrate that the design of state-of-the-art long rotor blades for steam turbines is a topic worthy of great attention, due to the potential reduction in fuel consumption and improvement in plant durability achievable by a robust design of this critical component.
There are numerous design approaches and problem specific strategies in last stage blade (LSB) design. This project places itself in the endeavour of providing a systematic and effective methodology for the design of these highly three-dimensional, highly loaded transonic LSBs operating in wet steam conditions. This involves the incorporation of strategies for the analysis and resolution of specific LP turbine scenarios into a rapid CFD based inverse design system, and eventual design and optimization of an actual steam power plant LSB. It is therefore essential to place the topic of specific LSB design into context, by understanding what are the major challenges faced by the aerodynamic designer, the nature of recurring problems and also why and how these relate to the sound operation of the LP turbine and of the entire power plant.
In the next section, the possible variations in thermal cycle are presented, in order to elucidate that having wet steam at the last stage is essentially an unavoidable feature of the cycle and how it affect the design requirements of the large rotors.

1.2 Steam power cycle requirements

The need for high efficiency in the vapour power cycle affects the design of the last stage low pressure turbine, by placing strict constraints on steam quality at turbine outlet. These requirements alone determine most aspects of the aerodynamic design scenario and it is therefore essential to understand why they are integral part of the whole plant operation.
This paragraph will introduce the major challenges faced by the designer when trying to provide a reliable high efficiency turbine while satisfying the require-

ments imposed by good thermal cycle efficiency. The vapour power cycle is assumed for now to be well represented by the simple ideal Rankine cycle. For any generic power cycle, the general approach is to improve thermal efficiency by increasing the temperature at which heat is transferred to the working fluid, and reducing the temperature at which heat is rejected.

If it is attempted to improve efficiency by, for example, reducing the condenser temperature in the Rankine cycle while keeping the same turbine inlet conditions (1.4a), an obvious increase in moisture content of the steam at turbine outlet is experienced. This is undesirable as low quality steam causes, at best, erosion of the turbine blades (more details on wetness losses are provided later).

The water saturation temperature at condenser pressure puts limitations on how low the heat rejection temperature can be. In order to maintain the low condenser temperature (and the improved efficiency coming from it) it is common practice to superheat the steam to a higher temperature, as shown in figure 1.4b. This improves quality of steam at state 4, and has the added benefit of higher average boiler temperature (hence efficiency improves). This increase in superheated steam temperature is however limited to the highest temperature recommended for the safe operation of turbine inlet materials. Note that for supercritical cycles (High boiler pressures and temperatures, values depending on definition) the steam condition in the LP turbine is approximately the same as for simple superheated; Only at the high (HP) and intermediate pressure (IP) turbines special design considerations must be taken into account in order to handle the high pressure and temperatures (material science also plays a major role in this area). Therefore, in order to increase the average boiler temperature further without raising the superheated peak temperature, the operating pressure of the boiler is usually increased. As shown in figure 1.4c, however, this has the drawback of low steam quality at turbine outlet.

The general solution to this comes from reheating the steam between a high and a low pressure turbine. This not only reduces the moisture content at LP turbine outlet, but also increases the average temperature at which heat is transferred to the working fluid, hence improving efficiency (figure 1.4d). The number of reheat cycles is limited to one or two by cost and complexity.

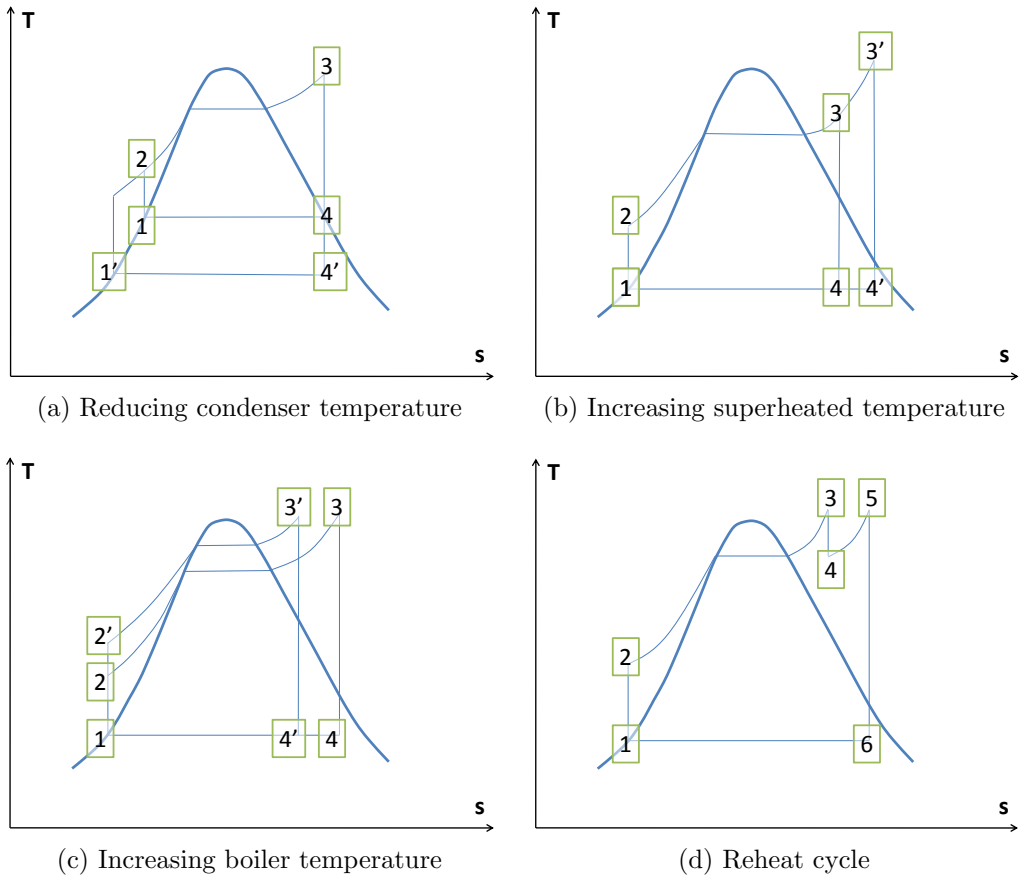

(a) Reducing condenser temperature

(b) Increasing superheated temperature

(c) Increasing boiler temperature

(d) Reheat cycle

Figure 1.4: Rankine Cycles

One more problem encountered in these improved efficiency cycles is the large volume flow rates through the LP turbine achieved when pressure drops to such low values of condenser pressure (usually below atmospheric). This brings difficulties in the design of the last stages of the LP turbine: as the size increases, speeds and stresses become challenging to handle. Even when regeneration is included in the cycle, problems due to the large volume flow rates can be present. Regeneration involves bleeding off some of the superheated steam before it enters the turbine. This steam is used to heat up the water entering the boiler. The purpose is to increase the average temperature in the boiler hence the cycle efficiency. This has the added benefit of reducing the volume flow rate through the turbine. The number of regeneration stages is limited by cost and complexity.
As a summary, the typical condition of steam at turbine outlet, as needed by the power cycle, is:

- Below saturated steam line
- High volume flow rate
- Low pressure

Hence the last stage turbine is characterized by:

- High velocities due to high volume flow rates
- Large sizes due to high volume flow rates and the need for maximum energy extraction
- Condensation effects and wetness losses

The above conditions pose problems in the design of the last stage turbine blades because of the following:

- Large size and high speeds create the occurrence of transonic to supersonic regions, hence very complex 3D shapes
- High twist to control leaving energy
- Shocks and expansion fans due to high velocities

- Possible non-equilibrium condensation effects
- Erosion of the blades due to moisture
- High tip speeds
- Great pressure drop, hence highly loaded blades
- Low Reynolds number
- High stresses due to : high rpm, complex shape and large size

The above, together with the fact that the last stage turbine provides the greatest contribution to the power output of the plant, make the layout and optimization of the blade profiles a very demanding task, with the need to improve efficiency while ensuring structural integrity. The above observations could be derived by simply observing the power cycle requirements. These and more problems will be analysed further when presenting the section on aerodynamic design of LSB.

1.3 Plant operation requirements

Before going into details of specific aerodynamic and profile design, it is important to bear in mind some more general design requirements for LSB, other than the improvements in thermodynamic efficiency and aerodynamic performance.
Generally speaking, LSB are required to operate over a long life span, ensuring high levels of reliability. It is essential to make sure that tolerances and the carefully designed geometry preserve over time in order to maintain efficient operation. Furthermore, structural failure of any of the rotating components could be potentially very hazardous and costly. Inspection and maintenance should be kept to a minimum to ensure continuous and effective operation of the power plant.
Not only LSB have to be high efficiency components, but also they have to be manufactured and assembled with reasonably easy procedures. It is also important to design the turbine for flexibility of usage, and adapt to seasonal climate

changes (affecting especially LSB, but also the entire cycle due to changes in condenser temperature and pressure), different types of fuels and boiler technologies. These affects also the aerodynamics, demanding ability to deliver performance at a range of Mach number values. Recent numerical investigations on the effects of condenser on the last stage have been carried out by Stanciou et al. [2013] who concluded that the heat sink can have large effects on performance by causing undesirable flow regimes, and then provided design guidelines for the exhaust hood which account for these effects. Finally, also the rotational speed may vary according to different levels of operation of the electric power generator, with obvious implications on the turbine design.

1.4 Aerodynamic requirements

1.4.1 General considerations

Once the general requirements for the LP turbine in relation to the power plant operation are clear, the focus shifts onto the more specific problems encountered in the LSB design process. Under an aerodynamics viewpoint a considerable effort must go into the analysis of shock and expansion fan structure and its interaction with boundary layers and wakes. The effects of the boundary layer thickness, along with dependency of flow characteristics on Mach number and Reynolds number are also of interest. Additionally, the estimate of profile and secondary losses is an integral part of the design, which is usually based on correlations derived from experimental data. More specific to LP turbine is the relatively recent research into wetness prediction methods, and novel methodologies for modelling non-equilibrium condensation effects .

All the above considerations will contribute to the shaping of the blade profile, together with generic considerations on incidence angles, interaction between stages, outlet diffuser flow, trailing shocks and wakes. The current research project will focus mainly on the aerodynamic design of the turbine blades, hence further and more detailed considerations on aerodynamic design will be provided in the next section. This section briefly summarises other and more generic design considerations and how they interlink with the aerodynamics of the blade profiles. First

of all, the aerodynamic design is strictly constrained by structural considerations, which should always be kept in mind and included into optimization strategies. As mentioned earlier, LSBs involve a high level of blade twist, due to the great variation in circumferential speed across the span, together with the need of extracting as much energy as possible at all span locations, especially at the low-turning sections near the tip. Typically, control over the leaving flow energy is achieved through twist, but also lean and sweep for low rpm or nozzle blades. However it is essential to reduce sweep and lean or eliminate these features completely in the LSB and also to make sure that twist is achieved through stacking about the centre of gravity of the profiles. This is to ensure reduced stresses due to the high centrifugal forces arising at the LSB: lean and sweep typically create a misalignment in the radial direction with consequent bending stresses arising at portions away from the profiles neutral axis, which are usually the greatest source of stress in LSBs.

Also it is important to ensure radial smoothness of the blade geometry when stacking the profiles: this can be a challenging task especially in the transition surfaces between positively cambered profile sections to convergent-divergent decambered profiles: combining geometrical parametrisation of these sections with the aerodynamic performance and the structural behaviour is not easily achievable, and a degree of graphic manipulation is still the case in modern designs.

Structural and manufacturing requirements impose constraints also on specific geometrical features of the blade such as wedge angles and trailing edge (TE) thickness, which have to be taken into account especially when manipulating these features for trailing shock control. Stein et al. [2010] provide insightful considerations on TE design or Ashgar et al. [2014] show how the LE geometry can affect the overall performance of an LP turbine. Also, prediction of wetness formation and droplet flow is essential in determining the countermeasures at the structural and material level: Erosion of the blades must be taken into account and this can affect the aerodynamic design (e.g. sometimes extra material is added at the LE, so that the optimal shape will actually be achieved after erosion has occurred, improving the lifespan of the blade) but also the metal treatment required such as surface hardening, and more comprehensive redesign of the blades, such as the introduction of hollow blades in order to prevent mois-

ture build up on the blade surface through suction. The overall thickness of the sections and resulting blade weight distribution is also a major constraint when profiling the blades, and must be taken into account in order to keep stress levels within allowable limits.
Stiffness requirements can also alter the aerodynamic performance, especially through the introduction of a snubber and closed shrouds. Modal analysis should be performed on the rotor, and major resonant frequencies should be avoided by improving stiffness and carefully selecting the range of operation of the rotor, together with wake frequencies from stages upstream. Finally the material selection opens another very broad design topic which affects the design by allowing different temperature ranges and blade durability through creep and oxidation control.

1.4.2 Shocks and other loss mechanisms

Due to the high circumferential speed and high steam expansion rates typical of last stage blades, the flow at rotor outlet is everywhere supersonic and very often near the tip also the inlet flow might be supersonic. Shock behaviour, interaction between shocks and expansion fans, and other loss mechanisms such as boundary layer separation must be controlled at every span section. Near the hub delicate profile losses mechanisms arise due the high flow turning conditions, and near the tip due to the high flow speed. Blade profiles and stacking are carefully devised in order to reduce the peak Mach number and control shocks occurring at LE (for example bow-shocks for supersonic tip inflows), as well as at the TE and across the blade passage (e.g. at the throat). Reducing the strength of LE and passage shocks is generally intended at avoiding shock induced boundary layer separation while controlling TE shock strength aims at minimizing wake mixing losses. The latter involves as a common practice reducing the unguided positive flow turning downstream of the throat. For low rotor exit Mach number, a simple way to achieve this is by straightening the suction surface portion of the airfoil downstream of the throat. These profiles are commonly known as *flat-back* or *straight-back*. Ainley and Mathieson [1955] investigated the influence of the suction surface curvature on turbine cascade performance and concluded

that flat-back designs were less prone to shock induced separation downstream of the throat. Furthermore, Moore and Sieverding [1987] showed that curvature on the rear of the suction surface leads to exit flow field non-uniformity due to high flow acceleration. As a consequence higher mixing losses are experienced. Flat-back turbine airfoils have been adopted for decades, and have evolved with time. Modern designs display increased TE thickness and downstream shift of the geometric throat in order to counteract the possible separation due to the sudden change in second derivative when the curved suction surface becomes flat (Simurda et al. [2012]).
If the exit Mach number is low, a convergent-divergent (CD) flow passage can be achieved with a flat-back design by carefully devising a combination of inter-blade pitch and stagger.

However, flat back designs are usually not flexible enough in giving the required level of control over flow turning and do not put enough emphasis on the CD condition (especially at high exit Mach number). This is particularly the case at high span locations, where a certain level of blade negative camber is introduced in order to achieve a good CD passage even at high stagger angles and low flow turning. The introduction of CD sections accelerates the flow upstream of the throat and aims at controlling the expansion and avoid local and unwanted peaks in Mach number, hence reducing the strength of the downstream shocks. Fundamental principles of 1D isentropic shock free CD nozzle flow can be used to determine within reasonable accuracy the appropriate exit/throat area ratio. Note that the exit area can be measured at TE of adjacent pressure side blade, or further downstream depending on the circumstances, considering the wake as the upper boundary of the divergent section.
Particularly at tip sections, the design against shocks becomes a delicate matter as the transonic nature of the flow causes most of the losses. At these sections several loss generating structures are present, such as suction side expansion fans at the LE, throat pressure side shock and possible reflection on adjacent suction side, plus two TE shocks (pressure and suction side). For supersonic inlet and high blade load, bow shocks upstream of LE are not uncommon at the tip, and a special treatment is required to predict these carefully (Senoo et al. [2011]), or experimental investigations (Parvizinia et al. [2004]). State of the art design

of tip sections involves careful geometrical manipulation in a restricted design space, with particular attention to LE shape and outlet metal angle, and it is based on the evaluation of a set of loss mechanisms (Senoo and Ono [2013]). Tip sections and high reaction turbine airfoils are very sensitive to small changes in all flow features. For example, boundary layer growth will move the actual throat upstream causing an early flow expansion with increased exit Mach number and TE shock. Shocks downstream of the throat can control the wake direction angle; this in turn will affect the expansion rates of the unguided flow and relative Mach number values.
Wedge angles are chosen in order to control shock strength, together with a reduction of TE thickness within manufacturing constraints. Additionally, shock behaviour at the LE (especially for high reaction sections such as tip sections of long last stage rotors) can be controlled by careful design of the upstream stator (for example controlling blade lean), like suggested by Ono et al. [2013].

Estimating profile losses and all secondary losses is also a relevant part of the design due to the highly loaded and low Reynolds number conditions. Profile losses trends are often linked to shock behaviour, together with the shock-boundary layer interaction. In subsonic flow, high profile losses are observed in high lift aft-loaded turbine blades, as observed by Prakash et al. [2008], due to flow separation on the suction side. For transonic flows aft-loaded designs display lower losses with respect to front loaded, but performance deteriorates with high exit Mach number (Corriveau and Sjolander [2004]). Secondary losses are associated with endwall vortices, tip leakage and mixing flows. Endwall losses are more relevant to low-aspect ratio blades, and it was observed that in aft-loaded configurations profile losses predominate over secondary (Popovic et al. [2006], Zoric et al. [2007]). It can be concluded that for the long LP turbine rotor considered in this project, profile losses are of main concern. Several correlations exist to model profile losses or estimate entropy generation and an extensive review is provided by (Denton [1993]). Despite the advent of high-fidelity CFD or in fact with the aid of it, the estimate and modelling of new loss correlations is still at present a topic of interest, with authors investigating effects of Mach number on loss generation in LP turbines (Vazquez and Torre [2012]), running experiments targeted at the measurement of aerodynamic losses (Abraham et al. [2012]), incorporating

numerical prediction of unsteady secondary flows in the design process (Schrack et al. [2013]) or correlating tip geometry to endwall losses (Volino [2014]). The use of empirical correlations is employed in optimization strategies where direct analysis of flow patterns and shock locations is not feasible in automatic way.

1.4.3 Wetness effects

Due to the thermodynamic necessity of expanding the steam below saturation, wetness losses become one of the major concerns related to condensation, together with blade erosion. The condensed droplets are heavier than the surrounding flow. This causes kinematic losses due to friction between vapour and water, as a first consideration. Furthermore, the trajectory of the droplets is usually different from the main flow, generally speaking with higher radial velocity. As a result braking losses arise due to the impact of the droplets with the blade, but also erosion of the blade. The situation is worsened by the build up of water on the pressure side of the blade, forming a film which eventually sheds larger droplets at TE. Erosion occurs at LE and shroud, leading to poor mechanical and aerodynamic performance (e.g. loss of shroud material with consequent dynamic instability and leakage losses, or erosion of LE with reduction in chord and serious shock strength increase).

The modelling of wetness formation for the above situation requires the implementation of steam tables for 2-phase flow computation (Hill et al. [2000]) or non equilibrium models (White [2003]). However condensation takes place across the whole turbine flow path and usually wetness losses have to be evaluated for the entire LP turbine, rather than for the individual stages.

In addition, the efficiency of the turbine is greatly affected by non equilibrium effects and consequent thermodynamic wetness losses.

Subcooling occurs because stable nucleation of water phase does not appear immediately at saturation, due to the required increase in Gibbs free energy to overcome initial droplet surface tension. After the critical radius for stable nuclei is achieved, droplet growth can proceed decreasing the free energy. Subcooling does not occur only at heterogeneous nucleation sites in the turbine, but at any location in the stage where expansion rates are too fast for equilibrium conden-

sation to take place (homogeneous condensation). The process by which the subcooled steam reaches equilibrium state is irreversible heat transfer at a finite temperature gradient, with associated entropy production. Additionally, the retention and release of latent heat between stages can affect aerodynamics by altering velocity triangles and thus incidence angles. A heat sink can yield higher work output in some cases, and a heat source might increase outlet velocities, altering velocity triangles and increasing entropy.

Non equilibrium modelling involves incorporating a nucleation model and a droplet growth model as opposed to wetness evaluation directly from pressure and enthalpy in the equilibrium assumption case. Some authors (Starzmann et al. [2010]) are trying to set up a methodology for direct evaluation of losses due to non-equilibrium condensation, without having to compare the results with equilibrium models (which would involve solving twice for the flow). This direct evaluation through possible correlations is essential for being able to employ these models at the design stage, instead of being limited to pure analysis.

Chapter 2

Literature review and project objectives

Having introduced the numerous challenges and requirements of LSB design, a short introduction is needed here to present how the current project will contribute to the design methods for the long blades of last stage turbines. First, a brief review from recent literature is provided in order to outline the available design methods, including the latest applications of inverse design. Then a more historical review of inverse methods is provided, in order to contextualise the methodology adopted in this study. In this light, the aims of the project will be laid out together with the novelty aspects of it.

2.1 Review of design methods for LP turbine

State of the art design of LP turbine blades is a two step process. First the blade profiles are designed in two-dimensions at a variety of span-wise locations. These are then carefully stacked to form the three-dimensional blade. While historically the 2D design has focused on aerodynamics, with structural considerations emphasized during the stacking process, designers recently also recognize the need of incorporating the stacking technique into a wholesome 3D aerodynamic design process. A detailed insight on stacking techniques such as tangential lean, meridional sweep and blade twist is provided by Havakechian and Denton [2015]. In

their paper they present advanced stacking methods applied to a last stage stator blade, and how these can be used to control flow aerodynamics of the stage, by directly affecting the spanwise load distribution at rotor inlet, to match the near impulse load requirements at the hub and high reaction load at the tip of modern last stage turbines. Due to the large aspect ratio of these long blades, the stage loading coefficient (inversely proportional to the square of blade speed) is necessarily very high near the hub. Since the enthalpy drop cannot vary greatly along the span, in order to reduce the magnitude of the exit swirl while conforming to the high loading coefficient at the hub, the stage reaction must be kept as low as possible. This reduction in exit swirl is aimed at minimizing the stage leaving energy and improving the performance of the diffuser. For similar reasons, at the tip sections of the long blades, high speeds result in low stage loading, which requires very high reaction when constraining the exit swirl angles. Thus, when designing a stacking strategy for the stator, stage reaction along the span can provide a useful target against which the strategy can be assessed.

Last stage rotors are required to deliver lower exit speeds and extract as much work as possible to minimise energy losses. As mentioned earlier, the resulting blades are very large in size and subject to high load and centrifugal forces, which means that stacking strategies that target aerodynamic performance such as sweep and lean are to be avoided due to structural considerations. Precisely for this reason, the stacking techniques proposed by Havakechian and Denton [2015] are applied to the stator blade, which is shorter and most importantly not subject to centrifugal load.
In view of the above considerations, 2D profile creation followed by structural stacking is still at present the dominant approach in LP turbine and especially last stage blade design. This means that the emphasis is on the creation of optimal 2D profiles, and the concern during stacking is the mechanical response under loading and centrifugal forces. To reinforce this idea it is good to look at recent work on 3D turbine blade design such as the one proposed by Amtsfeld et al. [2014]. In their paper they point out that such a quasi-3D approach misses the potential of finding optimal blade design especially in the presence of strong 3D flow effects. As an alternative they suggest a 3D method coupling parametrization

and CFD analysis into an optimization strategy. It is no coincidence, however, that this method was applied to thick, low aspect-ratio, high-pressure gas turbine blades. These geometries are significantly simpler than the long rotors at the last stage of a steam turbine, and yet the representation of the design space required 80 parameters, and the whole optimization process revealed to be computationally intensive despite carefully devised acceleration strategies being in place to cut down the turnaround time. The complexity of such an approach would increase dramatically if applied to last stage steam turbine rotors, due to increased size, blade twist and structural constraints. Furthermore it would not justify the effort, given that strong radial flow features are generally absent in these turbomachines. Stress related performance, however, is not the only concern when creating the 3D blade from the 2D profiles. A high level of blade twist will result as a consequence of broad variation in stagger angle from hub to tip. This blade twist, together with the remarkable variation in blade profile shape from thick highly curved hub sections to thin decambered tip, poses an additional challenge in creating a 3D blade from 2D profiles while also guaranteeing a certain smoothness of the 3D surface, as will be explained later in this section.

The design methods for 2D profiles of turbine blades have evolved greatly over time. In the past, families of standard profiles were available (i.e. NACA), so that the airfoils could be described with a few parameters and the aerodynamic performance of different shapes could be easily compared. With time, the more advanced understanding of flow physics led to the creation of new shapes which took into account elements such as boundary layer separation, turbulence, skin friction, shape factors and unsteady effects. Thus, new methods had to be developed in order to parametrise the airfoils efficiently.
A geometry model for axial flow turbomachines which historically has been widely accepted in industry is the one suggested by Pritchard [1985]. In his work he recognised 25 airfoil parameters associated which any blade shape. Only 11 of these are independent parameters, and the pressure and suction surfaces are represented entirely by analytical functions. This means that to uniquely define any airfoil it is necessary and sufficient to specify the number of blades, the radial coordinate of the 2D profile, the axial and tangential chord, the unguided

turning, the leading and trailing edge radii, the inlet and outlet blade angles and the inlet wedge angle. Furthermore, 6 of these parameters can be defined with default values. This method is very useful when creating a blade profile from scratch, and gives direct control over airfoil features such as inlet and outlet blade angles and inlet wedge angle which provide the traditional aerodynamicist with a straighforward way of generating a predictable and consistently feasible airfoil shape (as opposed to parametric representations with excessive degrees of freedom which might produce impracticable shapes under a structural or manufacturing viewpoint). This approach however provides only a limited design space, and the exploration of novel geometries is rather limited, especially when considering modern and more advanced airfoil geometries within a multi-disciplinary optimization context.

Futhermore, considerable proficiency of the designer is required in order to associate any particular change in one of the blade parameters with the resulting effect on flow physics.

In order to provide a more flexible representation of blade profiles, different parameterization techniques have been developed over the years, which are more geometrical in nature, which means that rather than fixing specific blade features, more generic geometrical features such as meanline or surface control points are defined and then the blade constructed with a set of predetermined rules. For example, Korakianitis [1993] proposed a 2D airfoil design method that defines a prescribed curvature through a spline, then links LE and TE geometries by imposing continuity of slope. Burman [2003] defined the blade profiles by constructing pressure and suction sides from a camber line spline and a thickness distribution. Corral and Pastor [2004] developed 2D airfoils from highly differentiable Bezier curves linked together with continuous slope.

All these methods are bound by the limitations imposed by the selection of constraints necessary in order to keep the blades manufacturable and ensure a certain degree of surface smoothness of the 3D blade. The importance of surface smoothness in relation to the parametric representation of the blade geometry has been emphasised in recent times by authors like Nemnem et al. [2014] who followed the work of Siddappaji et al. [2012] in developing a combined parametric-graphical method by which 2D profiles are first generated individually and then stacked

along a line or curve, and lofted with a graphical approach in order to obtain a smooth 3D surface. Each 2D profile is created by imposing some geometric constraints or a standard thickness distribution onto a blade mean-line defined by aerodynamic considerations. This is essentially a computer aided design (CAD) strategy in which streamline definition provides an insight towards the final shape, but it still remains only a geometric representation and consistent manipulation of the parameters is required from more specific aerodynamic requirements. Nevertheless, the fact that authors decide to focus on blade smoothness demonstrate its importance in turbomachinery design. This is because the geometric curvature has a major effect on aerodynamic performance. This concept is well explained by Fox et al. [2009]: deriving Bernoulli's equation in the stream-wise direction it can be shown that the pressure gradient along a streamline is inversely proportional to the radius of curvature of the streamline. Other advantages of smoothness could be either stress or erosion related, or linked to manufacturing considerations.

All of the above methods provide a solution for the creation of blade profiles, but not a precise guidance on how to achieve the desired aerodynamic performance, such as control over shock structure, boundary layer, profile and secondary losses, or thermodynamic losses incurred for example in two phase flows. A system is required in order to investigate the effect of manipulating the geometrical parameters on the flow physics, and modify the blade profile accordingly. Traditionally the required performance of the turbine blades was attained by direct geometric manipulation, selection of blade angles, wedge angles, suction surface curvature and blade thickness which were decided on the basis of empirical correlations or direct experimentation. A classic book on turbine design is the one by Horlock [1966], while a comprehensive summary on estimating losses through correlations and flow physics considerations is given by Denton et al. [1987], Denton [1993]. Traditional methods are generally speaking time consuming and heavily reliant on the experience and proficiency of the designer. These methods have greatly evolved in time, not only thanks to adoption of blade generation techniques listed above, but also in association with the advances in computational methods. Implementation of computational fluid dynamics (CFD) at the design level is very popular at present, with a variety of associated design techniques which deviate

from a classical know-how based approach. However, these also require a great effort in setting up the problem, and often also long computational times and cost will be involved. An additional benefit of modern CFD techniques is the potential incorporation of a broad range of specific analysis tools such as estimate of entropy generation through a stage or steam condensation and two-phase flows.
When a method for geometric blade representation is employed in association with a performance evaluation technique, this is generally speaking known as a *direct design method*, whether it be an old-school manipulation of blade metal angles followed by a correlation based flow evaluation or a modern CAD based parametrization coupled with an advanced CFD technique.
Designing state of the art turbine blades with the conventional direct methods, even with modern parametrised profiles and CFD analysis is extremely challenging, since the relationship between geometry and flow features is defined through the solution of flow equations and hence it is highly non-linear. This has made automatic optimization techniques very popular amongst aerodynamic designers, thanks to the availability of CFD tools, together with development of Finite Element Methods (FEM) for stress analysis. Optimization techniques such as Genetic Algorithm (GA), Non-dominated Sorting GA (NSGA), Neural Networks (NN), Simulated Annealing (SA) are used to search for global maxima or minima in discontinuous and non-linear design spaces, in which relations between design parameters are difficult to describe through explicit functions. When using automatic optimization the attention shifts to the selection of the objective function, constraints and parameterzation. The effective representation and parametrization of the blade geometry has become a crucial point in the design process, and much effort is being placed in attempting to represent the broadest design space with the smallest number of parameters. This can be done through direct approximation techniques such as Non-Uniform Rational B-Spline (NURBS) representation (Chen and Yuan [2008], Hasenjager et al. [2005]), or stacking of 2D profiles with reduced degrees of freedom (Sonoda et al. [2006], Oyama et al. [2002], Dennis et al. [2000]), by defining parameters such as camber, stacking line and blade angles (Oksuz and Akmandor [2010]). These direct methods of parametrization can become cumbersome, as they require numerous parameters to be defined alongside a strict set of constraints in order to keep the blade shape

within reasonable manufacturing limits. As it will be explained in the next sections, the alternative to this is offered by the parametrization of the blade through few loading coefficients used in inverse design, which allows the exploration of very broad design spaces while reducing considerably the number of parameters required and therefore making it a more efficent choice for optimization (Wang and Zangeneh [2014] Boselli and Zangeneh [2011], Zangeneh et al. [2008]).
Examples of applications of global optimization techniques to the design of LP steam turbines are available in Kosowski and Tucki [2010] and Yuan et al. [2010]. The most notable example is the paper by Senoo et al. [2010], in which the NSGA based design of a last stage long rotor of a steam turbine is presented. Here each 2D blade profile (airfoil) is represented through a 4th degree spline. A non-dominated sorting genetic algorithm (NSGA-II) uses as inputs the control points of each airfoil spline, and returns optimised blade geometries based on the performance predicted through a CFD solver. A set of constraints is placed on control points mobility, leading and trailing edge shapes, wedge angles and axial chord. Shock waves downstream of the throat are controlled during the design by the method of characteristic curves. The 2D profiles are stacked along the centroid and then a NURBS surface is fitted to give the 3D blade. The resulting blade is currently state of the art in last stage turbine design, with extended efforts placed in the design of the tip section (Senoo and Ono [2013]).
As mentioned above, optimization techniques such as GA allow the exploration of broad design spaces, to find global optima and handle multi-objective problems. However, they can also be computationally expensive. Another approach to shape optimization is provided by adjoint methods. These originally derive from the sensitivity analysis methods of control systems. Often in turbomachinery design only minor modifications of a baseline design will yield an optimal blade profile. In these cases a deterministic, gradient-based optimization technique is considered acceptable.
The adjoint method allows the calculation of an objective function gradient, with a computational cost independent of the number of design variables, and has been employed in turbo-machinery design in recent years (Walther and Nadarajah [2012], Lu et al. [2013], Pini et al. [2014]). To the author's knowledge the adjoint method has not been applied to the design of last stage steam turbine

blades in the available literature.
Because of the complex set of constraints required to maintain such a long and highly twisted blade within a realistic and manufacturable shape, the design of individual 2D sections is still currently the most effective technique.
Other optimization strategies specific to LP and steam turbines include probabilistic methods based on Baeysian statistics such as in Miki et al. [2014] or a more general sensitivity analysis focused on the variations between a numerical analysis based design and a real-life application as presented by Bertini et al. [2012].
All of the design methods, with the exception of the adjoint method, can be classified as direct methods, thus rely on some kind of iteration between separate blade parametrization and aerodynamic or multi-disciplinary performance assessment, with a broad variety of results available in literature. As will be presented shortly, inverse design methods which start from the prescription of a design flow quantity provide a unified way of parametrising the blade geometry while providing a more direct control over the aerodynamics of the turbomachine.

2.2 Review of inverse design methods

Before detailing all the advantages of inverse design over direct methods, an introduction to inverse design is provided here, highligting the most relevant techniques and how they evolved with time. Practically all the inverse design methods in use at present have reduced, technically speaking, to semi-inverse design. These take the form of a re-cambering of blade profiles, in which the thickness distribution is held fixed. In most cases only the camber line is modified, in order to satisfy a prescribed load distribution and other flow conditions. In the remainder of this report, however, all methods will be simply referred to as inverse design, with no differentiation from the earlier methods in which pressure and suction surfaces were modified independently.
The main advantage of inverse design methods over conventional ones is that they provide more direct and intuitive control over the aerodynamic behaviour of the airfoil. This is because through the blade loading specification many flow features can be influenced effectively by the designer, such as peak suction, dif-

fusion, shock position and total work output. Additionally inverse design offers an attractive way of parametrising the blade geometry through the desciption of a blade loading, which can be easily implemented into global optimization techniques. More specific advantages of inverse design and why this was chosen in the current project will be explained in the next section, after the review of different available methods provided in this section.
Over time, many different inverse design methods have been developed based on a variety of fundamental flow physics assumptions and mathematical techniques. Even though most of these methods have proven interesting under a theoretical and research viewpoint, very few have survived in real life to the demanding requirements of modern engineering applications.
Out of the most successful inverse design approaches, two main categories can be identified: the methods based on *potential flow* and the *time-marching* methods (based on either Euler or Navier-Stokes equations).

2.2.1 Potential flow methods

Typically, potential flow methods are very mathematical in nature and provide mostly analytical or sometimes iterative strategies to modify an airfoil shape according to a prescribed flow quantity, most commonly a velocity distribution. These methods were the earliest to appear in inverse design practice.
Notable methods in this group are: the *conformal mapping* method of Lighthill [1945], where the airfoil is mapped to a unit circle in the complex plane and a surface velocity distribution is prescribed; the *potential-stream function* method introduced by Stanitz [1953], where the the flow solution is resolved on the $\phi - \psi$ plane[1] and the flow angle is used to determine the required cascade passage geometry; the *hodograph* method introduced by Nieuwland [1967], in which the potential equations are solved on the velocity-streamline angle $(V - \theta)$ plane; and the *fictitious gas* method, employed by Sobieczky et al. [1978] and Nakamura [1981] to design shock free transonic airfoils by modifying the local density in order to keep the flow equations everywhere subsonic.

[1] where ϕ is the potential flow function and ψ is the stream function

The main disadvantage of these early methods is the limitation to thin airfoils or to strictly incompressible flow, hence the difficulty in coping with more complex geometries or flow discontinuities such as shocks. Also, they are limited in scope, as many of them are intended for the design in a particular flow regime, and very often a compromise has to be made in order to achieve a feasible airfoil geometry.
Additionally to the above methods, the *circulation methods* can also be classified as belonging to the category of potential flow methods. The circulation method was introduced by Hawthorne et al. [1984], where blades were represented by sheets of vorticity and modified according to a prescribed distribution of circumferentially averaged swirl $r\tilde{V}_\theta$ (r is radius V_θ is the angular velocity, and the tilde designates a circumferentially mass averaged value). This method has been successfully expanded and applied to 3D design of radial turbomachinery by Borges [1986], Hawthorne and Tan [1987], Zangeneh [1988], and expanded to account for compressible flows by Zangeneh [1991]. The main advantage of this method is the rapidity with which novel 3D geometries can be created, an advantage derived from not having to numerically solve the Euler or Navier-Stokes equations.
Unlike the other potential methods, the circulation methods have survived the test of time and have been applied to a variety of applications. The most successful cases include water pumps (Zangeneh et al. [2008]), radial compressors and diffusers (Zangeneh et al. [2011]), and can tackle specific problems such as stress in axial turbines (Boselli and Zangeneh [2011]) or noise reduction in turbochargers (Wang and Zangeneh [2014]), via inclusion of dedicated models into an optimization process.

2.2.2 Time-marching methods

Another main category of inverse design can be established by grouping together all the time-marching methods. These are by definition of a numerical, more than analytical, nature. Generally speaking a time-marching flow solver (based on the discretised Euler or Navier-Stokes equations) is coupled with a blade update algorithm which iteratively modifies the blade geometry, usually driven by the difference between a prescribed and a computed flow quantity.
The advantage of these methods over potential flow ones is the increased level of

accuracy, especially for cases in which compressibility effects play a major role. The most notable advantage is the inherent shock capturing attributes of the numerical solution of the integral form of the flow governing equations.
As for the potential methods, also in the case of time-marching methods a great variety of techniques for modifying the blade shape have been developed over the years. Two main sub-categories can be classified according to the prescribed flow quantity: This can be chosen to be the **pressure loading** ΔP (the difference in static pressure between pressure and suction sides of the blade); or the **circumferentially mass averaged swirl** $r\tilde{V}_\theta$.

2.2.2.1 ΔP method

The ΔP methods have evolved historically from conceptually similar iterative blade update techniques, which were originally based on the prescription of other flow quantities such as the surface velocity, surface Mach number or static pressure, specified separately on pressure and suction sides of the blade.
The ΔP methods can be further classified according to the wall boundary condition employed in the flow solver: *transpirating* walls or *moving* walls.
In the transpirating wall methods, the solid blade walls are treated as permeable, imposing - instead of a zero flux condition - a prescribed flow quantity (such as static pressure) . This type of boundary condition in the flow solver results in transpirating flow across the blade walls, until a final target geometry is achieved iteratively and the fluxes normal to the walls tend to zero. Examples of this method are given by Leonard and Van den Braembussche [1992] who prescribed the surface Mach number, and a 3D extension of their work is provided by Demeulenaere and Van den Braembussche [1998], with the prescription of surface static pressure. The restriction with the prescription of surface static pressure (or Mach number) is that unless a realistic distribution is known a priori, the independent modification of pressure surface and suction surface might result in infeasible designs, such as overlapping or open trailing edges.
A solution to this is the imposition of a surface pressure difference ΔP (also known as pressure loading) rather than absolute values of pressure. This method

was demonstrated by Dang et al. [2000] and Medd [2002], Medd et al. [2003].
The transpirating wall method is highly integrated with the chosen flow solver, because of the necessity of imposing the permeable boundary condition during the numerical flow solution. This is a disadvantage because it lacks the modularity required to couple the blade update algorithm to any flow solver.
Furthermore, in the author's experience, the permeable wall boundary condition lacks robustness, due to the non-physical transpirating fluxes at the boundary and the special treatment and assumptions it requires in order to achieve convergence. Having flow crossing the blade surface effectively transforms the wall boundary condition into an inflow (or outflow). At a inlet boundary, two conditions must be specified for subsonic flow (which is always the case for transpirating fluxes, given that the required blade modifications are always small), but only one condition is provided by the imposition of a prescribred pressure. Authors like Leonard and Van den Braembussche [1992], Demeulenaere and Van den Braembussche [1998] , Dang et al. [2000] and Medd et al. [2003] all make a common assumption that the normal components of the transpirating fluxes are equal on pressure and suction sides of the blades, which essentially provides the extra condition. Their blade update algorithm is based on this unphysical assumption, acceptable only for thin blades, with relatively straight camber lines and no major three-dimensional geometrical features, such as the NASA 37 rotor employed in all their papers. ΔP methods have nevertheless evolved in recent times in order to improve modularity and adapt to viscous flows. Transpirating walls have been abandoned by their original authors because of the level of integration with a specific flow solver, and because of the incompatibility with the no-slip condition of viscous flow solutions (the old methods required velocity vectors at the walls). Van Rojii and Medd [2012] suggest a reformulated ΔP method compatible with the no-slip condition, in which the blade modifications are driven by the difference between a prescribed load and the load computed by a Reynolds-Averaged Navier-Stokes (RANS) solver. Their method can be classified as a "moving wall" method, since the residual difference in blade loadings is resolved as a virtual blade velocity component, used in the blade update algorithm.
Similarly, authors such as Page et al. [2013] and Arbabi and Ghaly [2013] have coupled blade update modules to commercial or proprietary RANS solvers. The

blades are modified by replacing a fixed wall boundary condition in the blade update procedure with a movement controlled by a virtual velocity distribution, arising from a difference between prescribed and computed ΔP.
Even though innovative, these methods seem to be very theoretical exercises. Van Rojii and Medd [2012] reiterate a redesign of NASA 37 rotor, with results very similar to what was achieved in the early 90's with the older transpirating wall methods. Arbabi and Ghaly [2013] also limit their study to a thin, straight blade, and imposing arbitrary ΔP distributions they achieve almost imperceptible modifications and an increase in computed total-to-total isentropic efficiency of 0.23% (not very meaningful by industry standards, as it could be easily due to effects of numerical modelling). Page et al. [2013] show a very interesting application to multi-stage design, but once again the applicability to complex geometries and flow regimes typical of last stage blades seems limited, as revealed by the simple geometries chosen in their case study.
Additionally, the recent ΔP methods (as well as the older ones) all have in common their use of local information such as surface pressure, to drive blade modifications. This is unavoidably very dependent on the accuracy of the numerical solution, and possibly limited in scope because of how information propagates in a discretised space.

2.2.2.2 Swirl velocity method

The second recognisable category of time-marching inverse methods is the swirl velocity $r\tilde{V}_\theta$ method. This is a re-adaptation of the circulation method presented earlier, but making use in this case of a Euler flow solution rather than having a potential flow field. This approach was presented by Dang and Isgro [1995] and a 3D adaptation of this is the one by Tiow and Zangeneh [2000].
In this method, the difference between prescribed and computed circumferentially mass averaged swirl rV_θ drives the blade modifications. The meridional derivative of the swirl rV_θ distribution is proportional to the blade loading, hence this method has the advantage of a direct control over the loading. Furthermore, specifying the inlet and outlet rV_θ values at every span location effectively fixes the Euler turbine work output (or compressor work input).

The main advantages of this method are the robustness derived from the use of mass averaged values (i.e. information comes from across the whole flow passage) and the excellent modularity: since no special boundary conditions are required, the blade update module can be easily coupled to a flow solver.

The implementation of the $r\tilde{V}_\theta$ method will be explained in more detail in the course of the report, as the fundamental principles behind it have been adopted in the creation of the novel blade update technique presented within this research. The reasons behind this choice are outlined in the following section.

2.3 Choice of inverse design and proposal of novel method

In this sections the main advantages of inverse design are highlighted in conjunction with the selection of the most suitable strategy amongst the numerous ones available in literature as listed in the previous section. The objective of this project is to create an inverse design strategy specific to the requirements of last stage steam turbine blades. The main advantages of inverse design have been outlined at the start of section 2.2, but are briefly reiterated and reinforced here. With respect to conventional design methods, inverse design allows the rapid specification of a prescribed blade loading without a traditional iterative procedure of manually modifying a blade geometry and then measuring the resulting performance. As explained earlier, manipulating the blade loading gives the designer a more direct and intuitive control over the resulting flow features. Additionally, it allows the parametrisation of the blade geometry in terms of blade loading (a blade loading curve can be described through a few control points), which facilitates the exploration of broad design spaces and creation of novel profiles free of the constraints of a conventional direct geometric parametrization. As such, this methodology lends itself to a rapid implementation into multi-objective and multi-disciplinary optimization strategies.
Another advantage of recent semi-inverse design methods is that blade modifications occur through the re-cambering of an initially specified profile. This allows

the specification of a baseline thickness distribution, which can be devised with mechanical performance in mind, or the eventual achievement of a smooth 3D blade.

Finally, even though the inverse methods proposed in the present context are developed for 2D profile design (in accordance to common practice of 2D stacking strategies for last stage blades), inverse design can generally speaking be extended to 3D, and find use in the design of a variety of applications such as radial turbomachines, or axial components subject to large radial flows.

In order to create an inverse design method targeted at the long blades of a last stage steam turbine, two main aspects of these machines have to be kept in mind: the geometrical complexity and the occurrence of wet steam flow.

The problem of geometrical complexity relates to the high level of twist displayed by this kind of blade, going from thick, curved, near-impulse hub profiles to thin, decambered, high-stagger, high-reaction profiles near the tip. The latter sections pose particular problems in terms of a simplified geometric representation. Traditional inverse methods derive their blade update on the assumption of a possible representation of the blade in terms of a *tangential* thickness distribution (this is the difference between suction and pressure sides of a profile in the circumferentially tangential direction at a given axial position). This can lead to serious problems when dealing with the high-stagger angles seen on last stage rotors, especially when attempting to modify regions near the LE, as will be shown in the course of this report. A way of representing blade profiles in terms of their *normal* thickness will be proposed (this is the thickness perpendicular to a camber line which is in turn the locus of points bisecting the thickness segments at each location), and most notably a novel blade update formula will be derived from the assumption of this type of thickness description. The novelty of such a method is easily seen comparing to all other inverse design techniques available in literature. Even though a few authors such as Medd [2002] have achieved the imposition of a normal thickness distribution, the underlying principle of the blade update algorithm required temporary conversion to tangential thickness representation which, as it will be shown, is not compatible with the kind of turbine blades considered in the present research.

The second concern is about the effect of condensing steam on the design pro-

cedure. In inverse design, aerodynamics are controlled by prescribing a flow quantity. Clearly, being able to compute this flow quantity accurately is essential for the successful implementation of the method. Wetness effects have a great impact on blade loading, as they change the thermodynamics of the flow. The inclusion of wet steam properties in inverse design is another novel objective set out in this project as, to the author's knowledge, no inverse design methods based on a real gas model are available in literature.

The need to more accurately predict the steam flow field immediately narrows down the selection of the type of inverse design the few listed in the previous section. Clearly, none of the potential flow methods can be considered, and among the time-marching inverse methods, the preferred choice falls on those which can provide a modular structure, with blade update and flow evaluation easily discernible. This is because a stand-alone blade update module can be easily coupled with a flow solver, be it a real or ideal gas one, and allows to focus separately on the inclusion of steam properties in a flow solver while developing a new blade update method in parallel.
The choice is now between a Δp or rV_θ method. Even though in most recent years the time-marching inverse methods are based on a Δp prescription, these are, as explained earlier, very theoretical and not very suitable for the current objectives. Δp methods can lack robustness because of the use of local surface information only to drive blade updates, and can show problems when designing thick and curved blades because of the necessary assumption of equality of the normal "virtual velocity" components on pressure and suction sides of the blade (this assumption deviates from reality at high blade curvatures). Additionally Δp always require the possibility of describing the blades in terms of tangential thickness. This is a necessity of the Δp methods, because each value of Δp is computed at a given axial location as difference in static pressure between pressure and suction sides: this difference must be taken in the tangential direction in order to have physical significance and be directly related to torque. Given that it is not always practical to represent the last stage blades in terms of tangential thickness, Δp are not the first choice in this case.
The prescription of rV_θ has been extensively used for a number of years in the

successful redesign of industrial applications (through potential inverse methods), and has proven to be a robust and meaningful way of controlling the aerodynamic performance of turbomachinery. Therefore, it seemed natural to choose a time-marching method based on swirl velocity.
The work here presented begins with the modified adoption of a swirl velocity method similar to the one of Tiow and Zangeneh [2000]. The solver was recreated with the inclusion of real water and steam properties. Then, after investigating the limitations of a tangential thickness based method, a new way of representing blade profiles was devised, casting the foundations for a novel inverse design technique. The novelty lies principally in the creation of a new blade update algorithm from scratch, based on a normal thickness distribution. Finally a 3D rotor was redesigned, making use of the inverse method and with an overall strategy similar to none observed in literature so far.

2.4 Summary of content

As explained in the previous section, the work here presented begins with the re-creation of an older inverse method based on swirl velocity prescription and tangential thickness specification. This served a double purpose: to test the inclusion of real gas properties in the inverse design procedure, and to investigate the limitations of such a method when applied to the blade geometry under consideration (long blades from the last stage of an industrial turbine). The inverse method is composed by a blade update algorithm based on the one by Tiow and Zangeneh [2000], coupled to a 2D flow solver. The flow solver was initially chosen to be very simple such as the one presented by the original author of this method, with a sheared H-mesh which, as will be seen, greatly simplifies the blade modification process in a tangential thickness specification method. The choice of numerical scheme was an adaptation of the one by Jameson et al. [1981] which, for its ease of implementation and robustness, has been the choice of all the authors of time-marching inverse methods listed in the previous section, with the exception of the three authors who coupled their blade update modules to existing commercial or proprietary solvers. Given that the first objectives in the present case were to modify the solver with the inclusion of wet steam evaluation

and to investigate any shortcomings of the inverse design, developing the flow solver and blade update module was necessary in order to fully understand all aspects of the procedure.
In the second half of this work, once the shortcomings of a tangential thickness based inverse method had been highlighted, a new methodology was suggested. This is based on the representation of the blade profiles through their *normal* thickness distribution (normal means perpendicular to the camber). Since the sheared H-mesh was not compatible with this new methodology, a new type of grid had to be chosen, in order to connect smoothly across the flow passage the points on pressure and suction side of the blade. These had to be connected directly, but it could not be done with a straight line. An appropriate choice with these kind of boundaries was to use an elliptic solver. This was developed in-house for better integration with the overall procedure, and to satisfy the requirements of the sponsors who needed a complete procedure to be delivered at the end of the project, independent of third-party software. Furthermore, having a mesh generator helps remeshing during the inverse design procedure, each time after the blade profile is updated. Given that the modifications are small, the elliptic solver converges within few steps, and yields better quality meshes than other methods such as simple shearing or spring methods.
Chapter 3 presents the initial flow solver based on the sheared H-mesh. This was expanded with the inclusion of wet steam properties in chapter 4. Chapter 5 presents the initial inverse design procedure and an explanation of its limitations as applied to last stage steam turbine blades. The new method required a new way of representing blades, presented in chapter 6. Additionally, the elliptic mesh required the solver to be modified, in the way fluxes are evaluated. This is because the solver based on H-mesh did not need the evaluation of tangential fluxes on the computational cell sides at constant axial position. Chapter 7 covers this part and its validation. The new blade update algorithm is presented in chapter 8. Finally, the new methodology was employed in a new redesign strategy for the 3D rotor, as shown in chapter 9.

Chapter 3

Two-dimensional Euler solver: first version

3.1 Finite volume multi-step time-marching method

3.1.1 General considerations

The two-dimensional governing equations of fluid flow can be arranged in their integral from by considering a control volume Ω with boundary C:

$$\frac{\partial}{\partial t}\iint_{\Omega}\mathbf{U}d\Omega + \oint_{C}\mathbf{F}d\mathbf{r} = \iint_{\Omega}\mathbf{J}d\Omega \tag{3.1}$$

Where the closed line integral is performed along the boundary path $\mathbf{r}$. In the case of inviscid flow, the source term $\mathbf{J}$ disappears. With the above formulation, the variation of a quantity $\mathbf{U}$ within the control volume depends only on the values of the fluxes $\mathbf{F}$ on the control surface C (control curve in 2 dimensions). The governing equations can be thus discretized directly in the physical space by means of the finite volume method. This method was developed for the solution of two-dimensional flows by McDonald [1971] and MacCormack and Paullay [1972]. A successful development of this technique, which will be used in the present case, is adapted from the one devised by Jameson et al. [1981]. The fundamental idea behind this method is the coupling of finite volume discretization of the integral Euler equations with a multi-step Runge-Kutta time-marching al-

gorithm, and the incorporation of a blend of adaptive dissipative terms to ensure stability without excessively compromising shock capturing precision. This has proven to be an ideal technique for flows with discontinuities, due to the great suitability of the integral equations in conservation form, and for the rapidity of the implementation. Even though old, this scheme is considered a classic, and will pose a robust foundation for the investigation to be carried out, which will focus on the inverse design method rather than providing advances in numerical flow analysis, which is beyond the scope of the current work. Coupling of the blade update modules achieved in the course of this project with more advanced CFD solvers is a very interesting topic, which will be definitely worthy of notice in future work.

A mesh is created to divide the physical flow space into a set of cells. A finite control volume can be composed of one or more adjacent cells. From now on it will be assumed that each cell corresponds to a finite volume. At each finite volume, the discrete form of equation (3.1) is applied by evaluating the fluxes across the cell sides. The advantage of this method is that the flow region can be divided into any arbitrary mesh as long as the cells cover the whole region and do not overlap without having all surfaces (i.e. cell boundaries) in common with other cells.

In the *cell-centre* formulation, the values of the flow variables are stored at each cell centre; in the *cell-vertex* (also referred to as *node-centred*) formulation, the values are stored at the vertices of each cell (the nodes of the grid). This will affect how the fluxes are approximated at the cell sides.

In this first version of the flow solver, a cell-centre formulation is adopted, as suggested in the original paper by Jameson et al. [1981]. The fluxes at the cell sides can be then approximated by taking the average between two adjacent cells; this is done either directly:

$$\mathbf{F_k} = \frac{1}{2}(\mathbf{F}_{i-1} + \mathbf{F}_i) \tag{3.2}$$

or by using the fact that the flux vector is function of the solution vector, hence

averaging the solution vector values instead:

$$\mathbf{F_k} = \mathbf{F}\left(\frac{1}{2}(\mathbf{U}_{i-1} + \mathbf{U}_i)\right) \tag{3.3}$$

Formulation (3.2) is preferred in the present case because it requires fewer evaluations at each step; Holmes and Tong [1985] claim that this is less stable, but for the purpose of the current implementation no major differences were observed. From now on the k subscript indicating values at the cell sides will imply that the averaging (3.2) has been applied.

3.1.2 Discretization

The first relevant aspect of the method is the discretization of the Euler equations in their integral form. These are written in two dimensions for a region Ω bounded by C as:

$$\frac{\partial}{\partial t}\iint_{\Omega} \mathbf{w} d\Omega + \oint_{C} (\mathbf{f}dy - \mathbf{g}dx) = 0 \tag{3.4}$$

which is a special case of equation (3.1), with the all-round integrand expanded for the two components of the flux vector $\mathbf{F}$, the source term set to zero, and $\mathbf{w}$ representing the quantities in $\mathbf{U}$ (i.e. the solution vector for the case of the Euler equations). The solution vector and flux vectors are given by:

$$\mathbf{w} = \begin{pmatrix} \rho \\ \rho u \\ \rho v \\ \rho E \end{pmatrix} \qquad \mathbf{f} = \begin{pmatrix} \rho u \\ \rho u^2 + p \\ \rho uv \\ \rho uH \end{pmatrix} \qquad \mathbf{g} = \begin{pmatrix} \rho v \\ \rho uv \\ \rho v^2 + p \\ \rho vH \end{pmatrix} \tag{3.5}$$

where, for a perfect gas:

$$E = \frac{p}{(\gamma - 1)\rho} + \frac{1}{2}(u^2 + v^2) \tag{3.6}$$

$$H = E + \frac{p}{\rho} \tag{3.7}$$

The fundamental idea in the method is reducing equation (3.4) to an ordinary differential equation (ODE) for each finite volume in order to be able to apply Runge-Kutta multi-step algorithm and advance the solution in time. This ODE will take the form of (at each cell):

$$\frac{d}{dt}(\mathbf{w}h) + \mathbf{Q} = 0 \tag{3.8}$$

Here $\mathbf{Q}$ represents the numerical approximation to the line integral in equation (3.4). This is evaluated through the discrete form of the integral, as follows.

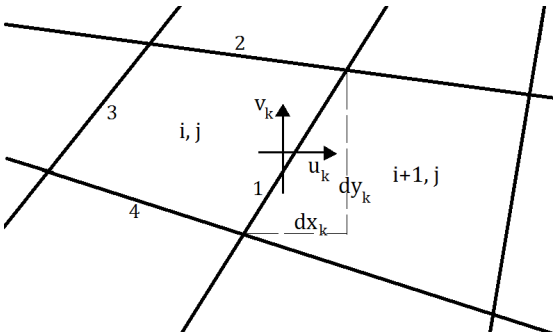

Figure 3.1: Definition of cell side values

Consider a cell i, j with area h (figure 3.1). Quantities are defined at cell centres (since the cell-centre formulation is chosen). The discrete from of the integral equation in (3.4) is given by:

$$\frac{\partial}{\partial t}\mathbf{w} \cdot h + \sum_{k=1}^{4}(\mathbf{f_k}\Delta y_k - \mathbf{g_k}\Delta x_k) = 0 \tag{3.9}$$

Once again, the subscript k indicates values at the cell sides. Expanding, for illustrative purposes, the x-momentum component of equation (3.27) (using the second row of (3.5)):

$$\frac{\partial}{\partial t}(\rho u) \cdot h + \sum_{k=1}^{4}\{[(\rho u^2)_k + p_k]\Delta y_k - (\rho uv)_k \Delta x_k\} = 0 \tag{3.10}$$

The mass, y-momentum and energy equations are discretised in the same way. Note that equation (3.10) is in fact in the ODE form of (3.8), where the $\mathbf{Q}$

component is given by the summation term.

3.1.3 Numerical dissipation

To prevent oscillations in the solution at discontinuities and ensure stable convergence, it is essential to introduce additional numerical dissipation through artificial viscosity terms. Therefore equation (3.8) is modified to equation (3.11) to be used in the Runge-Kutta algorithm. Here $\mathbf{D}$ represents the dissipative term:

$$\frac{d}{dt}(\mathbf{w}h) + \mathbf{Q} - \mathbf{D} = 0 \tag{3.11}$$

The dissipative term is computed using the blend of second and fourth differences scaled by adaptive coefficients "sensing" the pressure gradient and "switching on" the fourth order terms in regions of high pressure gradients. This means that no excess artificial viscosity is introduced where not needed, ensuring better accuracy of the solution. This formulation is given by Jameson et al. [1981], and it is of an empirical nature. For any term in $\mathbf{w}$, for example the density ρ, the dissipative term is given by:

$$D_\rho = d_{i+\frac{1}{2},j} - d_{i-\frac{1}{2},j} + d_{i,j+\frac{1}{2}} - d_{i,j-\frac{1}{2}} \tag{3.12}$$

Where all the d terms take a form similar to:

$$d_{i+\frac{1}{2},j} = \frac{h_{i+\frac{1}{2},j}}{\Delta t}\left[\varepsilon^{(2)}_{i+\frac{1}{2},j}(\rho_{i+1,j} - \rho_{i,j}) - \varepsilon^{(4)}_{i+\frac{1}{2},j}(\rho_{i+2,j} - 3\rho_{i+1,j} + 3\rho_{i,j} - \rho_{i-1,j})\right] \tag{3.13}$$

Once again, h is the cell area (volume in 3D), while the coefficients $\varepsilon^{(2)}$ and $\varepsilon^{(4)}$ vary according to the flow conditions as:

$$\varepsilon^{(2)}_{i+\frac{1}{2},j} = \kappa^{(2)} \max(\nu_{i+1,j}, \nu_{i,j}) \tag{3.14}$$

$$\varepsilon^{(4)}_{i+\frac{1}{2},j} = \kappa^{(2)} \max\left[0, \left(\kappa^{(4)} - \varepsilon^{(2)}_{i+\frac{1}{2},j}\right)\right] \tag{3.15}$$

Where:

$$\nu_{i,j} = \frac{|p_{i+1,j} - 2p_{i,j} + p_{i-1,j}|}{|p_{i+1,j}| + |2p_{i,j}| + |p_{i-1,j}|} \tag{3.16}$$

And the coefficients given by Jameson et al. [1981] are $\kappa^{(2)} = 1/4$ and $\kappa^{(4)} = 1/256$.

3.1.4 Time-marching scheme

Once the formulation of the dissipative term has been defined, equation (3.11) can be rewritten in a form convenient for the time stepping:

$$\frac{d\mathbf{w}}{dt} + \mathbf{P} = 0 \tag{3.17}$$

$$\mathbf{P} = \frac{1}{h}(\mathbf{Q} - \mathbf{D}) \tag{3.18}$$

The scheme employed is the fourth order Runge-Kutta, which is fourth order accurate in time (although the present discretisation is second order accurate in space). Its stability is given by Stetter [1973] for a Courant number:

$$\left|\frac{a\Delta t}{\Delta x}\right| \leq 2\sqrt{2} \tag{3.19}$$

Where a is the local speed of sound. The characteristic distance at each cell for the shear h-mesh used here (shown later) can be taken as the local Δx. This scheme allows the use of a variable time step for accelerated convergence.
The steps involved in advancing a the components of the solution vector from $\mathbf{w}^t$

to $\mathbf{w}^{t+\Delta t}$ are as follows:

$$\begin{aligned}
\mathbf{w}^{(0)} &= \mathbf{w}^{t} \\
\mathbf{w}^{(1)} &= \mathbf{w}^{(0)} - \frac{\Delta t}{2}\mathbf{P}^{(0)} \\
\mathbf{w}^{(2)} &= \mathbf{w}^{(0)} - \frac{\Delta t}{2}\mathbf{P}^{(1)} \\
\mathbf{w}^{(3)} &= \mathbf{w}^{(0)} - \Delta t\mathbf{P}^{(2)} \\
\mathbf{w}^{(4)} &= \mathbf{w}^{(0)} - \frac{\Delta t}{6}\left(\mathbf{P}^{(0)} + 2\mathbf{P}^{(1)} + 2\mathbf{P}^{(2)} + \mathbf{P}^{(3)}\right) \\
\mathbf{w}^{t+\Delta t} &= \mathbf{w}^{(4)}
\end{aligned} \tag{3.20}$$

Where $\mathbf{P}^{(n)}$ is obtained by computing at each step the discretization term $\mathbf{P}$ and the dissipative term $\mathbf{D}$ using variables obtained from the local solution $\mathbf{w}^{(n)}$. In order to speed up the computation it is possible to freeze the dissipation term at the first stage value, since it requires considerable computational time to evaluate D at each stage.

3.1.5 Accounting for blade rotation

The flow solver will be used to analyse turbine flows, hence it is essential to account for rotation of the blade profiles, which is not included by Jameson et al. [1981], who are dealing with stationary cascade flow only. The solver was thus modified to consider blade speed due to rotation. The change of a property w in the rotating frame is:

$$\left(\frac{\partial w}{\partial t}\right)_R = \left(\frac{\partial w}{\partial t}\right)_F + \omega\left(\frac{\partial w}{\partial \theta}\right)_F \tag{3.21}$$

In 2D the angular change is expressed as tangential:

$$\frac{\partial w}{\partial \theta} = r\frac{\partial w}{\partial y} \tag{3.22}$$

Then 3.21 becomes:

$$\left(\frac{\partial w}{\partial t}\right)_R = \left(\frac{\partial w}{\partial t}\right)_F + U\left(\frac{\partial w}{\partial y}\right)_F \tag{3.23}$$

Where $U = r\omega$. Now, the conservation integral form of the two dimensional Euler equations for inviscid flow (equation (3.4)) becomes, for rotating flows:

$$\frac{\partial}{\partial t}\iint_{\Omega} \mathbf{w} d\Omega + U \iint_{\Omega} \left(-\frac{\partial \mathbf{w}}{\partial y}\right) d\Omega + \oint_{C} (\mathbf{f} dy - \mathbf{g} dx) = 0 \tag{3.24}$$

And since (by Green's theorem):

$$\iint_{\Omega} \left(-\frac{\partial \mathbf{w}}{\partial y}\right) d\Omega = \oint_{C} \mathbf{w} dx \tag{3.25}$$

Then:

$$\frac{\partial}{\partial t}\iint_{\Omega} \mathbf{w} d\Omega + U \oint_{C} \mathbf{w} dx + \oint_{C} (\mathbf{f} dy - \mathbf{g} dx) = 0 \tag{3.26}$$

Equation 3.26 can be applied to a finite volume cell in discretized form:

$$\frac{\partial}{\partial t}\mathbf{w} \cdot h + U \sum_{k=1}^{4} \mathbf{w_k} \Delta x_k + \sum_{k=1}^{4} (\mathbf{f_k} \Delta y_k - \mathbf{g_k} \Delta x_k) = 0 \tag{3.27}$$

3.1.6 Boundary conditions

There are 4 types of boundaries for the turbine flow under consideration: inlet, outlet, solid wall and periodic boundary. The type of boundary condition at inlet and outlet depends on the nature of the flow component normal to these boundaries, i.e. the axial flow in this case, since the boundaries are aligned to the tangential (circumferential or, in 2D, y) direction. Even though the absolute flow through LP turbines is very often supersonic, the large tangential component of velocity ensures a subsonic axial component in practically all cases. The subsonic boundary conditions are therefore applied, as explained shortly.

The normal flow being analysed is subsonic at inlet, and generally speaking, it is subsonic also at the end of the outlet passage. The selection of boundary values of total pressure, total temperature and outlet static pressure has to ensure this condition: The reason for this is that subsonic and supersonic boundaries require different treatement and the solution to the flow under investigation will not converge unless inlet and outlet are subsonic (as this program is designed to

treat only this particular case).

3.1.6.1 Inflow boundary

The flow is governed by an hyperbolic system of equations; at subsonic inlet, one characteristic is propagating out of the domain, while the others propagate inside the domain together with the flow streamlines. Thus, only one variable needs to be extrapolated, while the other two are held fixed. In this case, the static pressure is extrapolated from the adjacent inner cell, through a zeroth order extrapolation in space, specially relaxed in time:

$$p_{1,j}^{t+\Delta t} = p_{1,j}^{t} + \beta \left(p_{2,j}^{t+\Delta t} - p_{1,j}^{t} \right) \tag{3.28}$$

Where β is a coefficient ($0.1 \leq \beta \leq 1$) determining the degree of relaxation in time.
A test is added in the program to make sure that the inlet static pressure computed does not exceed the inlet total pressure.
From the extrapolated static pressure, the temperature is found using the total values of pressure and temperature using the isentropic equation:

$$T = T_0 \left(\frac{p}{p_0} \right)^{\frac{\gamma-1}{\gamma}} \tag{3.29}$$

3.1.6.2 Outflow boundary

At the subsonic outflow, one characteristic is propagating back into the domain, while the others go out along with the flow streamlines. Only one variable is held fixed in this case, while all the others are left floating.
Density and velocity are extrapolated from the inner solution, while static pressure is kept constant at the prescribed outlet value.

3.1.6.3 Wall boundaries

On the blade profiles, a solid wall boundary condition must be imposed. This is done when evaluating the fluxes at the cells sides located on the blade profile: the mass fluxes and all the flux components depending on mass flux (i.e. containing

ρu or ρv, in (3.5)) are set to zero. In the case of rotating blades, the y directed components of the fluxes will be set to zero after adding the mass flux contribution due to rotation:

$$(\rho v)_k \Delta x_k - \rho_k U \Delta x_k = 0 \tag{3.30}$$

This ensures that the *relative* fluxes are zero.
Even though there is no mass flux through the wall, there will be a pressure contribution to the momentum equation. The pressure at the wall is therefore extrapolated from the interior, and accounted for, when computing the all round fluxes in (3.27).

3.1.6.4 Periodic boundaries

The imposition of periodicity at the inlet and outlet flow passage boundaries is achieved by setting the values at the boundary cell sides equal to the average between adjacent cell centres. This is easily achieved thanks to the matching x-coordinates of the grid points on the upper and lower periodic boundaries (hence no interpolation is required).

3.2 Simulations

3.2.1 Sheared H-mesh

The mesh is constructed for a cascade flow passage by splitting the blade profile at the minimum and maximum axial locations. These points are located in the LE and TE regions, but do not necessarily coincide with the LE and TE points (which, generally speaking, are at the point of maximum curvature). The flow passage is then extrapolated by following the gradient of the camber line at 5 % and 95% chord (this may vary in some cases). Splitting the blade in this way allows the representation of the blade profile through its tangential thickness distribution, and allows for a simple sheared H-mesh to be constructed. This is done by connecting upper and lower profiles of the passage with constant x lines (j directed or constant i); these are then subdivided into an equal number of segments each. The ends of the segmends will provide the nodes, which when

connected will yield the i directed mesh lines (i.e. running in the stream-wise direction). A geometric series can be used to either cluster or flare the mesh near locations such as LE, TE and walls.

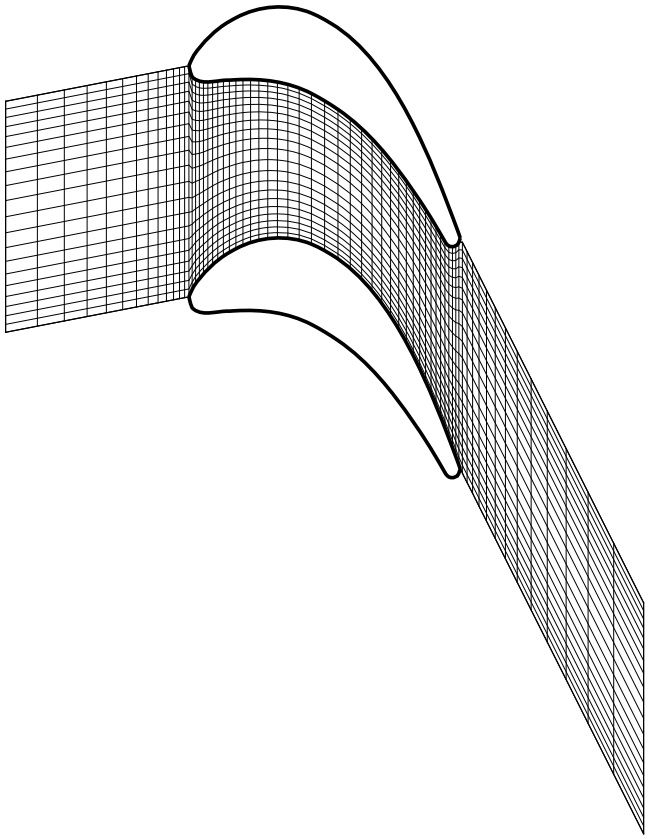

Figure 3.2: Mesh for VKI turbine blade (only every other node shown)

3.2.2 Validation

3.2.2.1 VKI cascade

Kiok et al. [1986] gathered experimental results for cascade flow over a turbine blade section, at four different European wind tunnels. The cascade blades varied in size (scaled up or down) and number (from 8 to 12) in each one of the wind tunnels. Carefully calibrated probes upstream and downstream of the cascade measured total and static pressures, and flow angle. Tappings on two central

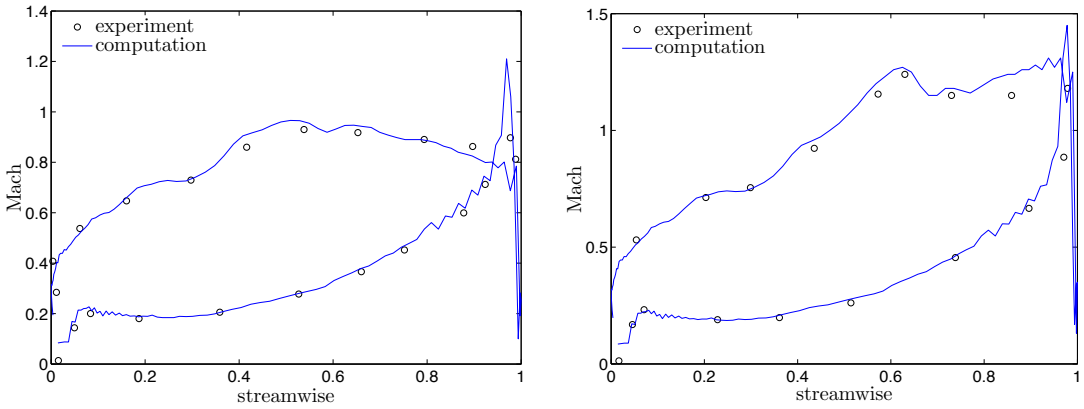

(a) subsonic case (b) transonic case

Figure 3.3: Surface Mach number comparison between VKI experiment and computation

blades provided surface pressure distributions. In their paper the authors provide the blade surface Mach number distributions for a subsonic and a transonic case. The boundary conditions used in the present numerical simulations are set to inlet total pressure of $1\,atm$, inlet total temperature $287\,K$, inflow angle 30^0; the outlet static pressure was set to $66.1\,kPa$ for the subsonic case, and $49\,kPa$ for the transonic case. The surface Mach number distributions are compared in figure 3.7. Some discrepancies are noticeable near the TE, due to the need for a finer mesh in this region. This was not attainable with the simple H-mesh used in this case, and the inviscid nature of the simulation, which fails to capture a possible boundary layer separation at the thick TE.

3.2.2.2 UTRC rotor and stator

The second experiment is the one presented in Dring and Wagner [1982], which provides blade surface pressure coefficients for stator and rotor blades of the UTRC turbine model. The inlet stagnation pressure and temperature were set to $p_0 = 100kPa$ and $T_0 = 288K$ for both rotor and stator, with outlet static pressure of $p_2 = 96.3kPa$ for the stator and $95kPa$ for the rotor. The inflow angles were $\alpha = 0^o$ and $\alpha = 67.9^o$ for the stator and rotor respectively. The rotational speed of the rotor was $410rpm$. Also in this case, the quality of the

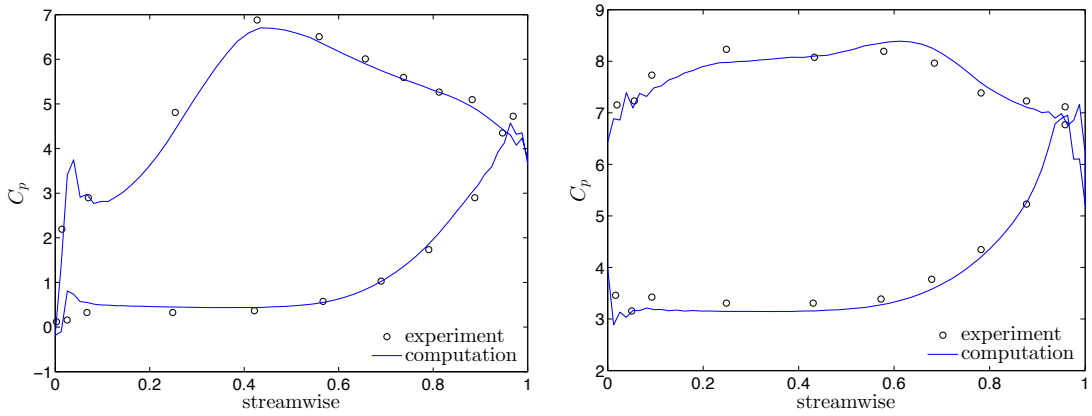

(a) stator (b) rotor

Figure 3.4: Pressure coefficient comparison between Dring's experiment and computation

computational prediction is sufficiently accurate, as shown in figure 3.4.

3.2.2.3 Steam turbine example

For the present research, the geometry of a last stage rotor was made available by the sponsor, characterised by large size, high curvture at hub, high stagger angles near the tip and decambered profiles between 50% and 80% span.
The flow solution obtained with the 2D solver for 50% span is presented here. First, the mesh independency was tested by comparing the solution obtained with different mesh sizes; in all cases mesh independence was satisfactory, and an example of this is shown in figure 3.5.
This test case was then compared with the results obtained using a well recognized commercial CFD package (Ansys CFX). The fluid modelled is steam ideal gas, with specific isobaric heat capacity $c_p = 1930\,J/kgK$ and molar mass $M = 18.2\,g/mol$. The rotational speed for the rotor under consideration is of 3600 r.p.m. and the boundary conditions were set as inlet total pressure of $32\,kPa$, inlet total temperature $343\,K$, inlet flow angle (absolute) of 75^o and outlet static pressure $5.6\,kPa$.
The mesh size for the 2D solution was set to 7500 nodes, a coarse mesh typical of a rapid inverse design procedure. This was chosen because the aim of this test

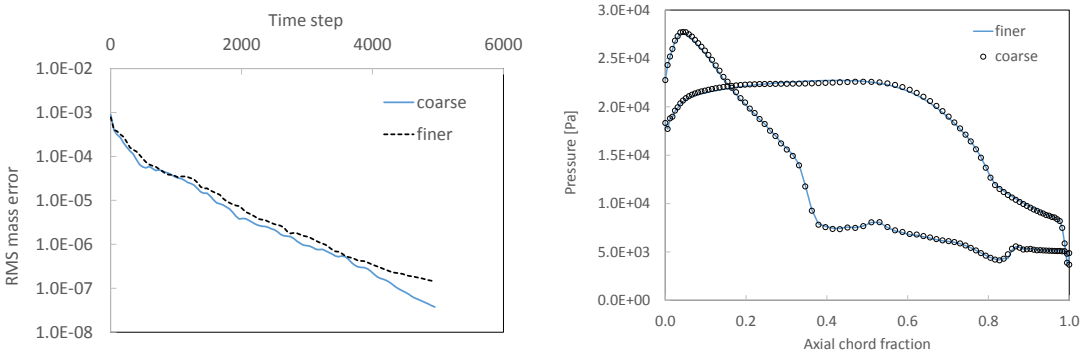

(a) Convergence history comparison

(b) Blade surface pressure comparison

Figure 3.5: Comparison between a 5k and a 12k nodes grid

was to check how a typical 2D inverse design flow solution compares to a more accurate commercial solution. The remainder of the project will focus on inverse design and blade update algorithms, rather than on adoption of more advanced CFD techniques. The flow solution for the 2D case was converged to RMS density residuals below 10^{-7}.

A simulation was set up in Ansys CFX, by redefining the two-dimensional blade profile as a constant-radius section (rather than constant z), and then extruding a thin quasi-3D blade in the radial direction. This was needed since CFX is a three-dimensional solver. The mesh for the thin blade is shown in figure 3.7b. The flow solution was based on dicretized RANS equations coupled with a $\kappa - \epsilon$ turbulence model. Convergence was set to RMS mass residuals below 10^{-5}. The boundary conditions were imposed to be the same as for the 2D in-house solver. A free-slip condition was imposed on both endwalls and on the blade surface to maintain similarity with the 2D Euler solution. A comparison between blade loadings is shown in figure 3.6. The agreement is generally acceptable on a qualitative level.

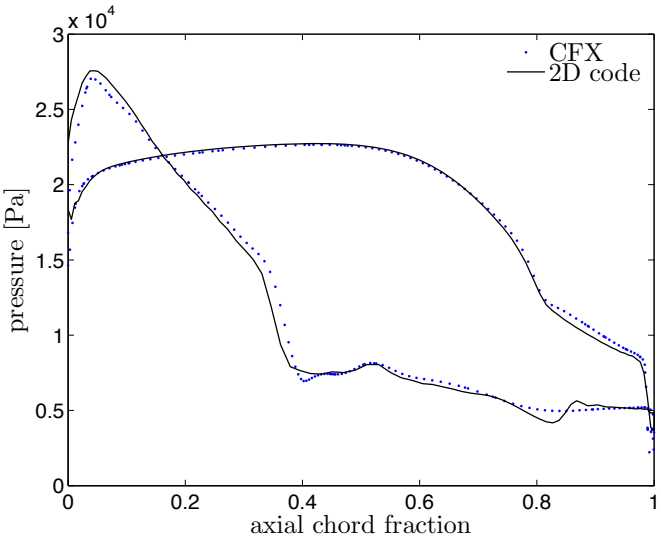

Figure 3.6: Comparison between blade loading obtained from flow solutions of CFX and 2D in-house code

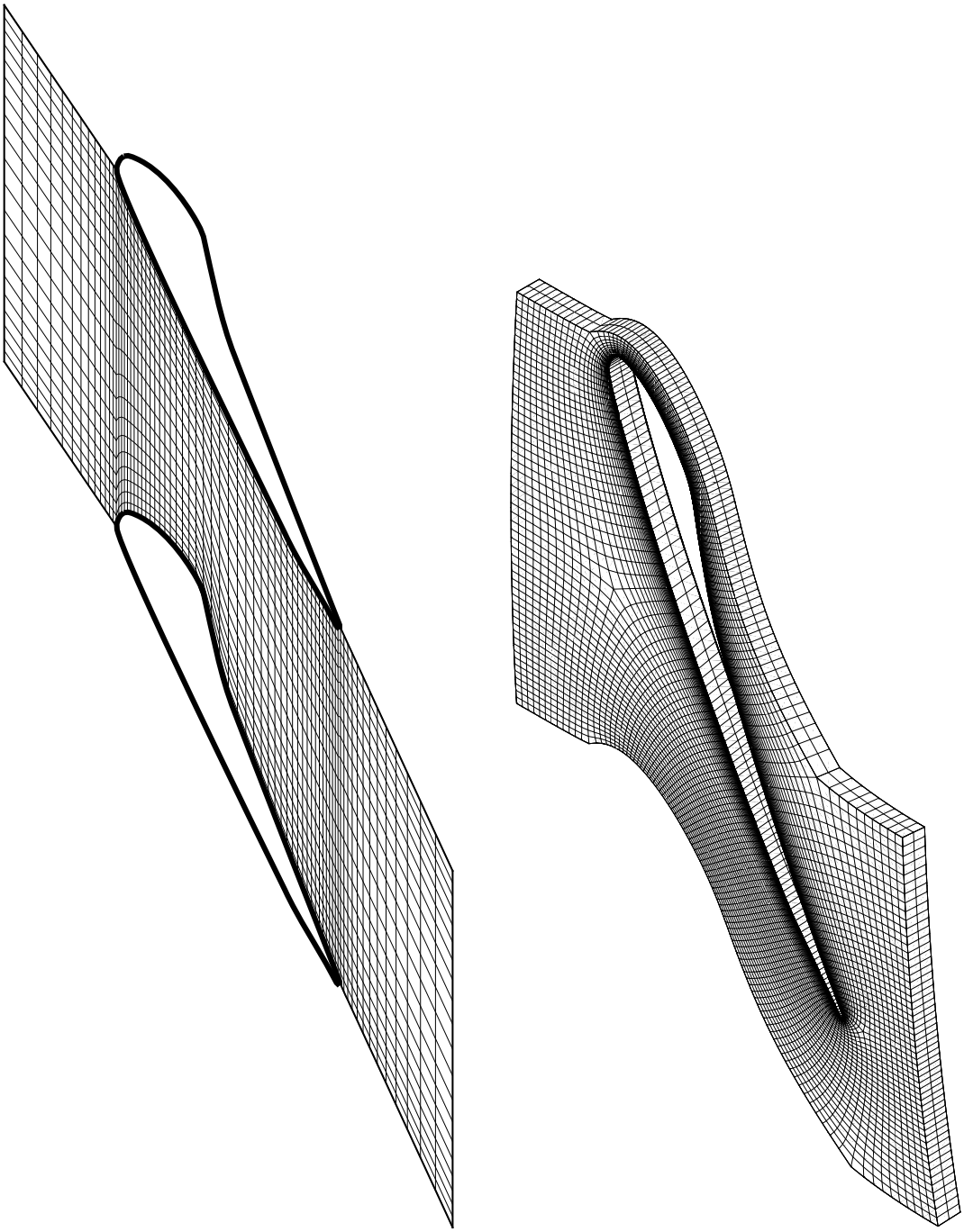

(a) 2D solver mesh (only every other node shown)

(b) quasi-2D CFX mesh

Figure 3.7: Mesh comparison between 2D code and CFX for 50% span test

Chapter 4

Water properties evaluation and equilibrium 2-phase flow

So far, the CFD solver presented treated the fluids as ideal gases. In the case of water, this approximation can be considered appropriate when dealing with dry steam, within a narrow range of pressures for which the reference specific internal energy can be adjusted. However, if more accuracy or a more versatile method is required, then a way of estimating real gas properties for water is needed. Furthermore, this will allow the computation of two-phase flows if the two phases (liquid and gas) are assumed to be in thermodynamic equilibrium.
Several unified equations of state for water have been proposed in literature. Two of the most popular formulations are the one based on the dimensionless Helmholtz function (Hill [1990]) and the IAPWS formulation based on the dimensionless Gibbs free energy (IF97 [2007]). Evaluation of any thermodynamic property can be carried out from the fundamental function and its derivatives. Generally speaking these calculations are computationally expensive in the context of CFD solutions, where properties need to be evaluated at each cell and each time step. Therefore, it is advisable to construct look-up tables of properties and derivatives, so that their values can be quickly extracted in the course of the iterative flow computation. The tabular property formulation, its implementation, and its use in 2-phase flows are the subject of this chapter.

4.1 Tabular steam property evaluation

4.1.1 Direct evaluation of thermodynamic properties (based on IAPWS IF97)

The IAPWS formulation (IF97 [2007]) provides equations for the 5 regions in figure 4.1. In the present case regions 1 for the liquid, 2 for the superheated and 4 for the saturated water and steam are considered. The equations for the saturation pressure $p_s(T)$ and temperature $T_s(p)$ were arranged in two independent subroutines.

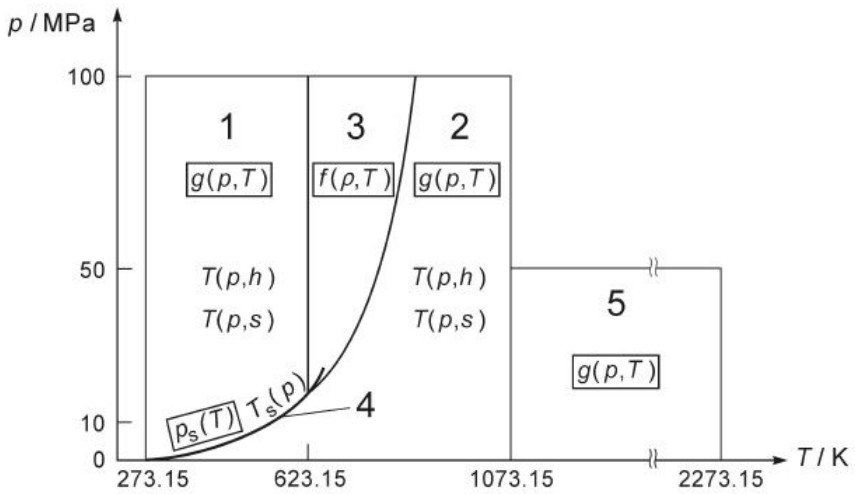

Figure 4.1: Regions and equations of IAPWS IF97 (Taken from IF97 [2007])

The dimensionless Gibbs free energy $\gamma(\tau, \pi)$ is given as function of the reduced tempretature τ and reduced pressure π, where the reducing quantity varies according to the formultion in IF97 [2007].
In the program here developed, the function $\gamma(\tau, \pi)$ and its derivatives are computed by means of two subroutines, one for region 1 and the other for region 2. The subroutine for region 2 automatically chooses the coefficients to be used in the expression for $\gamma(\tau, \pi)$ between equilibrium dry and metastable dry steam; this selection is made by comparing the input values of pressure and temperature with the saturation value given by the function $T_s(p)$ of region 4.

A set of functions was programmed, with one function for each of the thermodynamic properties (and for either liquid or gas). These functions call the subroutine for the dimensionless Gibbs free energy γ and then evaluate the property as a function of γ and its derivatives, by means of the appropriate relationships: these are given in the formulation for v, u, s, h, c_p, c_v and w. Further properties were included in this case such as the coefficient of thermal expansion $\beta = \frac{1}{v}\left(\frac{\partial v}{\partial T}\right)_p$, the coefficient of compressibility $\kappa = -\frac{1}{v}\left(\frac{\partial v}{\partial p}\right)_T$ and also the derivative $u_v = \left(\frac{\partial u}{\partial v}\right)_T$. For computational efficiency, the second derivatives in the subroutine for γ are evaluated only when needed (v, u, s, h are functions of γ and *first* derivatives only).

4.1.2 Unwrapping routines

4.1.2.1 Superheated and metastable dry: p, T functions of u, v

This routine finds values of p and T for given inputs of internal energy u_i and specific volume v_i (i subscript indicates input value in this case), by means of an iterative procedure. An initial guess for p and T is required: this can be arbitrary but better accuracy improves convergence. At each loop of the procedure, values of $\frac{\partial u}{\partial v}$, $\frac{\partial v}{\partial T}$ and $\frac{\partial v}{\partial p}$ are computed by means of the relevant functions (section 4.1.1), using as input the current values of p and T. Also u and v are computed as functions of p and T, then the differences:

$$du = u_i - u$$

$$dv = v_i - v$$

are used to find the changes in pressure and temperature:

$$dT = \frac{1}{c_v}\left[du - \left(\frac{\partial u}{\partial v}\right)_T dv\right] \tag{4.1}$$

$$dp = \frac{\left[dv - \left(\frac{\partial v}{\partial T}\right)_p dT\right]}{\left(\frac{\partial v}{\partial p}\right)_T} \tag{4.2}$$

At the end of the loop p and T are updated:

$$p = p + dp$$

$$T = T + dT$$

The procedure is repeated starting from the updated values of pressure and temperature. Convergence is typically achieved within 10 iterations (when dp and dT become sufficiently small). This routine is called during the construction of the look-up table.

4.1.3 Two-phase steam: P, y functions of u, v

This routine iterates for the wetness fraction at given mixture values of u and v with a nested iteration for the pressure of the gas phase (the partial pressure of the liquid phase in the mixture is neglected).
The value of u and v for the mixture are provided as input. An initial guess for the wetness fraction y and pressure p is also needed. These can be arbitrary, but better initial accuracy improves convergence. From the initial guess for y the specific volume of the saturated gas phase v_g is computed from the mixture v by neglecting the (very small) specific volume of the saturated liquid phase v_f:

$$v = y \cdot v_f + (1 - y)v_g \approx (1 - y)v_g \tag{4.3}$$

$$v_g \approx \frac{v}{1 - y} \tag{4.4}$$

An iterative procedure finds the value of pressure corresponding to the saturated gas specific volume, as explained shortly. Once a value of p is available the specific internal energy of the saturated liquid and gas phases u_f and u_g can be computed using the functions of region 1 and 2 respectively (section 4.1.1):

$$u_f = u_1(p, T_s(p))$$

$$u_g = u_2(p, T_s(p))$$

Hence an updated value of wetness is found:

$$y = \frac{u - u_g}{u_f - u_g} \tag{4.5}$$

Where u is the mixture input value. The procedure is repeated until convergence, i.e. when the changes in updated wetness become negligible. In the context of the present calculations, 8 loops proved to be enough.
The nested iteration to find p for a given input value of saturated gas specific volume v_{gi}, starts from an initial guess for p. The saturation temperature $T_S(p)$ is used to evaluate the saturated vapour specific volume:

$$v_g = v_2(p, T_s(p))$$

Where v_2 is the function for v of region 2 (section 4.1.1). Also, the derivatives $\frac{\partial v}{\partial T}$ and $\frac{\partial v}{\partial p}$ are evaluated by means of the available functions for β and κ at $(p, T_s(p))$. The derivative $\frac{dT}{dp}$ is computed numerically across a small increment, using the function $T = T_s(p)$. The pressure is then updated:

$$p = p + dp$$

Where the increment is given by:

$$dp = dv / \left[\left(\frac{\partial v}{\partial T} \right) \frac{dT}{dp} + \frac{\partial v}{\partial p} \right] \tag{4.6}$$

And dv is the difference between input and current value of the gas specific volume:

$$dv = v_{gi} - v_g$$

Convergence of the inner loop is achieved within 5 iterations typically.

4.1.4 Construction of the table

4.1.4.1 Superheated and metastable dry

In order to construct a table of p, T values at u, v coordinates, a rectangular region must be defined. The user inputs values of minimum and maximum pressure p_{min} and p_{max}, a value of subcooling ΔT_c and one for supreheat ΔT_h. The diagram of figure 4.2 shows the saturation line and how the rectangular region is defined. The functions for u and v used here are specified for region 2, which automatically extrapolates into the metastable region (using the appropriate metastable equation supplied by the IAPWS IF97). The minimum volume v_{min} and minimum internal energy u_{min} are found by subtracting the subcooling ΔT_c from the saturation temperature at the specified p_{max} and p_{min} respectively, along the metastable lines (dashed in figure 4.2). The maximum volume v_{max} and maximum internal energy u_{max} are found by adding the superheat ΔT_h to the saturation temperature at the specified p_{min} and p_{max} respectively. Note that the actual p_{min} and p_{max} occur at u_{min}, v_{max} and u_{max}, v_{min} respectively. These values are searched for and updated during the construction of the table. The grid is defined by n equispaced nodes in the u direction and m equispaced nodes in the v direction. At each node, the values of p and T are evaluated using the routine of section 4.1.2.1.

4.1.4.2 Equilibrium 2-phase

For the equilibrium 2-phase region, a table of p, y values is constructed at u, v coordinates. The rectangular region is specified by the input values of minimum and maximum pressure and by the prescribed maximum wetness fraction y_{max}. At this point it is useful to note that the subroutine of section 4.1.3 when used for regions defined by $y < 0.5$ and $p < 20\,bar$ returned accurate results, while convergence problems were experienced otherwise: The working range is however more than appropriate for LP turbine applications.
The u_{min} and v_{min} are computed using the maximum wetness fraction at p_{min} and p_{max} respectively. The maximum specific volume v_{max} is the saturated vapour value at p_{min}. The maximum specific internal energy u_{max} can be defined as the saturation value at either p_{min} or p_{max}. The former option will give a rectangular

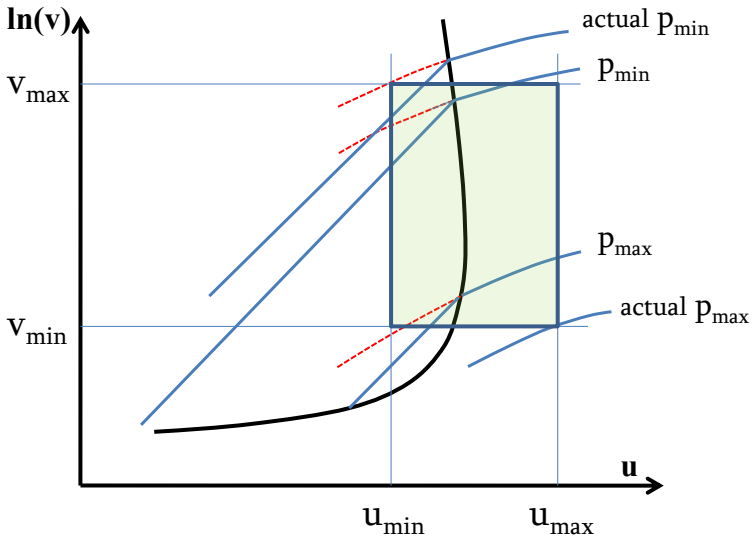

Figure 4.2: The rectangular region for the dry table. Dashed lines represent metastable constant pressure.

area as shown in figure 4.3a, where all the area is within the 2-phase region, but a small portion of low-wetness values is left out. The second option will give a rectangular area (figure 4.3b) which includes some portions of the superheated region, but with all the values of wetness fraction covered between u_{min} and the saturation line: the second option is preferred for this reason. In the superheated portion, y is set to zero and p can be computed using the routine of section 4.1.2.1. However, care is needed when looking up the table, to ensure that only wet combinations of u and v are used as inputs. This is because the derivatives used in the Taylor expansion need continuity which is not ensured across the saturation line; hence an unphysical value can be returned.

Once again, the actual p_{min} and p_{max} occur at u_{min}, v_{max} and u_{max}, v_{min} respectively; also the actual y_{max} is searched for during the construction of the table. The routine of section 4.1.3 is called at each one of the u, v coordinates at the table nodes.

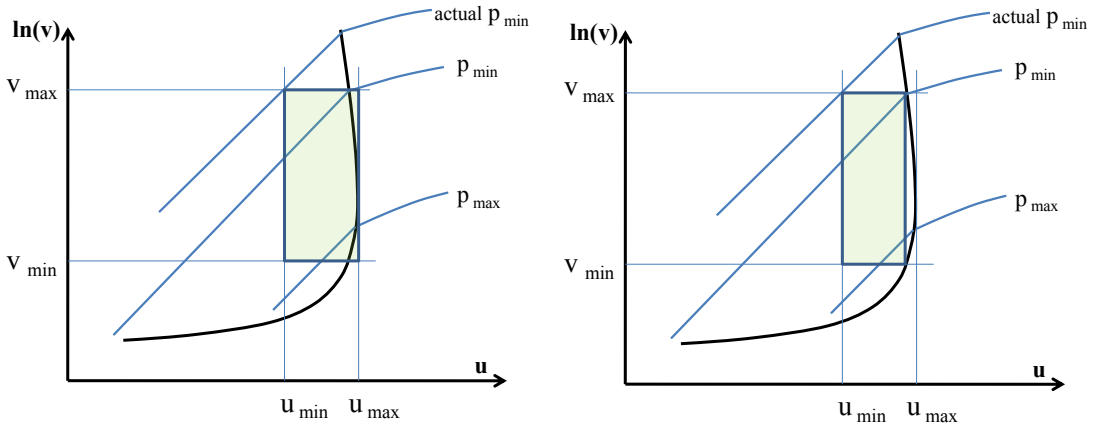

(a) u_{max} at p_{max} (b) u_{max} at p_{min}

Figure 4.3: The rectangular region for the wet table

4.1.5 Look-up method

The look-up method is the same for both tables, hence it is presented in general terms. The truncated Taylor series method adopded here was originally suggested by Hill et al. [2000], who applied it to a formualtion based on the dimensionless Helmholtz function, rather than the one based on Gibbs free energy employed in the present case.

The values of two functions f and g are stored in a table at each node i, j of coordinates x_i, y_j. The function f (or g) at x, y is then evaluated by means of a truncated Taylor series expansion about the closest point x_i, y_j

$$f = f_{i,j} + (x - x_i)\left(\frac{\partial f}{\partial x}\right)_{i,j} + \frac{1}{2}(x - x_i)^2\left(\frac{\partial^2 f}{\partial x^2}\right)_{i,j} + (y - y_j)\left(\frac{\partial f}{\partial y}\right)_{i,j} + \frac{1}{2}(y - y_j)^2\left(\frac{\partial^2 f}{\partial y^2}\right)_{i,j} + (x - x_i)(y - y_j)\left(\frac{\partial^2 f}{\partial x \partial y}\right)_{i,j} \quad (4.7)$$

The first and second derivatives at each location are computed numerically and stored during the first call to the look-up subroutine, making all the subsequent calls very rapid.

For a given input coordinate x, y the closest node is found from:

$$i = 1 + NINT\left[(x - x_{min})/\Delta x\right]$$

$$j = 1 + NINT\left[(y - y_{min})/\Delta y\right]$$

Where x_{min} and y_{min} are the minimum values on the table, at $i = 1$ and $j = 1$. The above are valid under the assuption of equispaced grid only.

4.1.5.1 Validation of steam property evaluation

The validity of the procedures of sections 4.1.4.1 and 4.1.4.2 was confirmed by comparing sample values taken from standard published steam tables (Rogers and Mayhew [1995]), to the values obtained within the rectangular regions used to construct the look-up tables. The maximum discrepancy measured within the regions was a difference in dry pressure of 0.32% near the corner of high internal energy and low specific volume. Similarly a maximum difference of 0.98% in dry temperature and 1.01% in wetness fraction. These figures are considered small errors in an evaluation of thys kind, which has rapidity as first objective. Figure 4.4b and 4.4a shows this comparison for the superheated region: a surface is constructed from the look-up table values, and at regular grid nodes some sample values from the standard steam table Rogers and Mayhew [1995] are included in the form of small cubes. Similarly, figure 4 shows comparison between the wetness fraction surface of the 2-phase look up table, and scatter values of wetness fraction extracted from the published tables. A similar validation was carried out for the pressure values of the 2-phase region. The figures show the locations at wich the values were compared and the alignment of the cubes with the surfaces suggests good matching. Further validation of the method is available in the next section 4.2.1, with the inclusion of the tables in the solver.

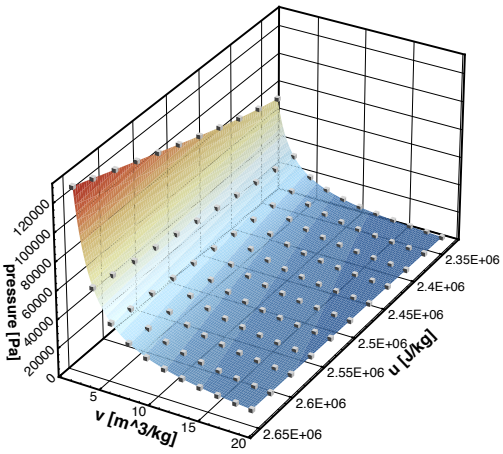

(a) dry pressure

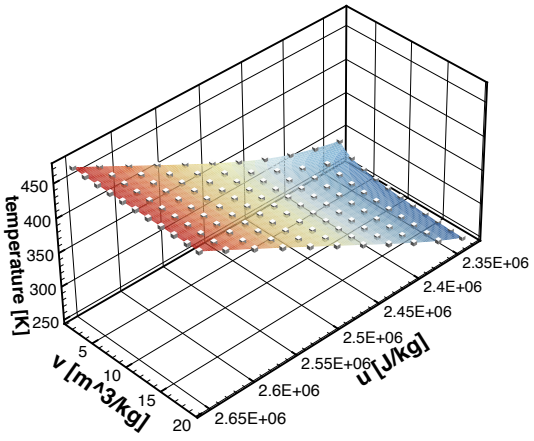

(b) dry temperature

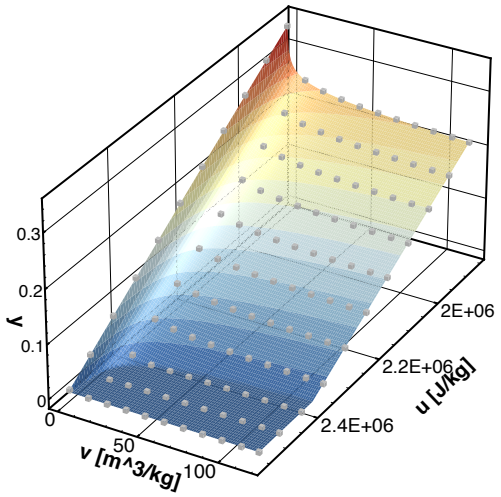

(c) wetness fraction

Figure 4.4: Comparison between values in the look-up table (surface) and sample values from standard tables (cubes)

4.2 Inclusion of equilibrium 2-phase table in Euler solver

4.2.1 Implementation

The equilibrium 2-phase table (section 4.1.4.2) was included in the 2-dimensional Euler solver for cascade flows. With this set up, the table can be used only for flows that are wet everywhere at inlet, and expand thereafter (i.e. no complete re-evaporation is expected anywhere). For flows that are superheated at inlet and nucleate in the flow passage, a stable/metastable dry table (4.1.4.1) is also needed, together with a criterion for switching from metastable dry to equilibrium wet (as suggested by Hill et al. [2000]).

The Euler solver runs as usual for the mixture (under the assumption of no inter-phase slip); values of e and ρ are returned from the energy and continuity equations. The mixture specific internal energy u is computed subtracting the kinetic term from the stagnation value e, then values of p and wetness fraction y are looked up on the table for the available u, v. The temperature is the saturated temperature.

The boundary conditions are implemented in a different way with respect to the dry solver. At inflow, the total enthalpy h_0 is specified along with a value of static entropy s, and the inflow angle α for the subsonic inlet. The static pressure p is extrapolated at each time iteration from the interior solution, with a first degree extrapolation in space relaxed in time. The total temperature is the saturated temperature corresponding to $T = T_s(p)$. Having pressure and temperature allows the computation of the specific entropy for saturated gas s_g and liquid s_f from the real gas subroutine based on the IF97. With these values and the prescribed value of s, the wetness y fraction can be found from:

$$s - s_g = y(s_f - s_g) \tag{4.8}$$

Then the enthalpy for the mixture can be computed:

$$h = h_g(1 - y) + h_f y \tag{4.9}$$

Where the values of enthaply for the saturated liquid and gas are computed using the static pressure and temperature evaluated earlier.
The magnitude of the velocity V can now be found using the prescribed value of total enthaply:

$$V = \sqrt{2(h_0 - h)} \tag{4.10}$$

The Cartesian velocity components are determined applying the prescribed inflow angle α to the velocity V.
The specific volume v is evaluated as $(1-y)v_g(p,T)$, where v_g is the function for the gas phase (the partial volume of the liquid phase is neglected).
Finally, the mixture internal energy u is evaluated using the functions for liquid and gas:

$$u = y \cdot u_f + (1-y)u_g \tag{4.11}$$

At the outflow all quantities are extrapolated as usual, imposing the outlet static pressure.
The inclusion of the superheated table (equilibrium and metastable) was more straightforward: at each time step of the flow solution, values of p and T were taken from the dry table, instead of being computed from the perfect gas relation.

4.2.1.1 Validation of dry and wet real steam property inclusion in flow solver

The solver was run in both metastable dry and equilibrium wet modes, for the convergent-divergent nozzle case presented by Binnie and Green [1942]. The authors investigated the effects of condensing steam into the nozzle flow, by varying the stagnation conditions. The steam entered the nozzle dry and expanded into the metastable region; at the onset of nucleation, a clear pressure rise was measured, known as the *condensation shock*. After this, the wet steam carried on the expansion into the 2-phase region, with conditions close to equilibrium. The metastable computation is expected to match the experiment upstream of the condensation shock. On the other hand the 2-phase computation is expected to almost match the wet portion downstream of the condensation shock, with the

measured value being slightly higher for the difference in choking mass flow and entropy increase across the condensation shock. The 2-phase computation was carried out by setting a small wetness fraction at inlet and atmospheric pressure. The nozzle geometry given in the paper was converted to a blade cascade configuration to be meshed in the. Figure 4.5 shows the comparison between computation and experiment.

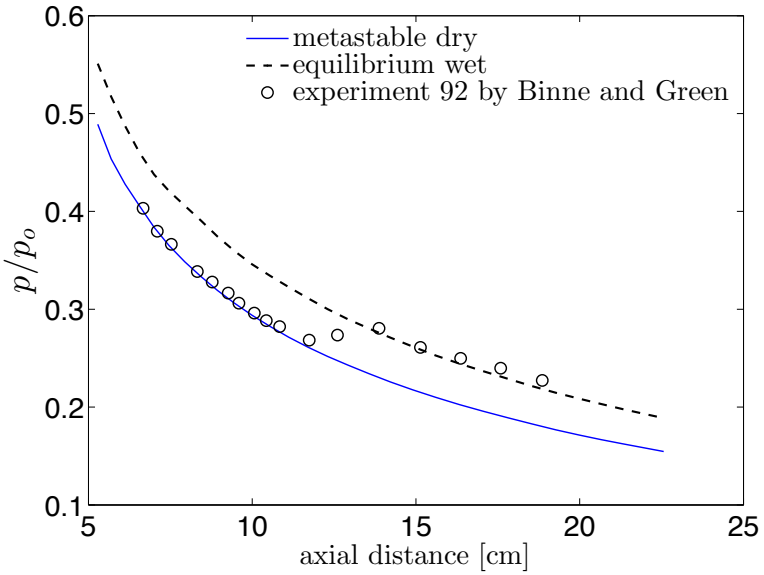

Figure 4.5: Comparison between experimental and computational pressure coefficients for condensing flow in convergent-divergent nozzle of Binnie and Green Binnie and Green [1942]

4.2.2 Further observations

The same case as in section 3.2.2.3 (50 % span, long last stage rotor) was run with ideal 2-phase fluid (wet steam). The inlet wetness fraction was imposed at the boundary to be 0.043, however when working with equilibrium 2-phase fluid the value of wetness fraction adjusts just downstream of the inlet to the equilibrium value at the inlet temperature and pressure. Figure 4.6 shows a comparison between the dry and wet blade loadings. The release of latent heat during condensation increases the level of energy hence the pressure levels. This result could potentially be making a great difference in inverse design, as the blade loading is

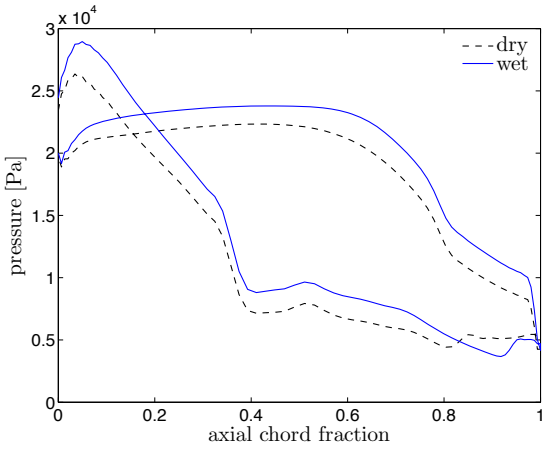

Figure 4.6: Blade loading comparison between dry steam and wet real steam simulations (50% span)

clearly affected by wetness.

Comparing the Mach number contour plots in figure 4.7 another interesting effect can be observed. As the gas expands through the turbine and work is extracted via the torque, the pressure drops and the flow becomes supersonic. The heat input due to condensation adds energy during the work extraction, hence moving the sonic line downstream. This can be observed near the throat area. A similar effect applies to the trailing edge shock, which has also moved downstream (and hits the suction surface closer to the trailing edge). Additionally it is interesting to note that even though the flow is very similar upstream of the throat, the outlet Mach number levels are lower in the wet case. This once again is due to the condensation heat release in the same way pressure levels are higher, as seen in figure 4.6).

Equilibrium 2-phase calculations can be considered appropriate for the kind of turbine under consideration: the flow is everywhere wet at inlet and no considerable secondary nucleation is expected. Generally speaking the effect on blade loading and the value of outlet liquid mass fraction can provide useful indications during the design procedure. Condensation in turbines is however very rapid and the phases do not reach equilibrium instantaneously. The effects of non-equilibrium conditions and delayed condensation are discussed in appendix. The wetness fraction contour plot for the present test case gives away the slightly

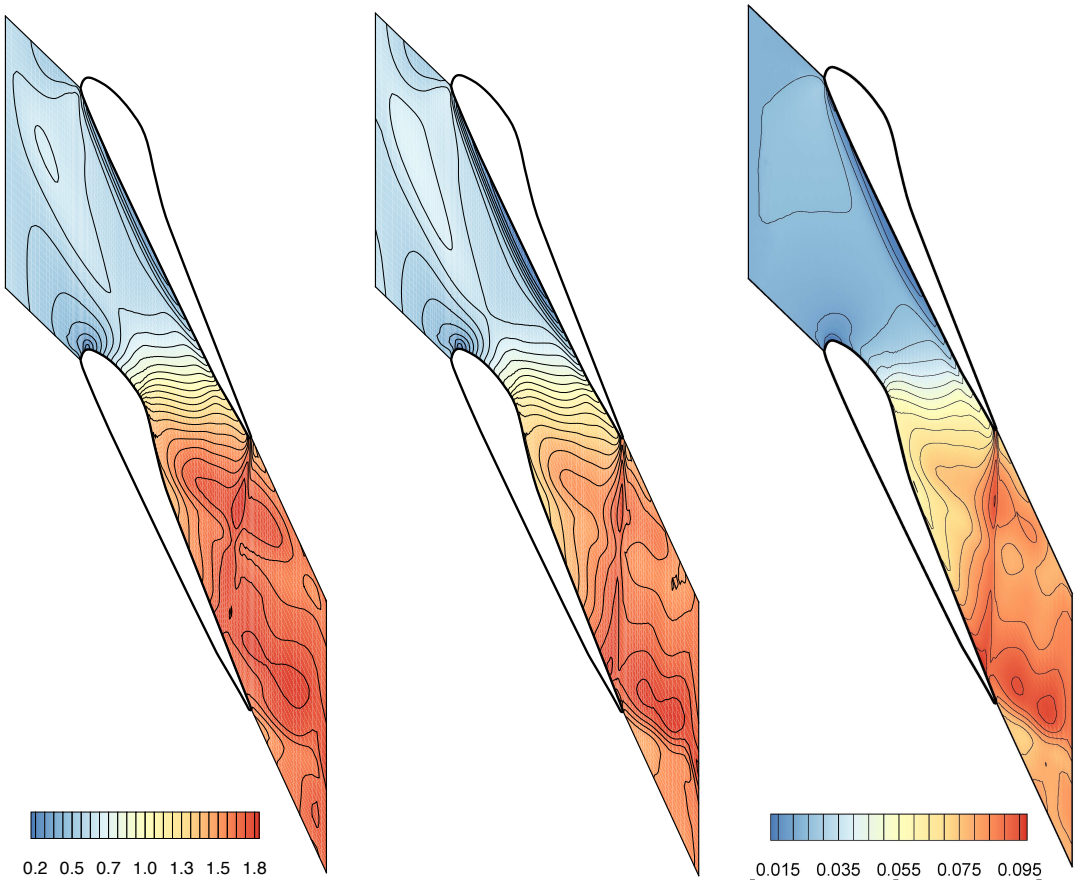

(a) dry Mach (b) wet Mach (same scale) (c) wetness fraction for wet case

Figure 4.7: Contour comparison between dry steam and wet real steam simulations

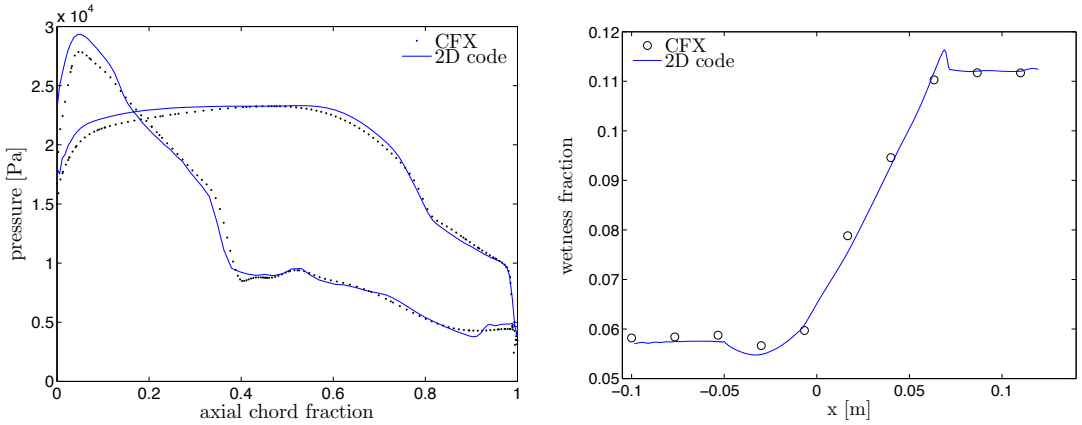

(a) Blade surface pressure

(b) Circumferentially averaged wetness fraction: inlet to outlet

Figure 4.8: Comparison of wet steam results from CFX and 2D code

fictitious nature of the equilibrium assumption: the contour plot 4.7c resembles very closely the wet Mach number contour plot in 4.7. This is because, in the equilibrium assumption, there is no delay between changes in gas properties and condensation.

4.2.3 Comparison with commercial software

A comparison with commercial software (Ansys CFX) was carried out, with similar procedure to the one in section 3.2.2.3. The same thin 3D mesh as before (figure 3.7b) was employed. The flow solution was based on RANS equations with $\kappa - epsilon$ turbulence model. Convergence was set to RMS mass residuals below 10^{-5}. Additionally the IAPWS table generation utility in CFX was employed for the 2-phase fluid wet steam. The blade loading plot 4.8a shows good qualitative agreement between commercial and in-house solutions. Some discrepancy is observed near LE, perhaps as the result of a different way of imposing inlet wetness fraction and consequent effect on incidence angle. There is also good agreement in the prediction of wetness mass fraction: figure 4.8b shows the circumferentially area-averaged liquid mass fraction, from inlet to outlet.

Chapter 5

Inverse design: a first general method

5.1 The swirl velocity method

The inverse design strategy is the one based on the prescription of the swirl velocity rV_θ distribution, as formulated by Tiow [2000]. The meridional derivative of the swirl velocity $\frac{\partial rV_\theta}{\partial x}$ is proportional to the blade loading (Hawthorne et al. [1984], Zangeneh [1991], Tiow and Zangeneh [2000]), hence there is direct control over loading when prescribing a rV_θ distribution. Furthermore, by the Euler equation of turbomachinery:

$$\dot{W} = \dot{m}\omega(rV_\theta|_{out} - rV_\theta|_{in}) \tag{5.1}$$

gives the work output, hence specifying inlet and outlet values of swirl velocity effectively fixes the turbine work. Another advantage of this method is the easy coupling with an existing flow solver such as the H-mesh based Euler solver presented in chapter 3.

Noting that the dimension of rV_θ is a velocity (r is radius and V_θ is an angular velocity), in 2D the swirl velocity reduces to the tangential velocity component V_y, "tangential" meaning in the instantaneous blade velocity direction. The cir-

cumferentially mass-averaged tangential velocity is:

$$\tilde{V}_y = \frac{\int_0^S V_y \rho V_x \, dy}{\int_0^S \rho V_x \, dy} \tag{5.2}$$

Where the tilde describes circumferentially mass-averaged values, and the notation V_x and V_y for the Cartesian components of velocity. The integration is performed across the passage from the suction surface at 0 to the pressure surface at S.
A value of $\tilde{V}_y$ is prescribed for the blade at each axial location. Its first derivative in the meridional (axial for 2D) direction represents the blade loading. The blade update algorithm modifies the blade on the basis of the difference between the prescribed $\tilde{V}_y^*$ and the current $\tilde{V}_y^0$ evaluated from the Euler solution. At each step the blade geometry and the computational mesh are updated, then a new flow solution is computed by means of the Euler solver, together with a new $\tilde{V}_y$ distribution. The procedure is repeated until a satisfactory matching is attained between the computed and the prescribed $\tilde{V}_y$ distributions.

5.2 Blade update algorithm

The sheared H-mesh used in this case is particularly suited to this methodology; the $\tilde{V}_y$ of equation 5.2 is easily computed at each axial location by integrating along a column of computational cells.
This type of mesh is also closely linked to the way the blade profiles are defined using the tangential thickness, which is the distance between lower and upper profiles of the 2D blade at any given x-coordinate. Since also the sheared H-mesh is described by constant x lines, the blade profile points will link neatly across the blade passage.
In 2D cascade arrangement, each of the n_{bl} blades is represented by their upper and lower surfaces $\alpha^{\pm}$:

$$\alpha^{\pm} = y - f^{\pm}(x) = nS \qquad n = 0, 1, 2, ..., n_{bl} - 1 \tag{5.3}$$

Where y is the tangential direction coordinate (in 2D), S is the blade pitch

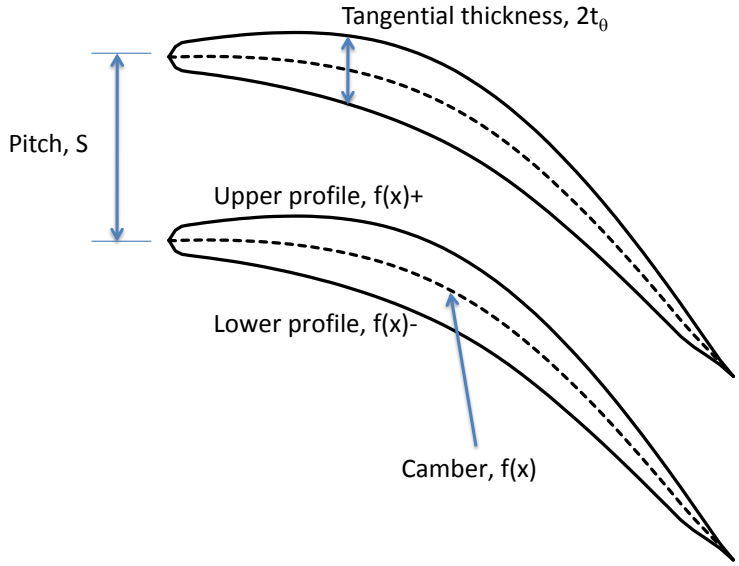

Figure 5.1: Blade profile definition as a function of x, obtained by adding the tangential thickness to the camber

and $f^{\pm}(x)$ describe the upper and lower profiles of the blade section. In the method under consideration, the blade profiles are described by a camber line $f(x)$ and a tangential thickness $t_\theta(x)$, thus:

$$f^{\pm} = f \pm \frac{1}{2} t_\theta \tag{5.4}$$

During the design procedure, the camber line is updated according to the prescribed $\tilde{V}_y$, and then the blade thickness is imposed to obtain the new blade profile. The formula used to update the camber line is derived as follows. The tangency condition is imposed at walls:

$$\vec{V}^{\pm} \cdot \nabla \alpha^{\pm} = 0 \tag{5.5}$$

Which becomes, using the definition of $\alpha^{\pm}$ and expanding:

$$\begin{pmatrix} V_x^{\pm} & V_y^{\pm} \end{pmatrix} \begin{pmatrix} -\frac{\partial f^{\pm}}{\partial x} \\ 1 \end{pmatrix} = 0 \tag{5.6}$$

Multiplying and using 5.4:

$$V_x^{\pm}\frac{\partial}{\partial x}\left(f \pm \frac{1}{2}t_\theta\right) = V_y^{\pm} \tag{5.7}$$

Adding the expressions for upper and lower surfaces together:

$$V_x^{+}\frac{\partial}{\partial x}\left(f + \frac{1}{2}t_\theta\right) + V_x^{-}\frac{\partial}{\partial x}\left(f - \frac{1}{2}t_\theta\right) = V_y^{+} + V_y^{-} \tag{5.8}$$

and rearranging:

$$(V_x^{+} + V_x^{-})\frac{\partial f}{\partial x} + \frac{1}{2}(V_x^{+} - V_x^{-})\frac{\partial t_\theta}{\partial x} = V_y^{+} + V_y^{-} \tag{5.9}$$

Defining blade average values:

$$V_{xbl} = \frac{1}{2}(V_x^{+} + V_x^{-}) \qquad V_{ybl} = \frac{1}{2}(V_y^{+} + V_y^{-}) \tag{5.10}$$

and blade difference value:

$$\Delta V_{xbl} = V_x^{+} - V_x^{-} \tag{5.11}$$

Then 5.9 can be written as:

$$V_{xbl}\frac{\partial f}{\partial x} + \frac{1}{4}\Delta V_{xbl}\frac{\partial t_\theta}{\partial x} = V_{ybl} \tag{5.12}$$

This expression relates the camber to the tangential velocity. For an initial camber f^0, 5.12 is written as:

$$V_{xbl}^{0}\frac{\partial f^0}{\partial x} + \frac{1}{4}\Delta V_{xbl}^{0}\frac{\partial t_\theta}{\partial x} = V_{ybl}^{0} \tag{5.13}$$

The assumption here is that the tangential thickness remains constant. For the new geometry (with camber f^1), an approximation is made that will eventually satisfy the prescribed $\tilde{V}_y^*$ (the star designates a prescribed value):

$$V_{xbl}^{0}\frac{\partial f^1}{\partial x} + \frac{1}{4}\Delta V_{xbl}^{0}\frac{\partial t_\theta}{\partial x} = V_{ybl}^{0} + \tilde{V}_y^{*} - \tilde{V}_y^{0} \tag{5.14}$$

Now, subtracting 5.13 from 5.14 yields:

$$V_{xbl}^0 \frac{\partial}{\partial x}(f^1 - f^0) = \tilde{V}_y^* - \tilde{V}_y^0 \tag{5.15}$$

This is the equation used to update the camber at each step of the inverse design algorithm. Equation 5.15 is integrated numerically in the axial direction, using trapezium rule (with first order forward difference in space). A "stacking point" x_0 is needed to be used as starting point for the integration. This camber point is fixed and does not move during the procedure. Generally speaking the leading edge point can be chosen, or a point close to the leading edge in which case the portion upstream of the stacking point needs to be reconstructed with some specific technique (introduced later). Alternatively, any point on the camber can be chosen to be the stacking point, and the integration of 5.15 needs to be performed both upstream and downstream of this point along the camber line. The integration of 5.15 is performed over n intervals, from the stacking point x_0 to a cut-off point x_n, which could be the trailing edge point, or a point upstream if then the trailing edge is reconstructed. The advantage of an H-mesh is that flow values are readily available at cell-centres between any two camber point abscissae, and also the remeshing is easily performed since the x coordinates are kept constant.
Note that for rotating blades, all the velocity values described above refer to *relative* velocities.

5.3 Results and discussion

5.3.1 Basic test for inverse design: blade recovery

A simple way of testing the operation of the inverse design procedure consists of recovering a known blade profile by prescribing its $\tilde{V}_y$ distribution. This involves three steps:

1. Analysing a given blade profile to obtain the $\tilde{V}_y$ distribution from the flow solution.

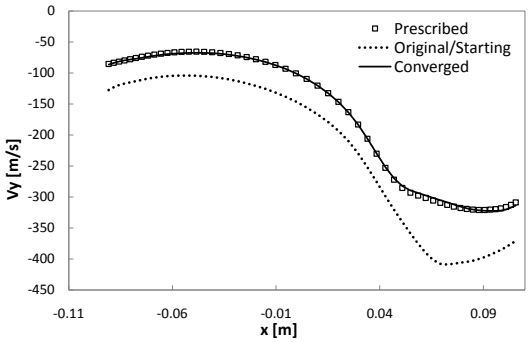

(a) mass averaged swirl $\tilde{V_y}$ at 30% span

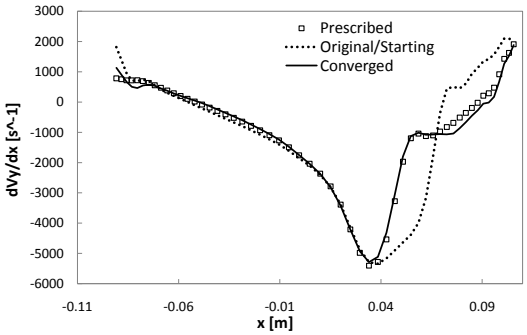

(b) loading $\partial\tilde{V_y}/\partial x$ at 30% span

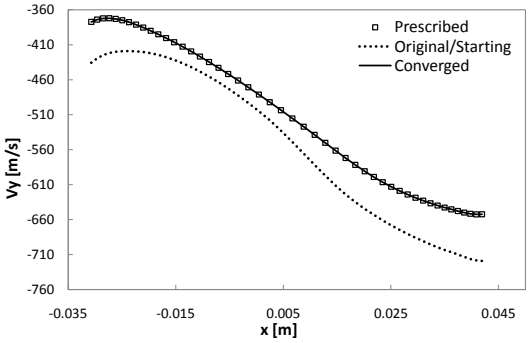

(c) mass averaged swirl $\tilde{V_y}$ at 100% span

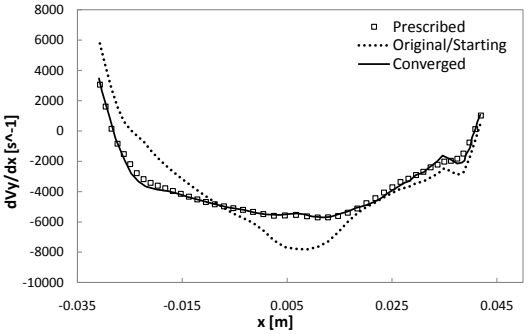

(d) loading $\partial\tilde{V_y}/\partial x$ at 100% span

Figure 5.2: Blade recovery at different span sections

2. Modifying the blade profile by arbitrarily altering its camber (and imposing the original thickness).

3. Starting from the modified profile, run the inverse design procedure prescribing the $\tilde{V_y}$ distribution of the original blade

As the $\tilde{V_y}$ distribution gets closer to the specified target, the computed blade profile should eventually match the original one. At each blade update the maximum blade modification is measured as a fraction of the maximum camber point displacement to axial chord length. When this ratio falls below 0.001, the inverse procedure is exited. The test was performed at different span sections of the 50in last stage blade considered in this research (hub, 30% span, 50%, 75% and tip). The shape was recovered by the code in all cases, with a maximum error of 0.092%, measured as the ratio of maximum discrepancy to axial chord length (discrepancy being the difference in tangential direction between original

and computed camber line points). Some sample results for 30% span and tip are presented here.

Figure 5.3a shows the original profile (marked by the small squares) and the modified blade used as starting geometry (dotted) for the inverse design. Figure 5.2a shows the $\tilde{V}_y$ distribution for the original, modified and recovered blade profiles. The prescribed distribution is the original one in the case of a blade recovery. Figure 5.2b shows the meridional (in the x direction for 2D) derivative of the swirl, as this is directly proportional to blade loading (i.e. pressure jump between suction and pressure surface). The small discrepancies near TE observed in the meridional derivative are mainly due to numerical differentiation errors in the typically coarse camber point distribution used in inverse design, and are considered negligible in common practice, since what is used to drive blade modifications is $\tilde{V}_y$ and not $\frac{d\tilde{V}_y}{dx}$, which is only shown for illustration purposes. The same test was performed at the tip section. The blade profile convergence is shown in figure 5.3, while the relevant $\tilde{V}_y$ and $\frac{d\tilde{V}_y}{dx}$ curves are shown in figure 5.2.

5.3.1.1 Notes on convergence

In order to recover the original profile correctly, the initial flow analysis has to reach excellent level of convergence, measured in this case by values of RMS density residuals of less than 10^{-8}. This initial solution is used to get the $\tilde{V}_y$ distribution to be prescribed on the modified camber. If the convergence of the analysis is not accurate enough, the inverse design will converge to a slightly different shape. During the inverse design procedure each of the flow solutions also needs to be fully converged for best results, and usually the criterion was set as RMS density residuals lower that 10^{-6} set and a blade update was performed after each convergence. After each update the solver starts using as initial conditions the flow solution from the previous analysis. As the blade profile converges to its final shape, and camber modifications reduce, convergence of the solver becomes faster. The procedure stops once the $\tilde{V}_y$ distributions match closely enough, or when blade modifications are negligible. The final run is usually converged to lower RMS values, in order to obtain a good flow solution of the resulting design. Figure **??** shows the convergence pattern of the inverse design procedure for this

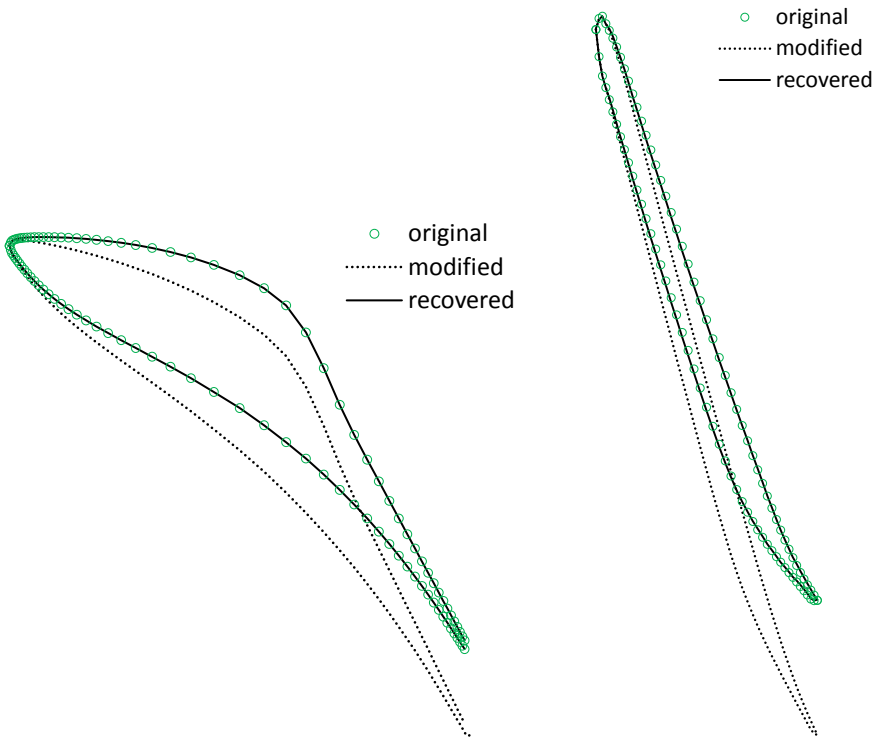

(a) 30% span (b) 100% span

Figure 5.3: Original blade recovered from a modified profile

blade recovery.

5.3.2 Inverse design with equilibrium 2-phase steam

5.3.2.1 Generic LP turbine tip section

A generic low pressure (LP) turbine tip section was taken in consideration for the present test case. The blade profile, with a subset of the mesh employed are shown in figure 5.5. Two flow simulations were run, with the boundary conditions (BC) of table 5.1. The blade surface pressures for the dry metastable and wet equilibrium flow solutions are shown in figure 5.6a: as expected the pressure levels in the wet steam case are higher due to the release of latent heat of condensation. This of course affects also the $\tilde{V}_y$ and $\partial\tilde{V}_y/\partial x$ (figure 5.6b), which in turn determine the outcome of the inverse design. This section will show the

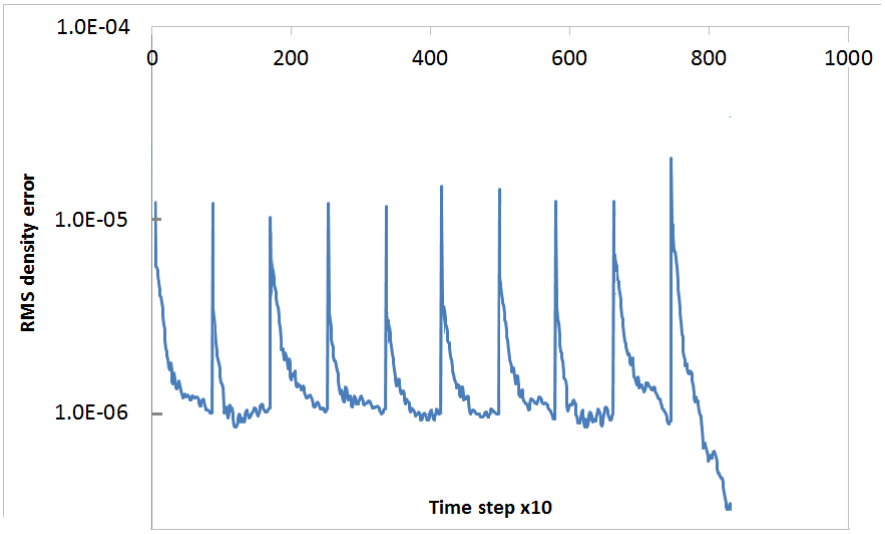

Figure 5.4: Convergence pattern of inverse design procedure

Table 5.1: Boundary conditions for LP tip section flow analysis

Fluid type	Dry metastable	Wet equilibrium
Inlet wetness mass fr. y	0.0	0.001
Inlet p_o **[kPa]**	32.0	32.0
Inlet T_o **[K]**	343.0	343.0
Inflow abs. flow angle α **[deg]**	77.0	77.0
Outlet p **[kPa]**	20.0	20.0
RPM	21945	21945

effect of using wet steam on the resulting geometry.

5.3.2.2 Dry and Wet inverse design

First, a blade recovery was run in dry and wet modes, starting from a modified version of the LP tip profile. In each case the blade recovery was run in the same way as explained in section 5.3.1, but this time prescribring the dry and wet $\tilde{V}_y$ distributions respectively. These are shown in figure 5.6b. As before the exit criterion of the inverse procedure was set to be a camber point y coordinate (tangential direction) modification inferior to 0.1% of the axial chord.
In both cases, the baseline geometry was recovered with excellent accuracy, with

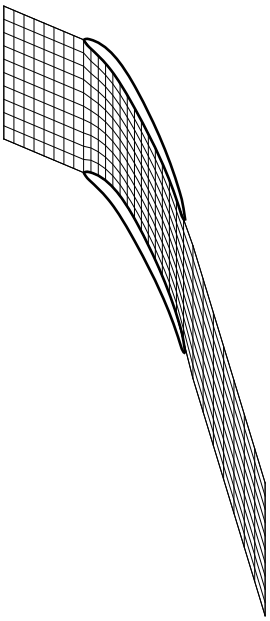

Figure 5.5: Mesh of the LP blade tip passage. This is a subset, not all nodes are shown

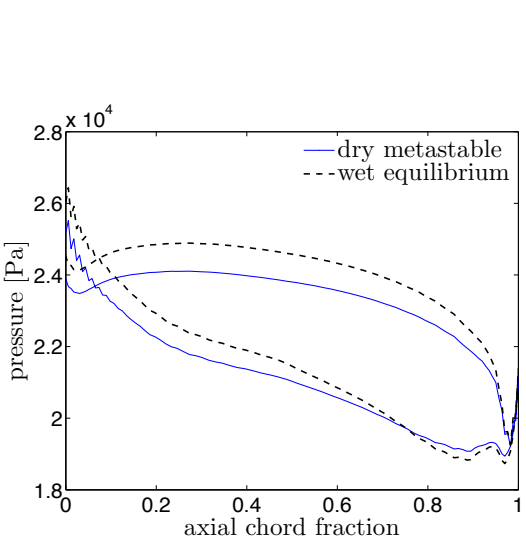

(a) blade surface pressure

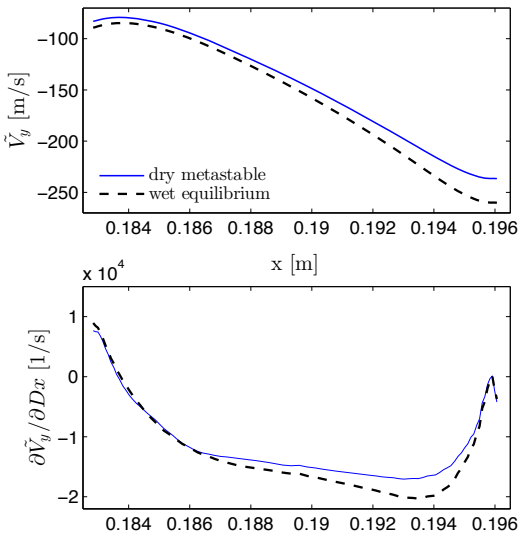

(b) $\tilde{V}_y$ and $\partial\tilde{V}_y/\partial x$

Figure 5.6: Comparison between results in wet and dry modes of the solver for the LP tip section

a maximum dicrepancy in camber point y coordinate of 0.22% between computed and original blade.

It was then attempted to redesign the LP turbine blade tip profile using the two different inverse design procedures, in dry and wet steam modes. A general practice for this kind of profiles is to aim for a more aft-loaded configuration.

Figure 5.6b shows the differences in swirl velocity $\tilde{V_y}$ and blade loading $\partial\tilde{V_y}/\partial x$ distribution between dry and wet flow solutions. With same boundary conditions (table 5.1), the blade produces more work output when the working fluid is 2-phase steam: this can be seen by inspection of figure 5.6b, since the difference between inlet and outlet $\tilde{V_y}$ is greater for the wet case, and by the 2 dimensional Euler equation of turbine work:

$$\dot{w} = \dot{m}U(\tilde{V}_{y_{(1)}} - \tilde{V}_{y_{(2)}}) \tag{5.16}$$

The difference $\tilde{V}_{y_{(1)}} - \tilde{V}_{y_{(2)}}$ is also represented by the absolute value of the area between the $\partial\tilde{V_y}/\partial x$ curve and the x axis: this is clearly greater for the wet case in figure 5.6b.

For the redesign, a slightly more aft-loaded $\partial\tilde{V_y}/\partial x$ distribution was prescribed, as shown (identical for both cases) in figure 5.7a and 5.7b. The values of inlet and outlet swirl velocity were chosen to be the values from the wet flow analysis, since these resulted in slightly higher work output. This can be observed in figures 5.7a and 5.7b, where the inlet and outlet $\tilde{V_y}$ of baseline and prescription match for the wet case but not for the dry case.

Thus, the two inverse designs were run, with same prescription but using dry and wet steam respectively. The exit criterion of the inverse procedure was set for camber point modifications in the y direction of less than 0.5% of axial chord, and each flow solution was converged to RMS density residuals below 10^{-6}.

In both cases the prescribed and computed swirl velocities match to a satisfactory level (as shown in 5.7a and 5.7b) and the exit criterion was met within 9 iterations. Some discrepancies can be observed near the leading edge (LE) due to the fact that in this region the blade update algorithm does not modify the camber, but rather the LE is reconstructed using a rotation of coordinates about the stacking point (a method devised for the present case).

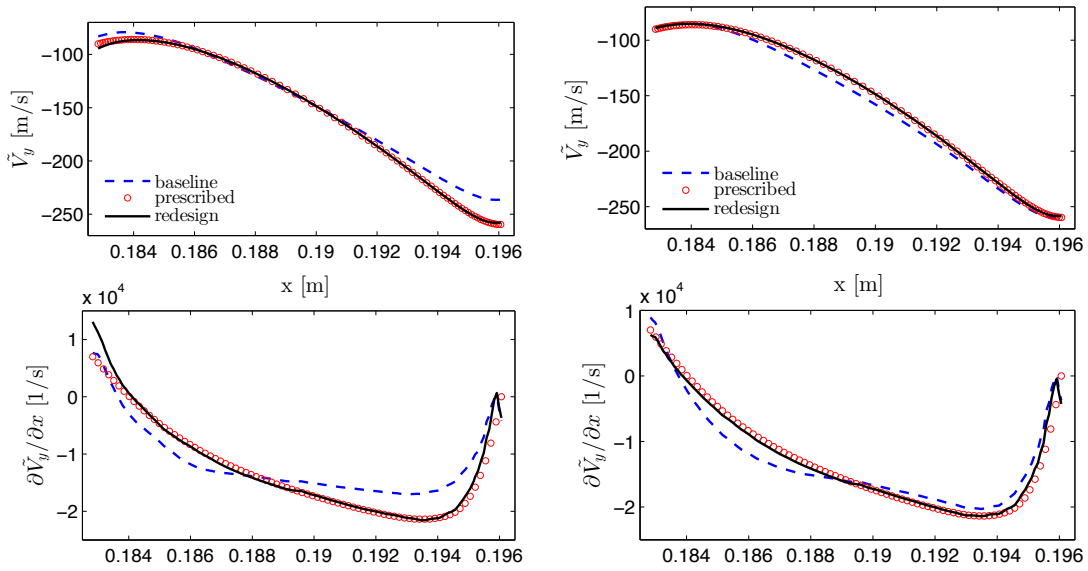

(a) dry mode (b) wet mode

Figure 5.7: The baseline, prescribed and obtained $\tilde{V}_y$ and $\partial\tilde{V}_y/\partial x$ for the LP tip section

Certainly the most interesting aspect of this whole exercise is that the two procedures produced different geometries (figure 5.8) for the same blade loading prescription; note that for this kind of high-reaction machine, small changes in geometry result in noticeable changes in aerodynamic behaviour. After obtaining the two different blades in traditional dry mode and with the new wet steam inverse design, their performance can be compared by analysing the flow solution in the actual operating conditions, i.e. in 2-phase steam flow. The Mach number contours for the two redesigns (with 2-phase wet steam as working fluid) are shown in figure 16: the blade designed in dry mode shows generally speaking higher Mach levels near the trailing edge, with peak value of 0.74 as opposed to the peak 0.69 obtained in the wet mode redesign. Furthermore, a zone of stagnation is visible adjacent to the pressure surface in the dry redesign. These flow features result in the isentropic efficiency being 1% lower for the dry redesign as compared to the wet redesign. Additionally, a wet steam simulation was run for the dry-mode redesign: figure 5.10 shows that the wet flow operating blade loading of the dry redesign does not match the prescription any more, with higher peak value of loading (resulting in higher peak Mach number). This emphasizes

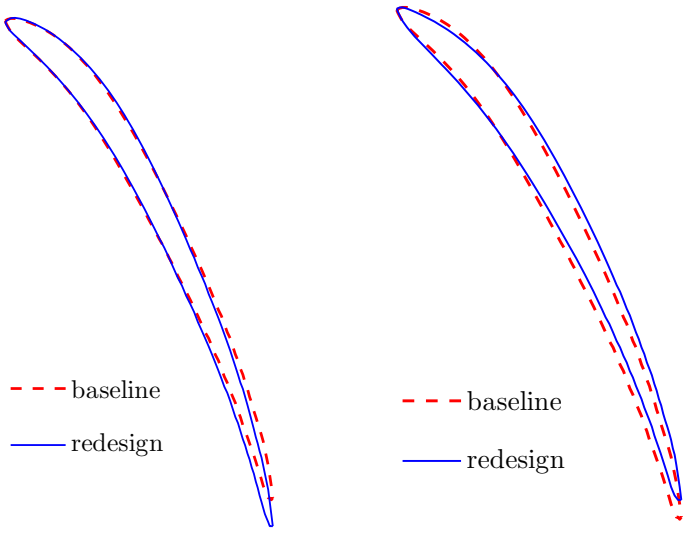

(a) dry mode (b) wet mode

Figure 5.8: Comparison between baseline and redesigned profiles of LP tip section; the inverse design was run in dry and wet modes respectively

the negative effects of inverse-designing under a dry steam assumption a blade which is supposed to operate in wet flow.

5.3.3 Long last stage blade test redesigns: arbitrary loading

The swirl velocity inverse method has been employed in variety of applications (as listed in section 2.2). In order to test the robustness of the methodology when applied to the long, last-stage geometry, some of the original blade sections were redesigned with the preocedure descibed in this chapter, imposing some arbitrary loading. This was done as an exercise to investigate the effectiveness of the procedure and possible problems, not as an attempt to produce an improved design.

5.3.3.1 30% span

A swirl velocity distribution corresponding to a parabolic loading was imposed keeping the original inlet and outlet tangential velocities (to preserve the same

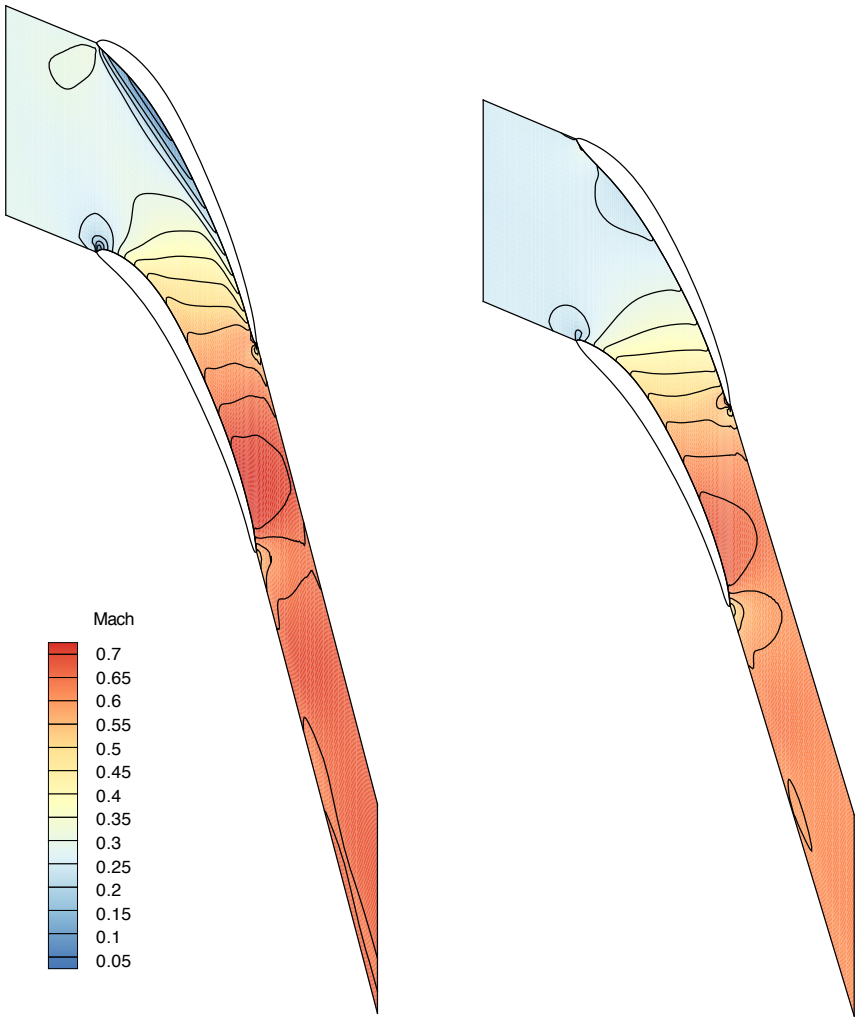

(a) dry mode (b) wet mode

Figure 5.9: Mach number contours obtained by analysing the two redesigned blades using the two-phase solver

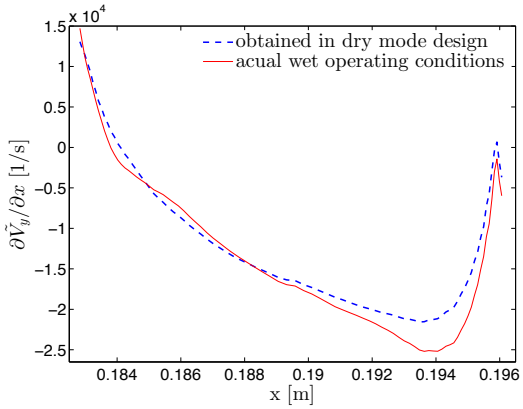

Figure 5.10: The $\partial \tilde{V}_y/\partial x$ distribution of the blade designed in dry mode, when actually operating in wet steam conditions

Euler work). The inverse procedure was run until camber point modifications fell below 1% of axial chord lenght, with convergence of each flow solution set at RMS density error below 10^{-6}. The parabolic $\frac{d\tilde{V}_y}{dx}$ distribution and the original one are shown in figure 5.11b, together with the one obtained from inverse design; the corresponding $\tilde{V}_y$ in figure 5.11a. Note that the tangential thickness is preserved in the current methodology: however the normal thickness (perpendicular to camber line) may vary, as clearly observable in this case (figure 5.12a). The shape obtained is rather unusual and most likely not an optimal design, but it gives the prescribed blade loading, which is the objective of the current exercise. Better knowledge of a reasonable prescribed loading will result in a more practical design. Incidentally, the computed total-to-total isentropic efficiency increased by 1.5% as a result of the reduction in peak Mach number.

5.3.3.2 50% span

Another test redesign was run at 50% span, prescribing a parabolic loading ($\frac{d\tilde{V}_y}{dx}$) and keeping constant inlet and outlet tangential velocities. The convergence criteria for the inverse procedure were set as before at 1% blade modification and RMS below 10^{-6}. The original, prescribed and obtained $\tilde{V}_y$ and $\frac{d\tilde{V}_y}{dx}$ are shown in figures 5.11c and 5.11d. Once again, the discrepancies observed near LE and TE are due to the fact that the blade can not be updated in these regions, and this issue will be discussed in the next section, and the imprecisions in $\frac{d\tilde{V}_y}{dx}$ are also

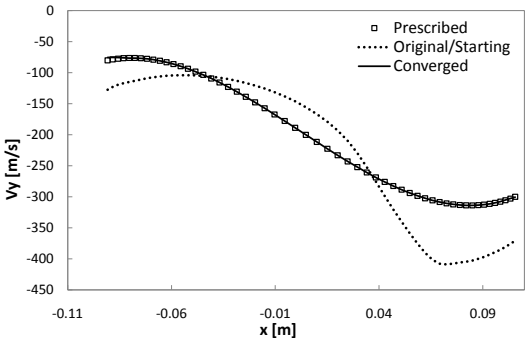

(a) mass averaged swirl $\tilde{V_y}$ at 30% span

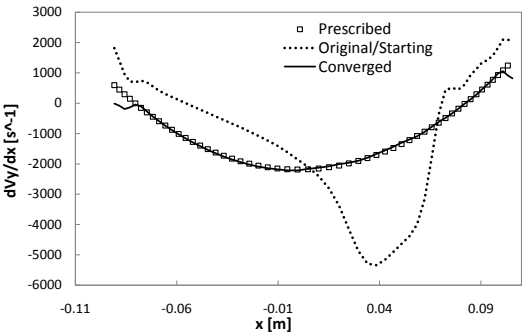

(b) loading $\partial\tilde{V_y}/\partial x$ at 30% span

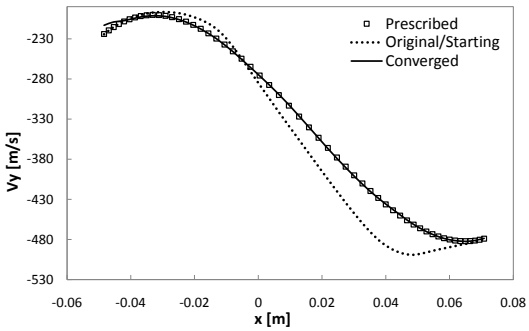

(c) mass averaged swirl $\tilde{V_y}$ at 50% span

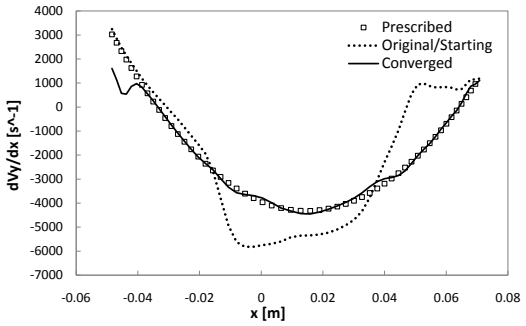

(d) loading $\partial\tilde{V_y}/\partial x$ at 50% span

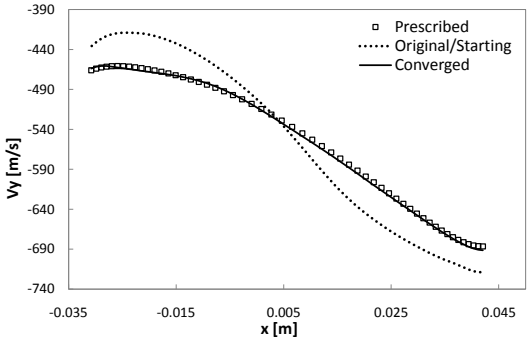

(e) mass averaged swirl $\tilde{V_y}$ at 100% span

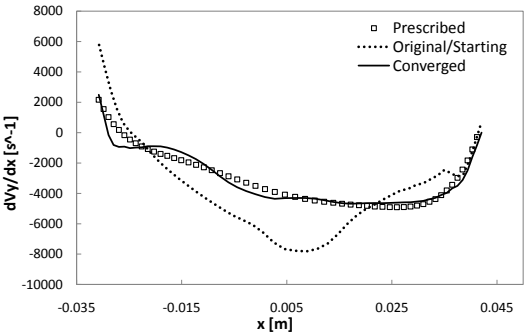

(f) loading $\partial\tilde{V_y}/\partial x$ at 100% span

Figure 5.11: Blade redesign at different span sections

due to numerical differentiation errors on a coarse grid.
This test case showed some limitations of the method under consideration. The two main areas of concern are the LE treatment and the structural infeasibility due to the reduction in normal thickness. Keeping the first few camber points fixed and modifying downstream results in LE shape distortion, as shown in figure 5.12b This has an effect on the loading in figure 5.11d where the curve does not match the prescription. Furthermore, defining the profiles in terms of tangential thickness (even though very convenient for the algorithm) does not assure that a reasonable normal thickness is preserved, especially for highly staggered airfoils. The reduced peak Mach number resulted in an increase in computed total-to-total isentropic efficiency.

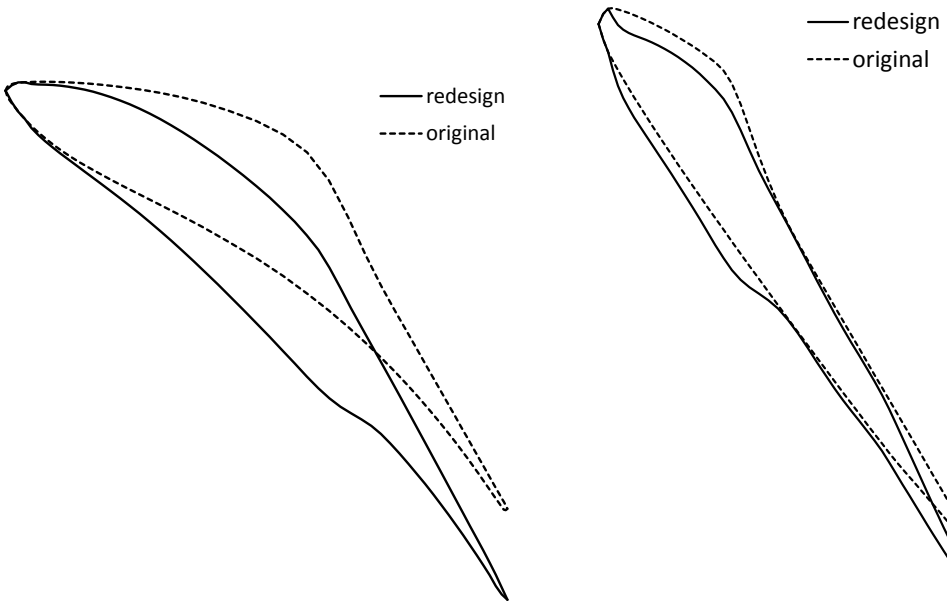

(a) 30% span (b) 50% span

Figure 5.12: Profiles resulting from redesign with prescribed loadings of figure 5.11

5.3.3.3 100% span

The original blade loading for the tip section is shown in figure 5.11f. A redesign aiming at making the blade section more aft-loaded was attempted (as seen in figure 5.11f); the corresponding $\tilde{V}_y$ was computed and set as a target. Figure 5.11e

shows that the $\tilde{V}_y$ curve seems to have moved close to the prescription, however its derivative shows some discrepancies with the prescribed load distribution. Probably the main element hindering the effectiveness of the method is the difficult treatment of the LE. In this case the first few points in the axial direction are kept constant. Because the axial and actual leading edges do not coincide (especially for highly staggered blades), there will be pressure side points on both the upper and lower blade profiles upstream of the actual LE (figure 5.13). The blade update algorithm does not work properly at these locations, hence all the shaded portion in figure 5.13 is kept fixed. This, however, might not result in a sound LE design, and could be the cause of poor convergence, especially for transonic airfoils where small variations in geometry result in large aerodynamic effects. The total-to-total isentropic efficiency of the new design dropped by one percentage point, probably as a result of the increased shock strength at the trailing edge.

5.4 Drawbacks of this approach

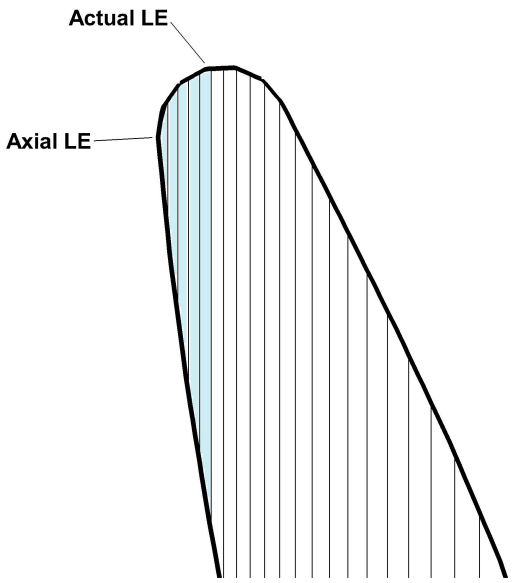

Figure 5.13: The LE in the tangential specification; the portion of pressure surface upstream of the actual LE is shown shaded

In the previous section it was shown how the tangential thickness based rep-

resentation of the blades and associated inverse design procedure display some shortcomings when applied to the long last stage rotor under consideration. The main areas of concern are the LE distortion caused by the inadequate representation of this portion of the blade at high stagger, together with the considerable changes in blade normal thickness which might yield infeasible blade profiles.
In an attempt to improve the situation, the strategy was modified by introducing a normal thickness evaluation on top of the existing methodology. This was aimed at preserving a constant normal thickness distribution during blade update, in order to achieve more realistic blades with the inverse design procedure. This fix, however, did not solve the fundamental problem of having an algorithm based on tangential thickness. The modified method starts from a tangential thickness representation of the blade; an iterative procedure then searches for the camber and the normal thickness relative to it, by interpolating from the existing blade points. This normal thickness distribution is then stored in a file. The same blade update algorithm of section 5.2 is then used at each iteration of the inverse design to modify the camber line. The major difference is that after the update, instead of imposing the original tangential thickness distribution, the blade profile is reconstructed by imposing the normal thickness distribution stored in the respective file. It is important to note at his stage that the existing inverse design methodology (5.2) was derived for tangential thickness specification, and it is based on the following fundamental assumptions:

- The tangential thickness representation is coupled with a sheared H-mesh (constant-x lines), where blade points and mesh vertexes coincide
- The upper and lower profiles of the 2-dimensional blade section, are specified at points with identical axial positions and are split at the axial LE and TE (minimum and maximum x respectively, see fig. 5.13). This allows them to be described by uni-valued functions of x

When reconstructing the blade using the normal thickness but keeping the tangential based inverse design method, several approximations are made:

- The camber is modified using current tangential thickness (see equation 5.4, at the beginning of the derivation), but then the normal thickness is

actually imposed when reconstructing the blade: this makes the method less robust, since the resulting blade differs from the one computed by the algorithm. Success of this approach is based on the assumption that this difference is small, which might not always be the case.

- After reconstructing the blade, upper and lower profiles of the blade section need to be interpolated back to the original x-coordinates of the H-mesh (with normal thickness imposition there is no control over the x-coordinates of the profiles). This interpolation adds imprecision to the procedure.

- At high stagger there is a portion of pressure surface (PS) located upstream of the LE (where $x < x_{le}$, for blades with LE to the left, see figure 5.13). This portion needs to be reconstructed after each blade update, within certain constraints:

  - the same axial LE position must be maintained
  - the new LE must be contained inside limits of the sheared H-mesh
  - the points describing the new LE must have same x-coordinates on either side of the axial LE

  A method was devised which kept the upstream portion of the PS fixed during camber update, and then interpolated back to the grid to ensure reasonable continuity with the new blade profile. The errors introduced in this approximative solution reduced robustness overall.

- This method is limited to coarser meshes (high shear does not allow refinement at LE). This greatly affects the capturing of supersonic effects (e.g. bow shocks)

- Supersonic aerofoils (such as the tip sections of the LP rotor) are sensitive to small changes in geometry, therefore all the above approximations are not well suited to the present case

Many attempts were made in trying to make this methodology work satisfactorily. It was eventually realised that a robust strategy could not be achieved since the underlying assumption in all the previous inverse design methods (e.g. Tiow and

Zangeneh [2000], Dang et al. [2000], Medd [2002]) was the tangential thickness specification; even though preserving normal thickness has been achieved before for other types of blades, the fundamental blade update algorithm still relied on the ability of specifying a tangential thickness and representing the upper and lower surfaces of the profile as functions of x. A new method is needed, where the blade is described through its normal thickness in a more systematic and robust way, and the blade update algorithm is actually derived based on this normal thickness specification.

Chapter 6

Blade representation based on normal thickness

6.1 Requirements of the new method

It was mentioned in the previous chapter that simply imposing a converted normal thickness in a tangential thickness based inverse method does not result in a robust approach when dealing with the type of LP turbine blades under consideration. It was decided for a completely new and perhaps more generic strategy, which would adapt well to the design of LP turbines, working equally well at hub and tip sections. The normal thickness (and resulting camber) description of the blade sections is more suitable for high stagger profiles and can possibly yield more realistic blades (under structural considerations). This is because the blade profile can be split into pressure and suction side at the actual LE and TE, rather than at the minimum and maximum axial locations. These features can be clearly observed in figure 6.1. The blade representation through tangential thickness (figure 6.1a) displays the drawbacks listed in section 5.4, namely the poor representation of the pressure surface axially upstream of the actual LE, and the potential shear introduced in the geometry when moving the camber points in an inverse design scenario.

The main advantage of the tangential thickness method, however, was the possibility of representing the upper and lower blade profiles in uni-valued functional

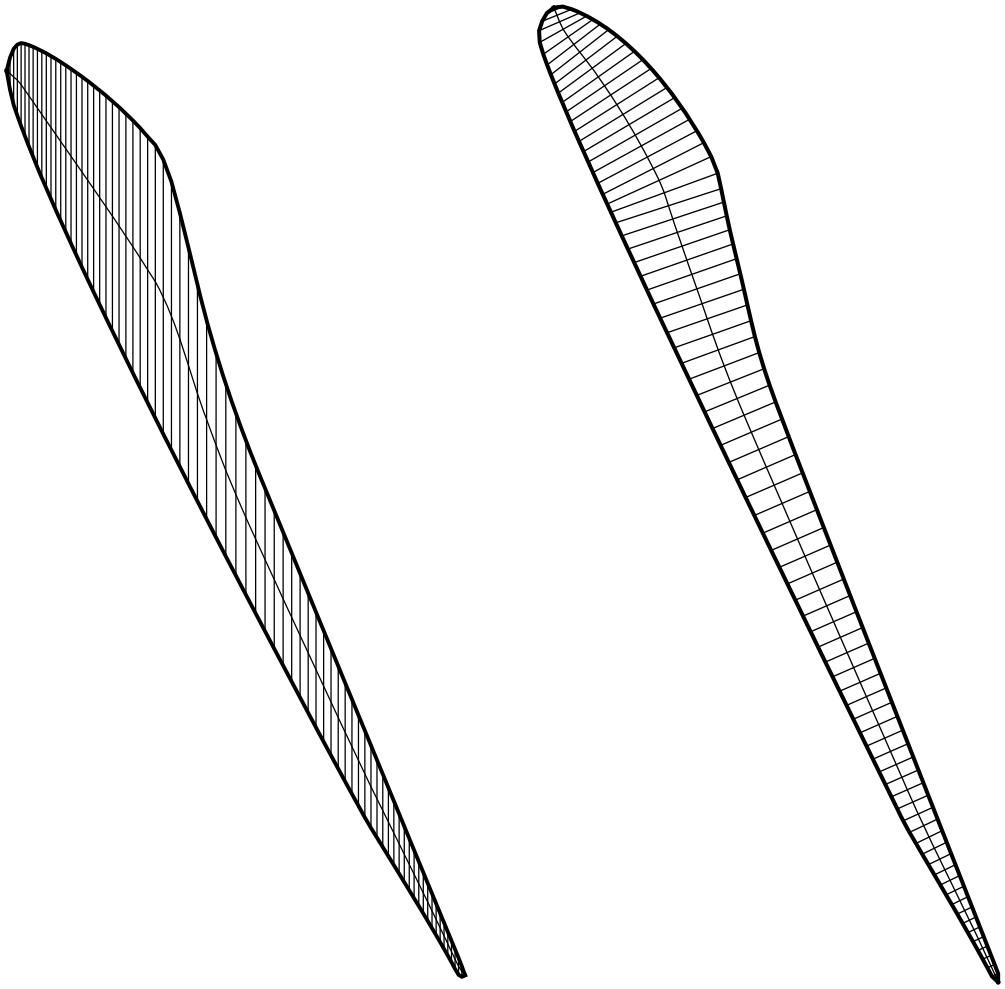

(a) Tangential thickness definition (b) Normal thickness definition

Figure 6.1: Representing a profile such as 50% span of a last stage rotor through different blade thickness definitions clearly shows the advantages of the normal method. Note also the differences in camber line.

form as the superposition of a camber line function $f(x)$ and a tangential thickness distribution t_θ:

$$f^{\pm} = f(x) \pm \frac{1}{2} t_\theta \tag{6.1}$$

which allowed the derivation of a neat blade update algorithm (see section 5.2). By looking at figure 6.1b it is obvious that a functional representation of the pressure and suction surface is not possible in the case of normal thickness representation. In other words, when splitting a high stagger blade profile at the actual LE, near LE the pressure side is not a uni-valued function of axial position x (at a given axial position in the proximity of the LE, can correspond two pressure surface points).

For a semi-inverse design in which the camber line is updated, a method is needed in order to represent the blades so that the pressure and suction surfaces can be reconstructed from a give camber line and specified thickness. In order to achieve this through a parametric representation of the profiles, the position of each camber line point will be represented in vector form $\mathbf{c}(s)$ as function of a single parameter s, and similarly for the upper and lower blade profiles $\mathbf{r}^{\pm}(s)$. Even if the use of parametric curves seems to initially add complexity to the procedure, it is a more powerful tool for geometric representation than simple uni-valued functions. A first advantage is, for example, the elimination of interpolation errors when moving blade points form one grid to another. But most importantly, it is very well suited to the blade description through normal thickness sought after in the present case thanks to the rapid evaluation of the tangent and normal vectors to the camber line curve $\mathbf{c}$ ($d\mathbf{c}/ds$ gives the unit tangent). To each camber point $\mathbf{c}$ corresponds a normal thickness vector $\mathbf{t}$. Adding or subtracting this vector from the camber position vector gives the upper or lower blade profile $\mathbf{r}$ respectively (figure 6.3):

$$\mathbf{r}^{\pm}(s) = \mathbf{c}(s) \pm \mathbf{t}(s) \tag{6.2}$$

where the parameter s is the camber arc length, the advantages of which will be discussed in section 6.3.2.1.

The method devised to represent the blades in parametric form through the use of non-uniform rational B-splines (NURBS) with arc length as parameter is detailed further in section (6.3).

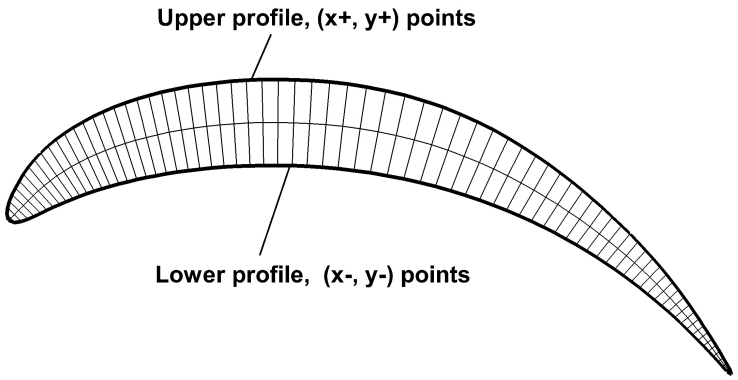

Figure 6.2: Blade section upper and lower profile definition

Here is a summary of the items required for a new inverse design method based on normal thickness specification:

1. A way of combining the camber+thickness requirement through parametric representation. This is resolved by describing the upper and lower blade profiles using the vector format $\mathbf{r}^{\pm}(s) = \mathbf{c}(s) \pm \mathbf{t}(s)$ as opposed to the previously employed functional format $f^{\pm} = f \pm t_{\theta}$.

2. A way of finding the normal camber, i.e. a new camber search algorithm. This is addressed in section 6.3.2.2.

3. A new type of mesh, which connects blade points across the passage without interpolation. Since points on the upper and lower profiles do not have matching x-coordinates, a more generic H-mesh is needed, which should still be single-block (for the inverse design). The mesh was generated using elliptic governing equations, with forcing terms for clustering and orthogonality to the walls (see section 7.1).

4. Re-meshing capability for the design procedure (see 7.1.4).

5. A **new blade update algorithm** which is one of the key elements in the new methodology. A method based on prescription of swirl velocity and normal thickness distribution was derived (see chapter 8).

6. An updated CFD solver. The solver employed in the tangential thickness based method had a simplified evaluation of fluxes at each computational cell, because of the constant-x vertical cell faces. This had to be modified for the elliptic mesh. Given that the way fluxes are computed had to be modified, the formulation was changed from a cell-centred to a node-centred (also known as vertex-centred or cell-vertex). This did not add any complexity, as the two formulations are almost equivalent in terms of coding and flow solution. The node-centred formulation was however preferred in this case as it simplifies some of the internal procedures of the new inverse design algorithm (presented in chapter 8). One of these is the evaluation of circumferentially averaged values on the arbitrary mesh using barycentric coordinates - as will be explained in chapter 8 - since no additional coordinates for the cell centres have to be stored. This was redesigned and re-coded, storing primitive variables at the cell verteces, modifying the flux computation at the computational cell, and adding compatibility with the arbitrary H-mesh (see section 7.2).

All the items above make it apparent that this new method required a radical restructuring of the inverse design procedure, and in particular a new blade update algorithm had to be derived from first principles. The following section introduces the new approach derived for the description of the blades.

6.2 Constructing the blade from the camber

The aim of the new blade design method is to be more general, i.e. work at the very different sections of hub and tip. A flexible representation of the blades is therefore needed, and as explained in the previous section, this takes the form: $\mathbf{r}^{\pm}(s) = \mathbf{c}(s) \pm \mathbf{t}(s)$. The camber line is parametrised in terms of arc length, which means that the coordinates of the discrete points representing the camber are stored at corresponding values of arc length s, starting from 0 at the LE.

First, from a given blade profile, the camber line described by a thickness perpendicular to it needs to be computed through an iterative procedure. Once this

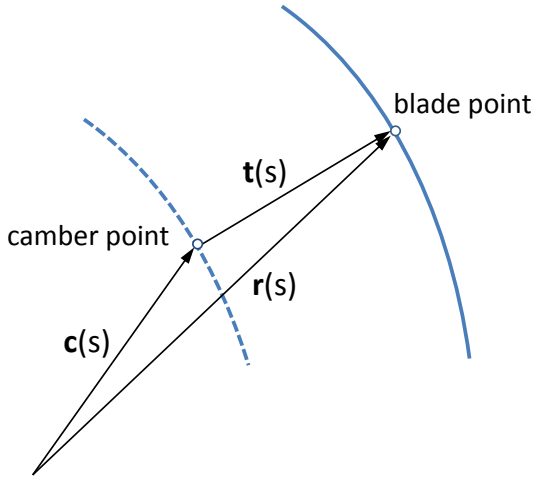

Figure 6.3: Camber plus normal thickness vector give the blade profile

is available from the search procedure described in section 6.6, its x, y coordinates are stored in a file. The value of half the normal thickness (i.e. the magnitude of $\mathbf{t}$) is stored in a separate file under the assumption that each value corresponds to a camber point. Note that at this point, the thickness magnitude is related to the camber only through indexing.

The camber line $\mathbf{c}(s)$ will be modified by the blade update algorithm, giving a new set of camber points. Thence, new values of s are computed and assigned to each point. The normal to the camber at each point is then given by:

$$\mathbf{N}_c = \frac{\mathbf{c}''(s)}{|\mathbf{c}''(s)|} \tag{6.3}$$

and if the Cartesian components of $\mathbf{c}$ are denoted by:

$$\mathbf{c}(s) = c_x\hat{\boldsymbol{\imath}} + c_y\hat{\boldsymbol{\jmath}}$$

then:

$$\mathbf{N}_c = \left[\left(\frac{d^2c_x}{ds^2}\right)^2 + \left(\frac{d^2c_y}{ds^2}\right)^2\right]^{-\frac{1}{2}} \left(\frac{d^2c_x}{ds^2}\hat{\boldsymbol{\imath}} + \frac{d^2c_y}{ds^2}\hat{\boldsymbol{\jmath}}\right) \tag{6.4}$$

gives the unit normal to the camber at each point. The derivatives are computed numerically for the discrete set of camber points.

The thickness vector is then related to the normal by:

$$\mathbf{t}(s) = |\mathbf{t}(s)|\,\mathbf{N}_c \tag{6.5}$$

where $|\mathbf{t}(s)|$ is the magnitude stored in the thickness file (which remains unchanged, only the normal direction changes with the camber line). The thickness vector can also be written in its Cartesian components:

$$\mathbf{t}(s) = t_x\hat{\boldsymbol{i}} + t_y\hat{\boldsymbol{j}}$$

The dependency of $\mathbf{t}$ on c_y is obvious by looking at equation (6.4); the next section will show that c_y is updated during the design procedure (c_x is fixed to preserve axial chord), hence all the vectors $\mathbf{t}$ are changing during design.

6.3 Obtaining the normal thickness and Camber

6.3.1 Parametric representation: NURBS

Parametric representation is useful in this case to deal with the complex geometries, and it is necessary because when splitting the high stagger blade section at the actual LE and TE, upper and lower profiles can not be represented as univalued functions of axial position. Furthermore it provides a convenient platform for describing the blades in terms of camber and normal thickness using vectors. Finally, the blade is represented with high accuracy without losses, even when changing grid size multiple times or during iterative procedures, since the spline is fitted to an unmodified set of control points (e.g. stored in a file).

The most versatile parametric form is generally the Non-Uniform Rational

B-Spline (NURBS) representation. The *p-th* degree NURBS is defined by:

$$C(u) = \frac{\sum_{i=0}^{n} N_{i,p}(u) w_i \mathbf{P}_i}{\sum_{i=0}^{n} N_{i,p}(u) w_i} \qquad a \leq u \leq b \tag{6.6}$$

Where $\mathbf{P}_i$ are the control points (each point is represented by a vector), w_i are the weights, and $N_{i,p}(u)$ are the *p-th* degree B-spline basis functions defined on the non-periodic and non-uniform knot vector:

$$U = \{\underbrace{a, \ldots, a}_{p+1}, u_{p+1}, \ldots, u_{m-p-1}, \underbrace{b, \ldots, b}_{p+1}\} \tag{6.7}$$

where a and b are usually 0 and 1 respectively. When all the weights are set to unity, (6.6) reduces to the special case of a *p-th* degree B-spline:

$$C(u) = \sum_{i=0}^{n} N_{i,p}(u) \mathbf{P}_i \tag{6.8}$$

since, by definition, the sum of all the basis functions of *p-th* degree is unity.
In general, the lower the degree, the closer the curve is to the control polygon, with the limiting case of 1^{st} degree, where the curve coincides with the control polygon (piecewise linear). This is because at lower degrees, fewer points influence the value $C(u_0)$ at a given u_0. An additional note is that the number of knots is $m + 1$, where $m = n + p + 1$, and $n + 1$ is the number of control points. An increase by 1 in degree allows for an extra knot. However, the multiplicity is also increased at the first and last knot, in order to keep the curve coincident with those points. At the limit $p = n$, all the control points influence the curve and gives the special case of a Bezier curve. The knot vector for the Bezier curve is:

$$U = \{1, \ldots, 1, 0, \ldots, 0\}$$

6.3.2 Normal camber search

The camber line connects the LE and TE points of a blade profile (these points are not the minimum and maximum axial positions as for the tangential thickness method). Furthermore through each *normal camber* point there is a segment connecting pressure and suction sides of the profile, which is also perpendicular to the camber line and bisected by it.
Defining the camber line in such a way offers a great advantage, because it provides a rule for reconstructing the blade from a camber line, which is modified during inverse design. Other methods could be used to describe a blade profile through its camber line, such as the medial axis transformation of a planar shape. The theory of the medial axis is presented by Lee [1982], but a recent application of this to the representation of axial turbomachinery blades is the one by Grossmann and Juttler [2012]. As clealry shown in their paper, the medial axis does not represent the *normal camber* line, because each point of this axis is not equidistant from the pressure and suction sides of the blade (considering the minimum distance from the axis to the blade profile). Furthermore, the segments that branch out of the medial axis to form the planar shape are not necessarily perpendicular to it. This means that a rule cannot be provided for the reconstruction of the blade after camber line modifications, nor the prescription of a fixed blade thickness.
Even though very convenient for blade reconstruction, finding the normal camber line in the first place is not that straightforward. Not much literature is available on this: Medd [2002] describes his definition of blade profiles through the normal camber and thickness, but nowhere in his thesis he explains how this was found in the first place. Some commercial inverse methods provide a tangential-to-normal thickness conversion, but this is approximate and still uses minimum and maximum axial location as LE and TE points.
A simple iterative method is presented here in order to compute the normal camber line and its associated thickness distribution for a generic turbine blade profile.

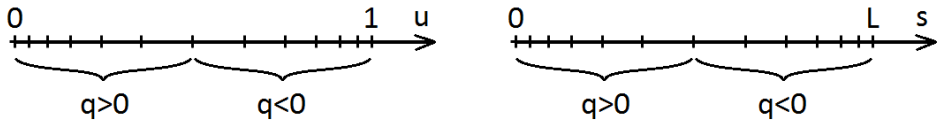

(a) using u intervals (b) using s intervals

Figure 6.4: Example of geometric progression applied to a segment

6.3.2.1 First guess

First, the blade section needs to be defined by an upper and lower profile, split at the actual LE and TE. In the present case, two arrays of points are created by converting from the starting format which gives the blade profiles as a set of x, y coordinates given in clockwise order, with special pointers to the LE and TE locations.

For each profile, a NURBS is fitted to the original points. This is done via two subroutines; the first initializes the knot vector (for the required curve degree) and reads in the control points (this is called once only). The second subroutine can be called multiple times with different input values of parameter u. The knot span, the basis functions and the $\mathbf{P} = (x, y)$ coordinate vector are computed within this subroutine (with calls to additional subroutines). The coordinates of the point are the output from the subroutine.

The user specifies the number n_{bl} of points needed for the rendering of the blade. Then $\mathbf{P_i} = (x_i, y_i)$ are computed at u_i for $i = 1, \ldots, n_{bl}$. For each profile, u goes form 0 to 1. The intervals between u_i values are chosen so that the points are more clustered near the LE and TE. For example, a geometric progression is employed for each half of the profile, where $\Delta u_{i+1} = \Delta u_i \cdot q$, and q is the geometric ratio (figure 6.4a). However, it was noted that because of the high curvature near the LE, the arc length segments covered by the first few strides of the parameter u were actually very short, resulting in excessive clustering of points in the LE region (this can be observed in figure 6.5a). It was therefore deemed more appropriate to re-parametrise the curve, so that the geometric progression would be applied to the arc length s ($s = 0$ at LE) instead of the parameter u (L is the total profile length) as in figure 6.4b This is achieved through an iterative procedure to find at each point the value of parameter u corresponding

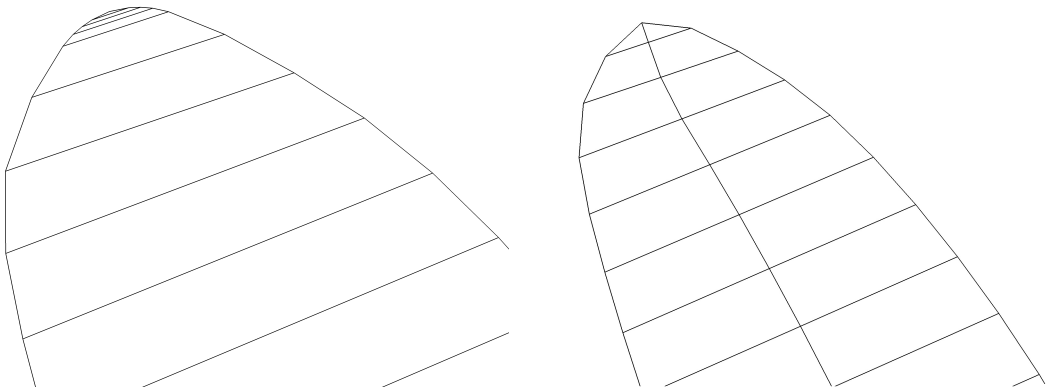

(a) The effect of curvature when imposing a geometric progression directly to the spline parameter

(b) Using s as parameter allows direct control over the spacing between points. The initial guess for camber points is shown.

Figure 6.5: Correcting the effect of curvature on parametrisation near LE

to the required value of arc length s (the bisection method was used for the search). The iterative routine is thus used to define upper and lower profiles at arc length intervals which correspond to equivalent percentages of total length of the respective profile. This is done by multiplying the original u distribution (which goes from 0 to 1), by the total arc length L of the profile. The two newly created sets of points serve in finding a first guess to the normal camber: each camber point will simply be the average between corresponding upper and lower profile points. The effect of re-parametrising in terms of s and the first guess for camber are shown in figure 6.5b.

6.3.2.2 Iterative search of camber

This algorithm is actually composed of a inner and an outer iterative procedure. The procedure starts from the first guess of camber points obtained in section 6.3.2.1. In the inner loop, for each camber point a search is performed to find the intersection between the profile and the normal to the camber line at that point. Once the intersections of upper and lower profiles with the normal is found, their average position will determine the updated location of the camber point: this is the outer loop.

The steps involved in the inner loop are as follows (refer to figure 6.6):

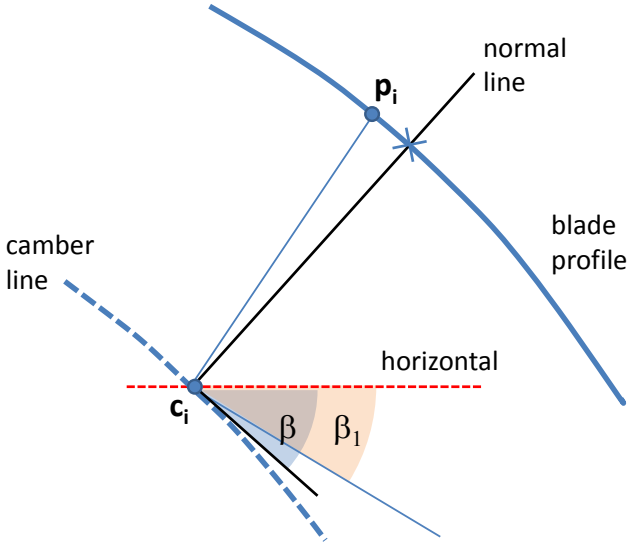

Figure 6.6: The inner loop in the camber search: finding the intersection of the local normal to the camber with the blade profile

1. Find the angle formed locally by the tangent to camber with the horizontal (β)

2. Find the angle formed by the line $\overline{\mathbf{c}_i\mathbf{p}_i}$ joining the current blade point $\mathbf{p}_i$ and the corresponding camber point $\mathbf{c}_i$ with the vertical direction (the equivalent angle β_1 in the figure, is shown as the angle between the line perpendicular to $\overline{\mathbf{c}_i\mathbf{p}_i}$ and the horizontal)

3. The point $\mathbf{p}_i$ is moved iteratively (by incrementally changing the parameter u and calling the NURBS subroutine which returns the coordinates of the point $\mathbf{p}_i$) until a satisfactory match is achieved between β and β_1

4. The same procedure is applied to upper and lower surface (changing the signs of the angles)

A new set of points is available for either upper and lower profiles of the blade section. The camber points are recalculated as the average between the newly updated profile points. The outer loop of the camber search repeats all the steps above, until modifications of the camber points become sufficiently small.

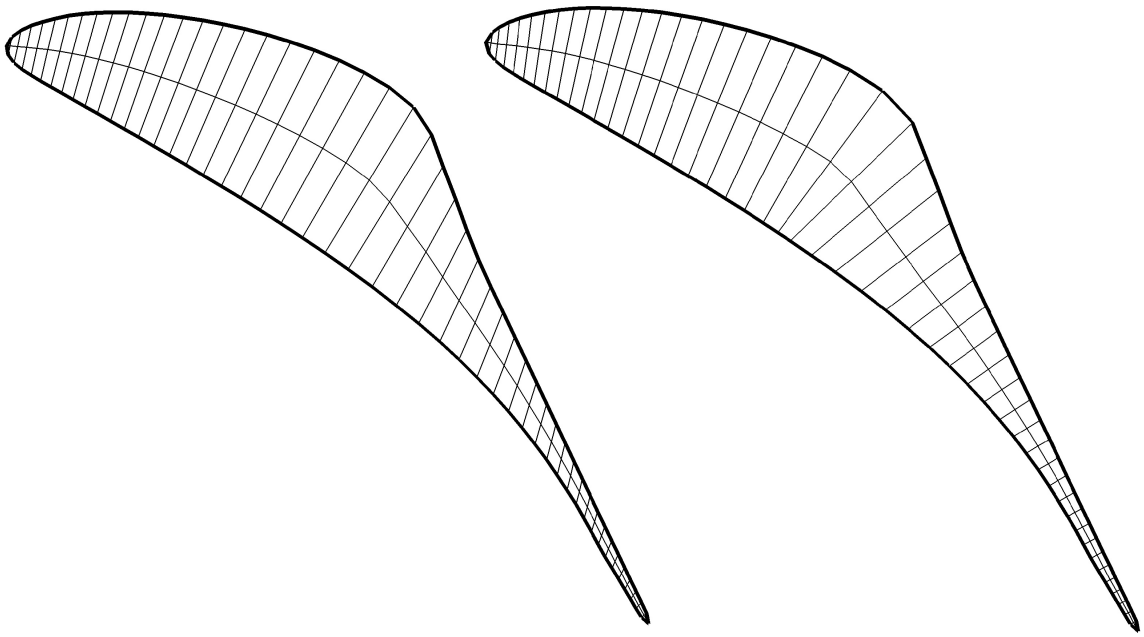

Figure 6.7: Example of first guess camber (left) and converged camber at 30% span of the long rotor blade

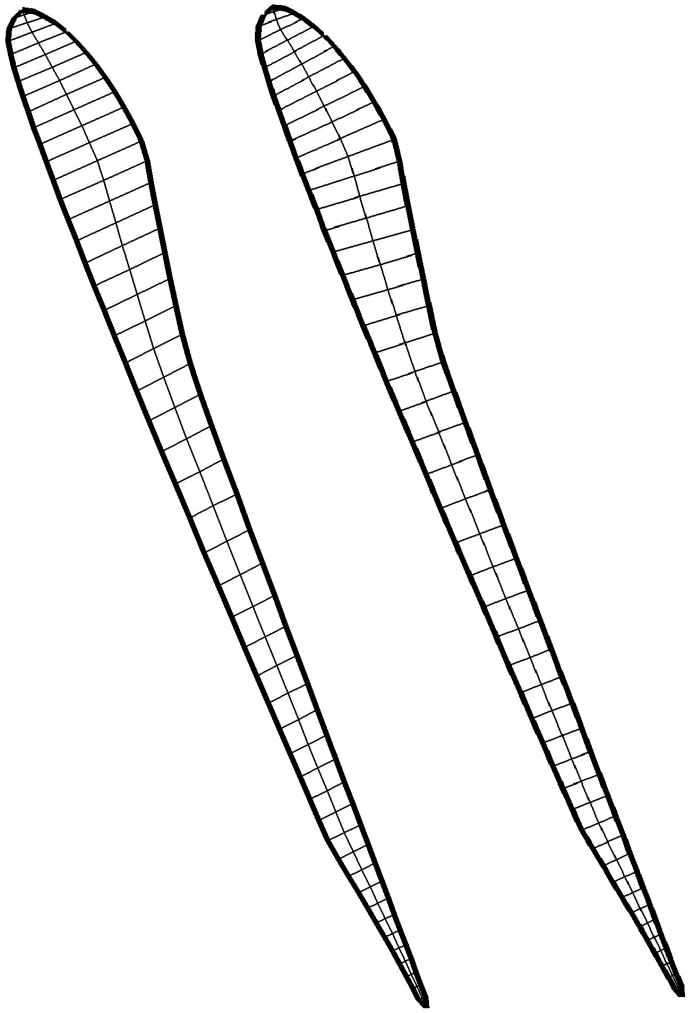

Figure 6.8: Example of first guess camber (left) and converged camber at 55% span of the long rotor blade

Chapter 7

Flow solver for new method

7.1 Mesh generation

7.1.1 The elliptic governing equations

With the normal camber line definition, blade profile points on pressure and suction side in the LE region cannot be connected with a straight line across the flow passage, especially at high stagger (this was possible when the profiles where defined with tangential thickness). Simple sheared H-mesh (with constant-x lines) cannot be employed in this case. Once the blade points are available from the camber search procedure, adding the inlet and outlet flow passages defines all the boundaries to the mesh. Elliptic governing equations for 1-to-1 mapping of non intersecting lines can be used to generate a smooth uniform H mesh.
The simple Laplace's equation provides a very robust method, but has the drawback of increased spacing between mesh points in the proximity of convex boundaries (such as the angle formed by the periodic boundary line with the LE wall). A method for clustering grid points near boundaries and imposing orthogonality to them was suggested by Steger and Sorenson [1979]. A system of Poisson's type equations governs the mapping:

$$\begin{aligned} \xi_{xx} + \xi_{yy} &= P(\xi, \eta) \\ \eta_{xx} + \eta_{yy} &= Q(\xi, \eta) \end{aligned} \tag{7.1}$$

where ξ and η are the transformed coordinates and P and Q are designed to give the required clustering effects. In the transformed space, the above equations become:

$$\begin{aligned} \alpha x_{\xi\xi} - 2\beta x_{\xi\eta} + \gamma x_{\eta\eta} &= -J^2(Px_\xi + Qx_\eta) \\ \alpha y_{\xi\xi} - 2\beta y_{\xi\eta} + \gamma y_{\eta\eta} &= -J^2(Py_\xi + Qy_\eta) \end{aligned} \tag{7.2}$$

where J is the Jacobian of the transformation:

$$J = x_\xi y_\eta - x_\eta y_\xi$$

and the coefficients:

$$\alpha = x_\eta^2 + y_\eta^2\,, \quad \beta = x_\xi x_\eta + y_\xi y_\eta\,, \quad \gamma = x_\xi^2 + y_\xi^2$$

In the paper of Steger and Sorenson [1979], P, and Q are given for clustering near a single boundary (e.g. in a O-grid). In the present case, clustering is needed at two boundaries (upper and lower blade surfaces). P and Q were then modified from the original form, to become:

$$\begin{aligned} P &= P_1 e^{-a(\eta-\eta_1)} + P_m e^{-c(\eta_m-\eta)} \\ Q &= Q_1 e^{-b(\eta-\eta_1)} + Q_m e^{-d(\eta_m-\eta)} \end{aligned} \tag{7.3}$$

where $P_1 = P(\xi, \eta_1)$, $Q_1 = Q(\xi, \eta_1)$, $P_M = P(\xi, \eta_m)$, $Q_M = Q(\xi, \eta_m)$ are calculated by imposing the two geometric requirements of element size near the wall and angle formed by lines incident to the boundaries. The same extension of P and Q to include two boundaries is used in Sorenson [1980]. Generally speaking $\eta_1 = 0$ and a, b, c, d are constants which determine how far the influence of the forcing terms can propagate within the domain; setting a, b, c, d very large will tend to a solution similar to Laplace's equation (i.e. no forcing terms). The equations in (7.2) are discretised and solved in the transformed space.

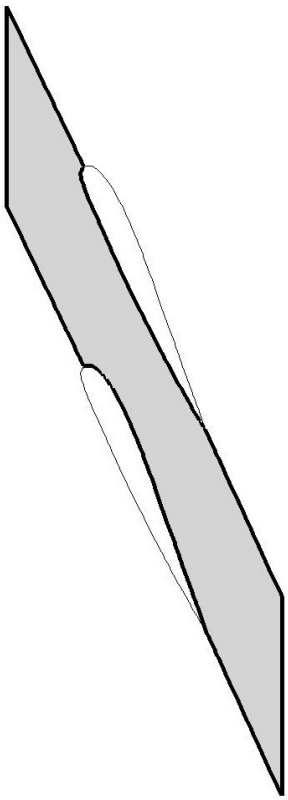

Figure 7.1: Boundaries of a computational domain, obtained by using upper and lower blade surfaces with extrapolated lines of periodic boundaries

7.1.2 Mesh boundaries and mesh

The Elliptic governing equations need all the boundaries to be defined. The blade points are available from the camber algorithm. The inlet and outlet periodic boundaries are extrapolated from the camber at 5% or 95% chord respectively. The upper and blade surfaces, togheter with the periodic boundaries enclose the entire computational domain for the flow solution, as shown in figure 7.1.

The length of the inlet and outlet passage periodic boundaries is user specified as a fraction of the axial chord. For example setting this fraction to 0.5 at inlet will result in an inlet periodic boundary which will extend axially upstream of the LE by a distance half the length of the blade axial chord. However, the long LP blades under consideration are characterized by high levels of twist. This means that near the hub, the blade sections will have long axial chord, and near the tip,

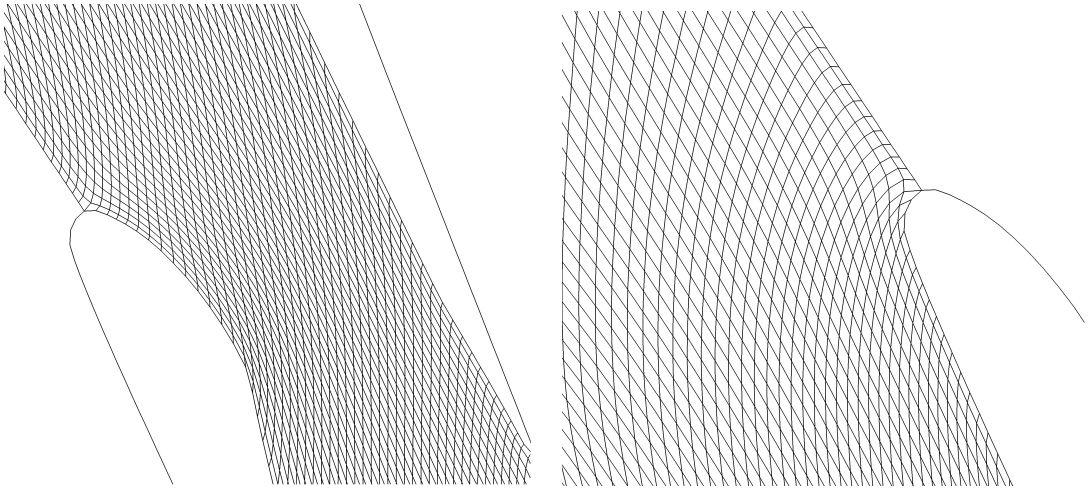

(a) flow passage (b) LE pressure side

Figure 7.2: Detail of mesh at 50% span

because of the high stagger angles, the axial chord will be very short. This will result in a very skewed computational domain at the high span sections, if the rule for determining the periodic boundary length is applied as just listed above. For this reason, instead of using the actual value of axial chord at each blade section, a "corrected" axial chord is used instead when estimating the required length of the inlet or outlet passages. The corrected axial chord increases the actual axial chord by a fraction corresponding to the sine of the stagger angle. For zero stagger, there will be no increment, as can be seen by the formula: $achord_c = 2 \cdot achord - \cos(S) \cdot achord$, where S is the stagger angle. Once again, this correction factor was devised in order to account for the necessity of longer (in the axial direction) inlet and outlet passages, as it returns larger fractions at high stagger sections (where the axial chord is very short). The ratios for the geometric progression used in clustering points near LE and TE is also user specified, along with the ratio for clustering in the y direction at the inflow and outflow. The number of mesh nodes m in the circumferential direction is calculated automatically to be proportional to the number of nodes n in the meridional direction as the pitch is proportional to the axial chord. Once all the boundaries of the mesh are defined, the interior nodes (or vertices) are computed from the elliptic solver, starting from an approximative first guess. A solution

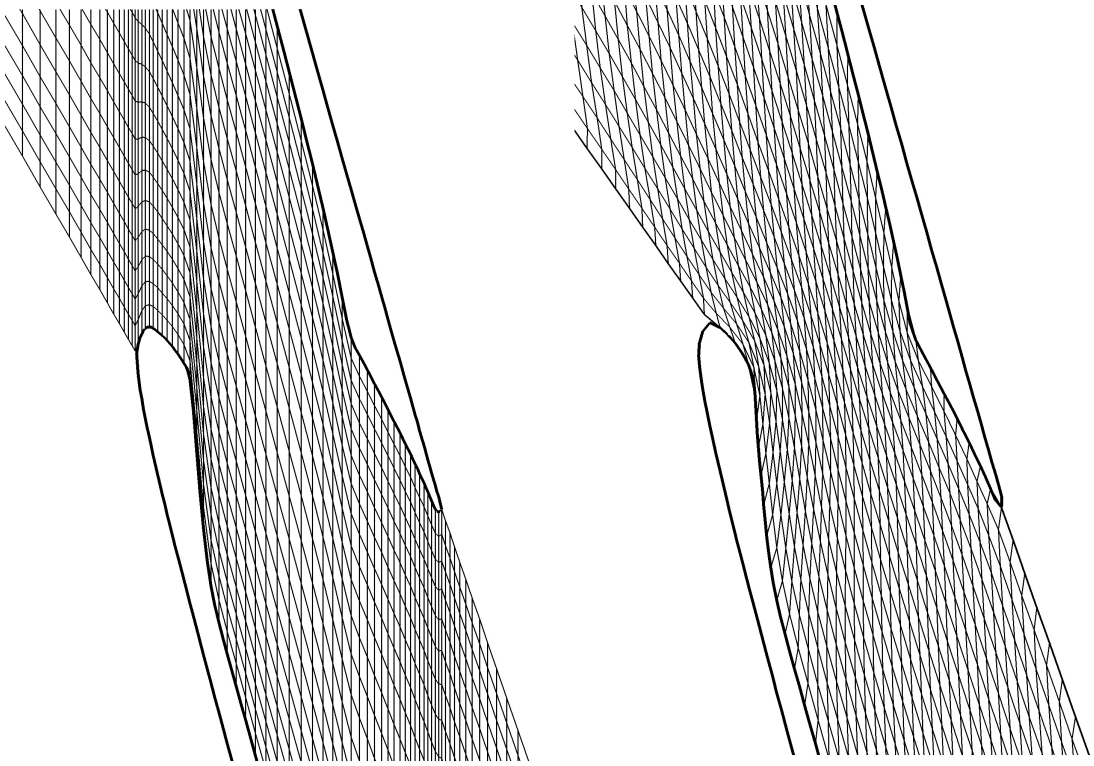

Figure 7.3: Comparison between blade thickness methods: H-sheared and elliptic meshes (only every other node is shown)

to the Poisson's equation (with forcing terms) is computed, which imposes the clustering near the walls and periodic boundaries, and perpendicularity of the j-directed lines to the walls (j being the mesh exex in the circumferential direction).

7.1.3 Notes on convergence of mesh generator

It was noted that creating a smooth mesh using governing equations of Laplace's form is in general a very robust and stable method, giving reasonable flexibility even at high stagger sections (where high shear is induced in the H-mesh). The main problem encountered in the mesh generation was the lack of convergence of the discretised Poisson's equation at high stagger angles. This is due to the fact that elliptic smoothing tries forcing all the mesh lines to intersect as orthogonally as possible: when the mesh boundaries impose very skewed angles at the cell vertices, convergence can be affected. While Laplace's equation seems to cope with this scenario, the addition of forcing terms to cluster cells at the boundaries and make the grid orthogonal to the blade walls seems to aggravate the situation. A possible solution to this problem could be running the mesh generator without forcing terms, and then use the solution as initial guess for a mesh based on the Poisson's equation. This however is impractical and results in higher computational times.

The forcing terms were thus modified in order to guarantee convergence also at high stagger angles and skewed meshes. By looking at the formulation of the forcing terms coefficients P and Q in equation 7.3 it is noted that when the constants a, b, c, d are set to large values, the forcing terms in 7.2 will tend to zero, reducing the governing equation to a Laplace's equation. Because the numerical solution of the Laplace equation proved to be the most stable, it follows that when the first guess for the grid is far from the final solution (e.g obtained from interpolation between boundaries), it is better to have the forcing terms close zero, but as the mesh converges to a final solution, these terms can be gradually introduced without the risk of causing instabilities. For the present case, a solution was devised by which an exponential decay is applied the values of a, b, c, d,

making them function of the cumulative time. Thus, for example, a becomes:

$$a(t) = a_0 e^{-kt/t_{max}} + a_1 \tag{7.4}$$

where a_0 is the initially large value used to reduce the forcing terms, and a_1 is the small value chosen for fully effective forcing terms. The coefficients k and t_{max} are chosen so that the exponential term will tend to zero within the typical number of timesteps t_{max} required for convergence of the mesh. For example, the mesh shown in figure 7.2 was obtained setting as convergence criterion a RMS residual of node position below 10^{-5} which was obtained within about 3000 time steps. The following values of constants were chosen: $a_0 = 800$, $a_1 = 0.9$, $t_{max} = 3000$ and $k = 10$.

Additionally, the numerical solution of the discretised equations governing the mesh can be under-relaxed. In Steger and Sorenson [1979] and in general mesh generation practice, over-relaxation is used to accelerate convergence; in the case of these highly skewed meshes it can become unstable, hence Gauss-Seidel (no relaxation) or under-relaxation is preferred.

7.1.4 Re-meshing during inverse design

Using an elliptic mesh requires the boundary points to be defined. In the blade update procedure used during inverse design, the axial position of LE and TE is preserved. After LE reconstruction, all the points for upper and lower blade profiles are available. The points at inlet and outlet periodic boundaries are extrapolated from the new chord, using old values of x-coordinates, obtaining the boundaries of the computational domain such as in figure 7.1. The inflow and outflow just need to be shifted in the tangential (y) direction (the pitch is preserved).

Once all the settings were in place for the first mesh, this method of re-meshing proved to be robust, an essential quality in the iterative procedure of the inverse design. For small modifications, the remeshing procedure is reasonably rapid, since the initial guess for the mesh is very close to the converged one.

7.2 Updated flow solver

7.2.1 Computation of fluxes

In a cell-vertex (or node-centred) formulation, the variables are stored at the mesh nodes (vertices). The main difference with the cell-centred formulation is in the locations where the primitive variables are stored and in the way the fluxes are summed around the computational cell (all-round fluxes). As already explained in section 6.1, the node-centred formulation was however preferred in this case as it simplifies some of the internal procedures of the new inverse design algorithm (presented in chapter 8). One of these is the evaluation of circumferentially averaged values on the arbitrary mesh using barycentric coordinates.
Considering the finite volume discretised system of Euler equations:

$$\frac{\partial}{\partial t}\mathbf{w}\cdot h + \underbrace{U\sum_{k=1}^{4}\mathbf{w_k}\Delta x_k}_{A} + \underbrace{\sum_{k=1}^{4}(\mathbf{f_k}\Delta y_k - \mathbf{g_k}\Delta x_k)}_{B} = 0 \tag{7.5}$$

Where $\mathbf{w}$ is the solution vector, and $\mathbf{f}$ and $\mathbf{g}$ are the flux vectors. The term A accounts for blade rotation (U is blade speed). The all-round flux for a cell is $F = A + B$, where the subscript k in (7.5) indicates values evaluated at the sides of a given computational cell. In the present formulation, fluxes are easily computed at the cell faces (sides), since the variables can be taken to be the average between two vertices. If the all-round flux is computed using 4 cell sides, this will be the all-round flux corresponding to the cell centre. Note that this is a virtual cell-centre, since its spatial coordinates are not needed.
In the present case the computational CV is chosen to be the quadrilateral formed by joining 4 adjacent cell centres: each cell vertex is therefore a centre of the computational CV (figure 7.4). The advantage of this is that the primitive values will be evaluated directly at the cell vertices. To find the all-round flux corresponding to the cell vertex, the average between the 4 surrounding cell centres is taken.

The all-round flux F for a computational cell corresponding to a vertex i, j is

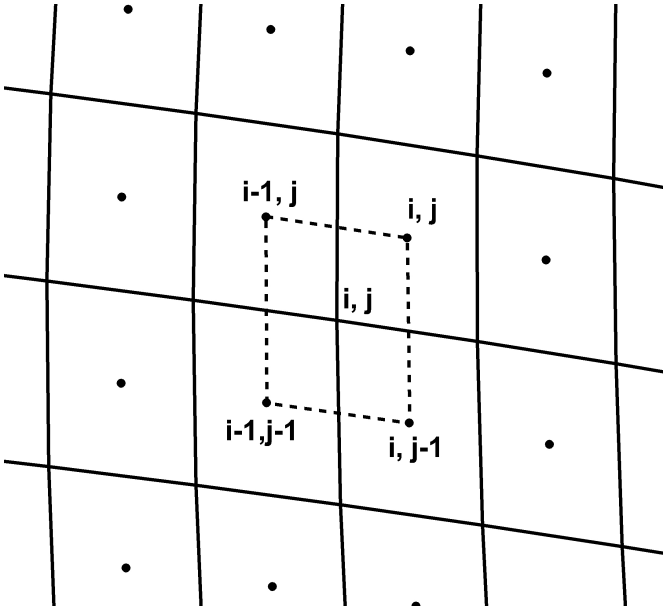

Figure 7.4: Computational control volume

then the average (refer to figure 7.4):

$$(F_{i,j})_{\text{vertex}} = \frac{1}{4}(F_{i,j} + F_{i,j-1} + F_{i-1,j} + F_{i-1,j-1}) \tag{7.6}$$

7.2.1.1 At the walls

The fluxes at cell sides on the wall boundaries are computed according to the type of condition being imposed: zero flux for solid walls, or no condition for transpiring walls. Either way, the all-round fluxes for vertices at a wall are computed in the same way: as the average between the 2 adjacent cells. This is equivalent to using 2 phantom cells mirroring the wall cells, and averaging over these 4 cells (figure 7.5):

$$(F_{i,j})_{\text{vertex}} = \frac{1}{4}(F_{i,1} + F_{i,0} + F_{i-1,1} + F_{i-1,0}) = \frac{1}{2}(F_{i,1} + F_{i,1,1}) \tag{7.7}$$

when $F_{i,0} = F_{i,1}$ (i.e. when mirroring cells).

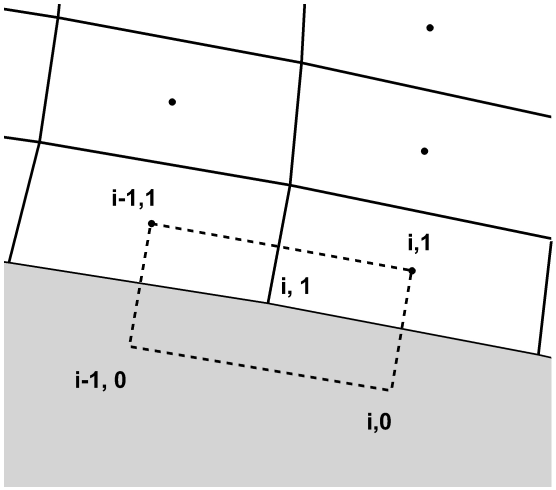

Figure 7.5: Computational control volume at the walls

7.2.1.2 At the periodic boundaries

At the periodic boundaries the cell vertex all-round flux is the average of the 4 adjacent cells. A special treatment of the indices is needed for this case in the algorithm. Periodic boundary condition is imposed outside the flux computation routine, by setting equal values at the periodic vertices.

7.2.2 Time step

Taking a local time step at each cell improves the convergence. However, the Courant-Friedrich-Lewy (CFL) condition must be satisfied for stability. In this case, the formulation for the time step to ensure stability is the one used by Van Den Burg et al. [1992]. For a 2D computational cell $i\,, j$, the time step is given by:

$$\Delta t_{i,j} = \frac{1}{1/\Delta t_i + 1/\Delta t_j} \tag{7.8}$$

The minimum time steps in the i and j directions are:

$$\Delta t_i = \frac{Ch_{i,j}}{\max\left(l_{i+\frac{1}{2},j}\lambda_{i+\frac{1}{2},j}, l_{i-\frac{1}{2},j}\lambda_{i-\frac{1}{2},j}\right)}$$

$$\Delta t_j = \frac{Ch_{i,j}}{\max\left(l_{i,j+\frac{1}{2}}\lambda_{i,j+\frac{1}{2}}, l_{i,j-\frac{1}{2}}\lambda_{i,j-\frac{1}{2}}\right)}$$

Where C is the Courant (or CFL) number, h is the cell area, l is the cell side length and λ is the maximum absolute eigenvalue of the flux Jacobian matrix:

$$\lambda = |V_n| + a \tag{7.9}$$

Where V_n is the velocity normal to the side l and a is the local speed of sound. The values of λ at the cell sides are computed using values of velocity and speed of sound taken as the average between adjacent cell vertices. The normal velocity V_n is given by the dot product between the velocity vector at the cell side and the normal direction to the cell side.

7.2.3 Flow solutions

7.2.3.1 Validation: VKI cascade

Kiok et al. [1986] gathered experimental results for cascade flow over a turbine blade section, at four different European wind tunnels. The cascade blades varied in size (scaled up or down) and number (from 8 to 12) in each one of the wind tunnels. Carefully calibrated probes upstream and downstream of the cascade measured total and static pressures, and flow angle. Tappings on two central blades provided surface pressure distributions. In their paper the authors provide the blade surface Mach number distributions for a subsonic and a transonic case.
The blade profile was represented through its normal thickness distribution and then meshed with the elliptic solver. The mesh of the flow passage had a node count of 8k, a coarse size typical of inverse design (rapidity of evaluation is more important than accuracy during the iterative design procedure). A simulation was then run with the updated flow solver.

The boundary conditions used in the numerical simulations were set to inlet total pressure of $1\,atm$, inlet total temperature $287\,K$, inflow angle 30^0; the outlet static pressure was set to $66.1\,kPa$ for the subsonic case, and $49\,kPa$ for the

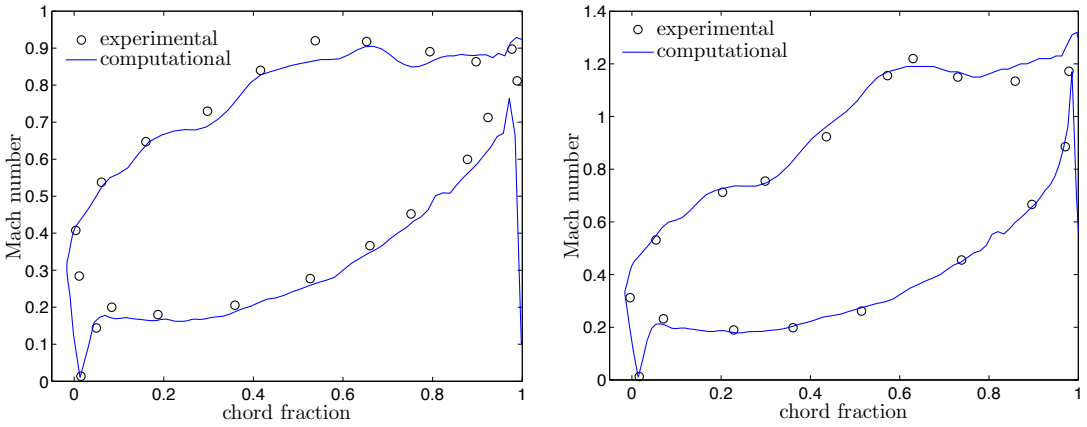

(a) subsonic case (b) transonic case

Figure 7.6: Surface Mach number comparison between VKI experiment and computation

transonic case.

The surface Mach number distributions are compared in figures 7.6a and 7.6b. The qualitative matching between computation ans experiment is satisfactory, considering that the solver is inviscid, two dimensional and a coarse mesh is employed.

7.2.3.2 Long rotor blade

The old solver, based on a sheared h-mesh, had some limitations, especially at very high stagger angles such as the tip section where, because of the high shear introduced in the mesh, some of the flow features could not be captured to a level considered satisfactory for inverse design. The updated solver based on the elliptic mesh shows some improvements in the quality of the flow solution. This is always within the limits of a relatively coarse mesh and an inviscid solver, which are what is being employed during the current inverse design procedure.

The most significant example of this is a comparison between the flow solutions obtained at the tip section with the old and new solver. At the tip, the flow is supersonic upstream of the LE. This results in the formation of bow shock, one side of which hits the pressure surface of the adjacent blade. The effect of this is

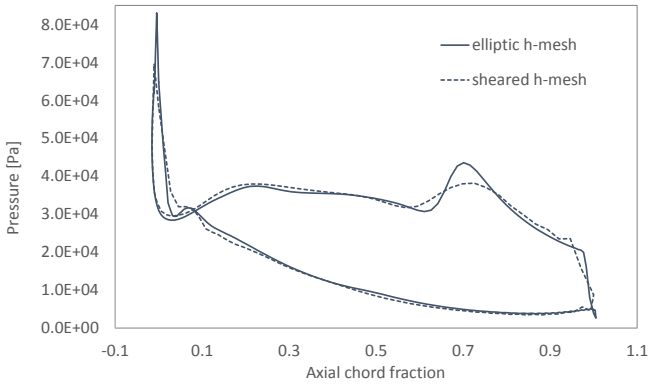

Figure 7.7: Blade pressure surface at tip, with clear pressure rise due to bow shock

clearly visible in the form of a surface pressure rise, by looking at figure 7.7. This pressure rise, which affects the blade loading considerably (hence the inverse design), was not captured as sharply with the previous mesh and solver. The improvement achieved is obvious in the comparison of figure 7.7. The pressure contours for the updated solution are shown in figure 7.8b. The shock locations are visible even if smeared, which is unavoidable with coarse meshes and with the level of shear which, even if greatly improved, is still present at the high stagger angle meshes.

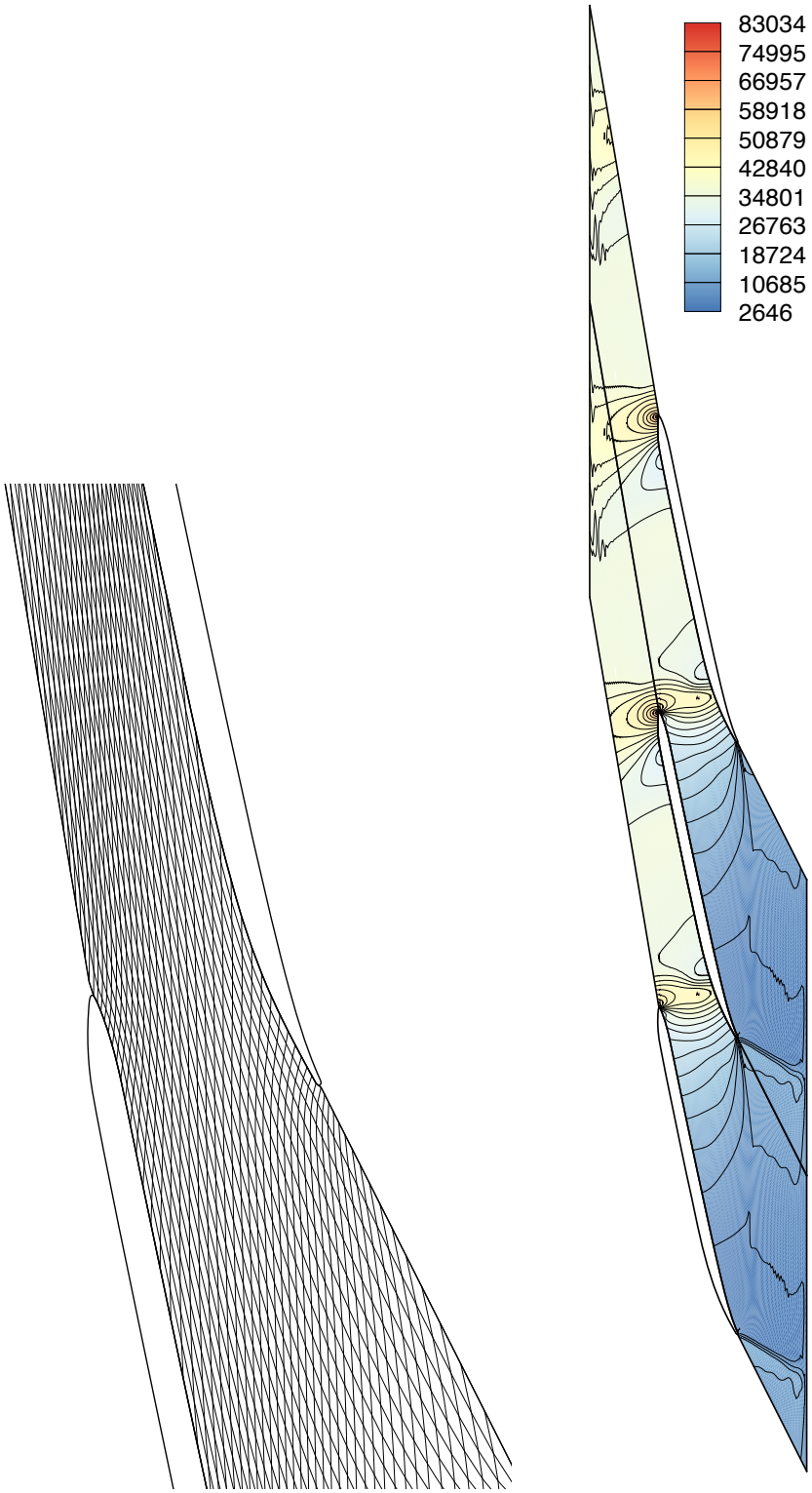

(a) mesh detail (only 1 in 3 nodes shown)

(b) pressure contours (2 domains shown)

Figure 7.8: Tip section results

Chapter 8

New Inverse method part 2: Swirl based

8.1 New swirl velocity method

As explained in section 2.3 and 6.1, a new blade update method based on normal thickness specification is needed.
The Δp method was initially chosen for the new normal thickness based blade configuration because of its convenient implementation with an arbitrary mesh, as it uses flow information only at the walls, avoiding the need for circumferential averaging of the flow variables across the blade-to-blade passage. However, it appears that this very aspect would make the method unsuitable for the transonic flows considered in this case, due to the reliance on extremely high accuracy of the flow solution at the walls, showing limitations when applied to thick and curved blades, as well as decambered and extremely high-stagger supersonic sections, choked flows and complex shock structures (the normal thickness Δp method developed is presented in appendix .4).
The swirl velocity algorithm presented in chapter 5, conversely, relies on the circumferentially averaged swirl for the computation of updated blade geometries. This means that information from across the whole flow passage is used, rather than just indirectly by using solely surface flow information.
This feature makes it far less dependant on the level of precision of surface velocity

vectors at the walls, possibly casting the foundation for a more robust method. The method had to be adapted to the new blade representation and mesh, with the two most notable tasks being the derivation of a new blade update algorithm, and the averaging of the swirl velocity on the new grid.

8.1.1 Blade update algorithm

The blade surface was described in section 6.2 in terms of upper and lower profiles ($\mathbf{r}^+$ and $\mathbf{r}^-$) as $\mathbf{r}^{\pm}(s) = \mathbf{c}(s) \pm \mathbf{t}(s)$, where the Cartesian components of the camber $\mathbf{c}$ are denoted by:

$$\mathbf{c}(s) = c_x \hat{\boldsymbol{\imath}} + c_y \hat{\boldsymbol{\jmath}}$$

The thickness vector can also be written in its Cartesian components:

$$\mathbf{t}(s) = t_x \hat{\boldsymbol{\imath}} + t_y \hat{\boldsymbol{\jmath}}$$

Defining the vector tangential to the blade surface at each point:

$$\mathbf{T} = T_x \hat{\boldsymbol{\imath}} + T_y \hat{\boldsymbol{\jmath}}$$

The tangent to $\mathbf{r}$ will be the derivative with respect to its arc length σ:

$$\mathbf{T}^{\pm} = \frac{d\mathbf{r}^{\pm}}{d\sigma^{\pm}}$$

Where σ is the blade surface arc length, computed in this case numerically from the available set of blade surface points. Then applying chain rule, the above can be expanded as:

$$\mathbf{T}^{\pm} = \frac{ds}{d\sigma^{\pm}} \left[\frac{d}{ds}(c_x \pm t_x)\hat{\boldsymbol{\imath}} + \frac{d}{ds}(c_y \pm t_y)\hat{\boldsymbol{\jmath}} \right] \tag{8.1}$$

The surface velocity, or relative velocity vector is defined as:

$$\mathbf{V}^{\pm} = u^{\pm}\hat{\boldsymbol{\imath}} + v^{\pm}\hat{\boldsymbol{\jmath}} \tag{8.2}$$

The derivation of the blade update formula starts as in the previous method

from a tangency condition at the blade walls. In this case, the cross product between surface relative velocity and wall tangent vector is used:

$$|\mathbf{V} \times \mathbf{T}| = 0 \tag{8.3}$$

Where

$$\mathbf{T} = T_x \hat{\boldsymbol{i}} + T_y \hat{\boldsymbol{j}}$$

And $\mathbf{V}$ in this case represents the velocity relative to the blade, where u and v are its Cartesian components. Then (8.3) can be expanded and rearranged:

$$\frac{T_y}{T_x} u = v \tag{8.4}$$

A correction term is introduced on the right hand side, which will vanish as the blade converges to give the prescribed mass averaged swirl $\tilde{v}^*$ (in 2D the v component represents the tangential or swirl velocity):

$$\frac{T_y}{T_x} u = v + \tilde{v}^* - \tilde{v} \tag{8.5}$$

The tilde indicates circumferentially mass-averaged values and the star designates a prescribed quantity. Equation (8.5) will be rearranged into a formula to update camber line. This needs to be compact and computationally efficient, by avoiding implicitly repeated terms and minimizing the number of operations required. Defining the correction term $\Delta\tilde{v} = \tilde{v}^* - \tilde{v}$ then (8.5) can be written, for upper and lower blade surfaces:

$$T_y^{\pm} = \frac{T_x^{\pm}}{u^{\pm}} (v + \Delta\tilde{v})^{\pm} \tag{8.6}$$

The left hand side represents the updated value of T_y, thus the update formula starts taking shape. More explicitly, using the fact that $T_y = T_x \frac{v}{u}$ (from the tangency condition) (8.6) is expanded to:

$$T_y^{\pm} = T_y^{\pm} + \left(\frac{T_x}{u} \Delta\tilde{v} \right)^{\pm} \tag{8.7}$$

Where all the terms on the RHS come from the latest solution, and the LHS

is the new value for the following iteration.

Now, from (31):

$$T_y^{\pm} = \frac{ds}{d\sigma^{\pm}} \frac{d}{ds}(c_y \pm t_y) \tag{8.8}$$

Thus:

$$\underbrace{\frac{d}{ds}(c_y \pm t_y)}_{t+\Delta t} = \underbrace{\frac{d}{ds}(c_y \pm t_y)}_{t} + \frac{1}{\frac{ds}{d\sigma^{\pm}}} \left(\frac{T_x}{u} \Delta\tilde{v} \right)^{\pm} \tag{8.9}$$

Adding upper and lower surface equations in (8.9) yields:

$$\frac{d}{ds}(c_y)^{t+\Delta t} = \frac{d}{ds}(c_y)^t + \frac{0.5}{\frac{ds}{d\sigma^+}} \left(\frac{T_x}{u} \Delta\tilde{v} \right)^+ + \frac{0.5}{\frac{ds}{d\sigma^-}} \left(\frac{T_x}{u} \Delta\tilde{v} \right)^- \tag{8.10}$$

Which can be integrated numerically along the camber line to give an updated set of camber line y-coordinates $c_y^{t+\Delta t}$. It is reminded here that the curve parameter s represents the camber arc length, while σ represent the blade surface arc length. Only the y-coordinate c_y is modified, keeping c_x constant in order to preserve axial chord. The integration of (8.10) is performed starting from a fixed stacking point, which provides the constant of integration.

8.1.2 Correction to blade update formula using only suction side

By looking at equation (8.10) it can be observed that the new position of each camber point is influenced by a term dependent on the flow on the pressure side and by one on the suction side of the blade. At each camber point there is a specified thickness, which defines two points on the blade, one on the upper side (in this case the suction side) denoted by a plus, and one on the lower side (the pressure side) denoted in this case by a minus. The tangency condition at each blade point and the departure of the flow from the prescription will determine how much the camber point linked to that specific blade point has to move. As explained earlier, this movement is constrained in the axial direction, so that the total axial chord length is preserved (thus each camber point can only move in

the tangential - or y - direction). This was the case also in the previous method based on tangential thickness as shown in equation (5.15).
In both cases, using information from the two sides of the blade to update the camber point is actually redundant. This is because the prescribed swirl distribution is averaged across the passage, which means that at a given axial position the same value of $\tilde{v}$ is being imposed on either side of the blade profile. Not only this is redundant per se (by imposing the same distribution simultaneously from either side), but even more so given that each point on the blade suction side is geometrically constrained to its corresponding point on the pressure side through the specified thickness (normal or tangential). Furthermore, since the tangent vectors to the blade on upper and lower sides of the blade at a given axial location are different, the plus and minus terms in the update formula will give different direction (or just different magnitude) of movement to the same camber point. While this has a minor effect in the tangential thickness method (because blade points and corresponding camber point are all at the same axial location), having a blade update formula like (8.10) can actually create serious problems during the blade update, especially for thick blades or at high stagger angles.
The reason behind this lies in the specification of a normal thickness: in (8.10), each camber point is influenced by two blade points which lie at different axial positions (different x coordinates). Because of this, the values of computed and prescribed swirl at the two different locations can result in contrasting information, which might not be resolved in an effective movement of the camber point. Figure 8.1 helps understanding this, by showing a bad case scenario of this effect. In the figure, a blade profile is shown, and the the camber point under consideration with the corresponding blade points are highlighted with a dot. The prescribed (dashed) and computed (solid) swirl velocity distributions (this is an example, not the actual values) are also shown superimposed on the blade. It can be seen that at the suction side point the difference between prescribed and computed swirl is negative, which would result in a downward shift of the camber point. Conversely on the pressure side the positive difference in swirl should result in an upward shift of the same camber point. The contrasting information can result in the lack of convergence of the blade update procedure.

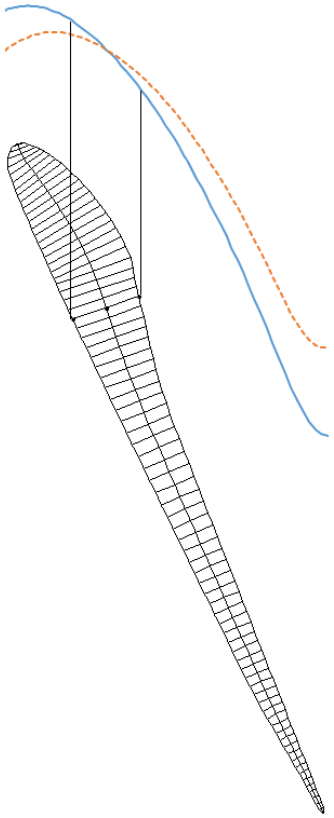

Figure 8.1: Example of prescribed swirl velocity distribution and a computed one. Having different axial locations influencing the same camber point can lead to errors

It was therefore decided to modify the blade update equation (8.10) so that only information from the suction side of the blade was used to modify the camber points. This is because the suction side of the blade profile has the greatest influence on the flow of turbomachines, and it is usually the main area of concern also in traditional design methods. The formula then becomes:

$$\frac{d}{ds}(c_y)^{t+\Delta t} = \frac{d}{ds}(c_y)^{t} + \frac{1}{\frac{ds}{d\sigma^+}}\left(\frac{T_x}{u}\Delta\tilde{v}\right)^+ \tag{8.11}$$

This is integrated along in the meridional direction to obtain the new camber line. The pressure side profile will result after each camber modification by the imposition of the normal thickness. Note that removing the influence of the pressure side flow does not change the fact that the geometric relationship between

pressure and suction sides is still fixed by the normal thickness distribution. This means that the method does not lose the ability to iteratively converge to the prescribed swirl distribution but it actually becomes more robust, as explained above.

8.1.3 Averaging the swirl on the generic H-mesh

The swirl method requires the prescription of a swirl velocity distribution along the axial distance. As already pointed out earlier, In 2D the swirl velocity corresponds to the y component of velocity, when the rotation axis is parallel to the x axis.
At each one of the discrete points on the blade surface, a value of circumferentially averaged swirl $\tilde{v}$ is needed in order to evaluate the latest value of $\Delta\tilde{v}$ in equation 8.10, at every iteration of the blade update procedure.
Note that a $\tilde{v}$ distribution is needed for the suction surface points only, to be employed in the corrected blade update algorithm presented in the previous section. However, this is found in the present case by taking the average of both distributions obtained from the upper and lower surface sets of points. The reason behind this is twofold: increasing the accuracy by refining the mesh on which the distribution is computed, and also exploiting the fact that on the pressure side the x coordinates of the blade points extend further upstream with respect to the suction side (for a given camber point), providing more information in the crucial LE area.
The circumferential averaging at each axial location is performed along lines of constant x, so that every point on the upper or lower surface will have an associated value of $\tilde{v}$ as they all have different x coordinate.
In order to perform the averaging, v needs to be thus interpolated from the flow solver grid to a new grid with lines of constant x. This is done by constructing two sheared H-mesh grids (with constant x lines), one for the upper and one for the lower surface:

1. At each location on the blade surface, the point on the opposite surface with the same x coordinate is found through interpolation (as in figure

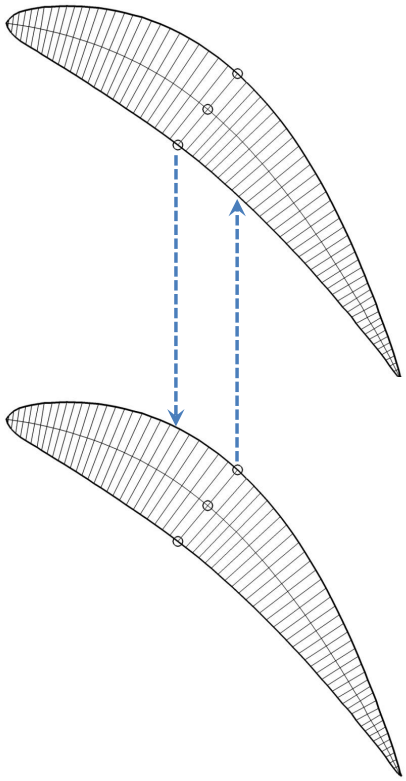

Figure 8.2: Lines for circumferential averaging for each point on pressure and suction surface

8.2), then the line joining the two points is divided in $m-1$ equispaced intervals. Therefore, two grids of $n_{bl} \times m$ nodes are created, n_{bl} being the number of camber points from LE to TE.

2. For each point of the newly fitted mesh, the 3 closest surrounding vertices of the solver mesh need to be found. This is done by performing a search for the 3 shortest distances, and then testing if the point is actually lying within the triangle formed by the 3 points so obtained (the barycentric coordinates of the point with respect to the triangle vertices must be positive).

3. The variables needed for the mass averaging (u, v, ρ) are interpolated at each point from the three surrounding vertices using barycentric coordinates.

4. The mass averaging is performed along the constant-x lines of the fitted

mesh, to give values of $\tilde{v}^{\pm}$, where the "+" superscript is associated with points on the upper profile and the "−" superscript with lower profile.

5. Note in figure 8.2 that values of $\tilde{v}^{\pm}$ corresponding to a camber point are given at different x positions but are actually represented by the same function of x. This means that plotting the distributions obtained from the pressure and suction side points should result in overlapping curves. A single distribution is obtained by averaging these two and an optional smoothing of the curve can also be performed to damp any numerical inaccuracies.

A final consideration is that $\tilde{v}$ cannot be evaluated for the portion of pressure surface upstream of LE for high stagger blades. It is common practice to reconstruct LE regions after the rest of the camber has been modified through the blade update procedure. A method is suggested in the following section.

8.1.4 LE reconstruction

In the previous method, the LE region was obtained by linearly extrapolating the camber line and imposing the normal thickness. This, however, can cause distortion. Steep gradients can cause elongation of the LE portion and in some high stagger cases, the rotation of the normal thickness vectors close to the LE will cause noticeable changes in the x location of the axial LE, altering the axial chord length.
A simple alternative to the extrapolation is the rotation of the LE camber line. This means that the points describing the LE camber are rotated about a temporarily fixed point (which may or may not be the stacking point), and then the normal thickness is imposed.
Since the LE regions to be reconstructed are often very close in shape to a circular arc, this approach has the advantage of preserving axial chord more accurately than the extrapolation method.

The rotation is performed about a "cut-off" point $\mathbf{P_{co}}(x_{co}, y_{co})$, by an angle $\theta = \alpha' - \alpha$ (figure 8.3), Where α' is the updated camber line angle at LE, and α is the old one. The result is an updated set of x', y' coordinates for the x, y

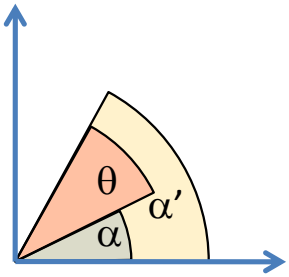

Figure 8.3: Difference between updated and old LE camber angles

points upstream of the cut-off point. The transformation is given by:

$$\begin{pmatrix} x' - x_{co} \\ y' - y_{co} \end{pmatrix} = \begin{pmatrix} cos\theta & -sin\theta \\ sin\theta & cos\theta \end{pmatrix} \begin{pmatrix} x - x_{co} \\ y - y_{co} \end{pmatrix} \tag{8.12}$$

The coordinates are computed as a distance from the cut-off point, which can move during the inverse design if it does not coincide with the stacking point. An example of reconstructed LE after camber modification is shown in figure 8.4. In this case "cut-off" and stacking point coincide.

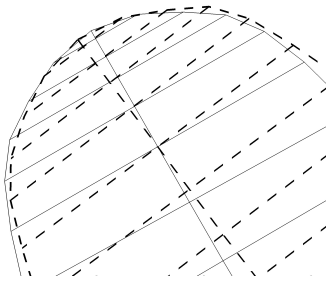

Figure 8.4: Example of rotated reconstructed LE (new and old shown)

8.1.5 Blade recovery

As previously done (e.g. chapter 5), the first test for a inverse method is the blade recovery, i.e. obtaining a known blade profile by prescribing its loading, starting from a modified profile. This was performed for different sections of the long last stage rotor. The first step consists of running a flow analysis for each blade

profile. Very good convergence is required for this numerical solution (RMS density residuals below 10^{-7}), so that the computed swirl velocity distribution can accurately represent the blade profile during the inverse design recovery. Then from each original profile, a modified profile is obtained by linearly shifting (by an arbitrary amount) the camber line about a stacking point and then imposing the same normal thickness. Then, starting from the modified profile, the inverse design procedure is run prescribing the originally computed swirl velocity distribution. The aim of this is to obtain the original profile, in order to demonstrate the effectiveness of the procedure.
Each blade update is executed iteratively after the flow solution has converged to a RMS density residual below 10^{-5}. The inverse design procedure updates the camber at each iteration, until the maximum y-coordinate modification of any camber line point falls below 0.1% of axial chord. This is typically achieved in 12-20 iterations. The flow solution of the final iteration is run to a convergence of RMS density residuals below 10^{-7}.
Some images are included here, where modified, original and recovered profile are shown. The recovery test was very satisfactory, as the blade profiles obtained through the inverse procedure match the original with excellent agreement, with a maximum discrepancy between original and recovered profile at the tip section of 0.081 % of axial chord.

8.1.6 Redesign of generic LP turbine

While the profile redesign of the long blade of the last stage rotor considered in this research project will be the topic of the next chapter (with stacking of profiles to form a 3D blade), some sample redesigns of a generic LP turbine tip section under choked flow conditions are shown here, as a test for the inverse design procedure just developed. The blade geometry is the same as the one employed in section 5.3.2.1, but the working fluid in this case is air ideal gas. The inlet stagnation pressure is $140kPa$ and the design exit pressure is $101kPa$: changing this exit value within plus or minus $20kPa$ results in different mass flows and blade loadings. Reducing the exit pressure enough gives choked flow, with recovery shock appearing on the suction side and moving downstream as the

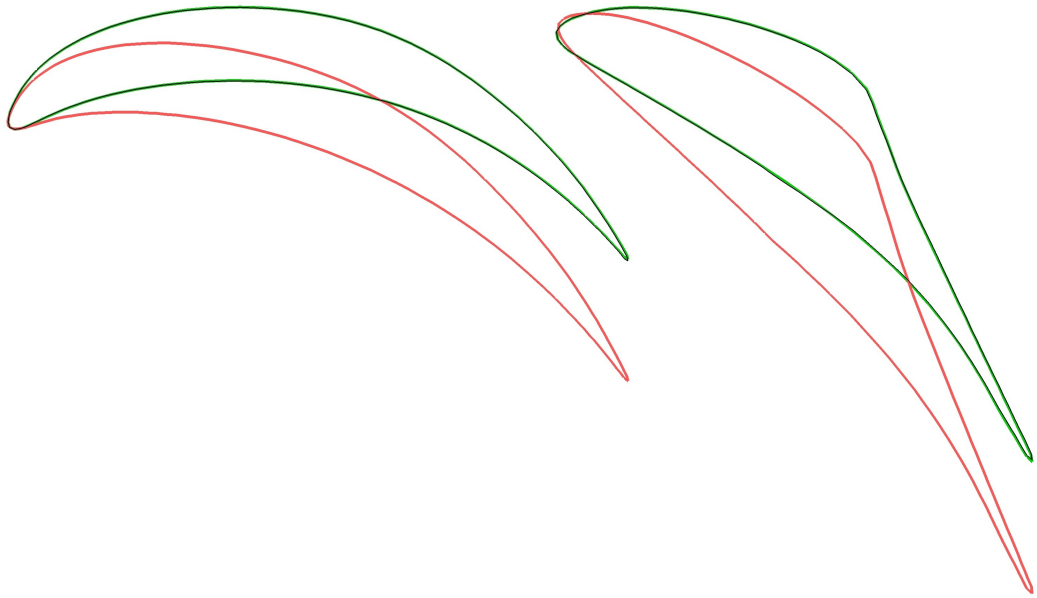

Figure 8.5: Hub (left) and 30% span section recovery (not to same scale). Original (green), modified (red) and recovered (black) profiles. The black overlaps the green perfectly, meaning that the blade recovery was excellent.

back pressure reduces (figure 8.7). At $40kPa$ the flow can effectively be considered fully choked, and further reductions will not affect the blade loading. With this boundary condition, a few test redesigns were carried out, with prescribed and obtained swirl distributions and loadings shown in figure 8.8. The reason for choosing a fully choked flow is to test the behaviour of the inverse design procedure in such a flow regime, which will characterize the last stage rotor redesigned in the next chapter (this runs at a fully choked regime).
In all cases the the blade updates were carried out at each iteration after the flow solution reached RMS density residuals smaller than 10^{-5}. The exit criterion for the inverse design was set to camber point modifications smaller than 0.5% of axial chord. The inverse design procedure proved robust and good matching between prescription and redesign can be observed. The main discrepancy is shown near LE. This is attributed to the fact that the blade geometry near the LE is not modified by the procedure but only rotated to align it with the updated camber line. Additionally there are changes in axial flow due to modifications in throat

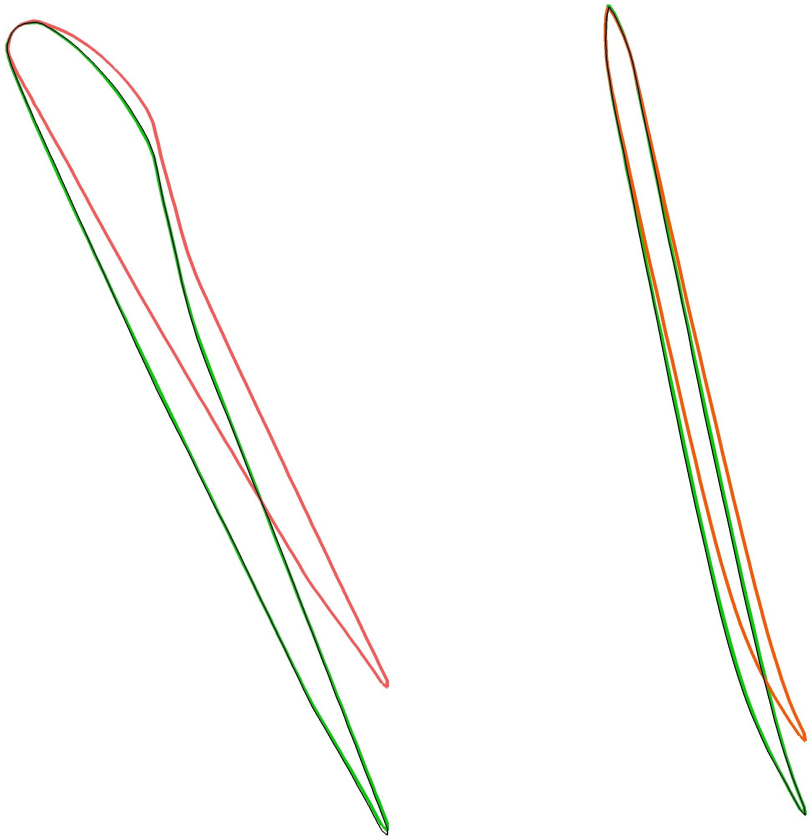

Figure 8.6: 50% span (left) and tip section recovery (not to the same scale). Original (green), modified (red) and recovered (black) profiles. The black overlaps the green perfectly, meaning that the blade recovery was excellent.

area which, at choked flow, are likely to affect incidence angles. The code was modified in order to keep constant relative inflow angles by adjusting the angle boundary conditions at the end of each design iteration. The improvements in obtained swirl distribution matching the prescription are seen by comparing figures 8.8a and 8.8g.

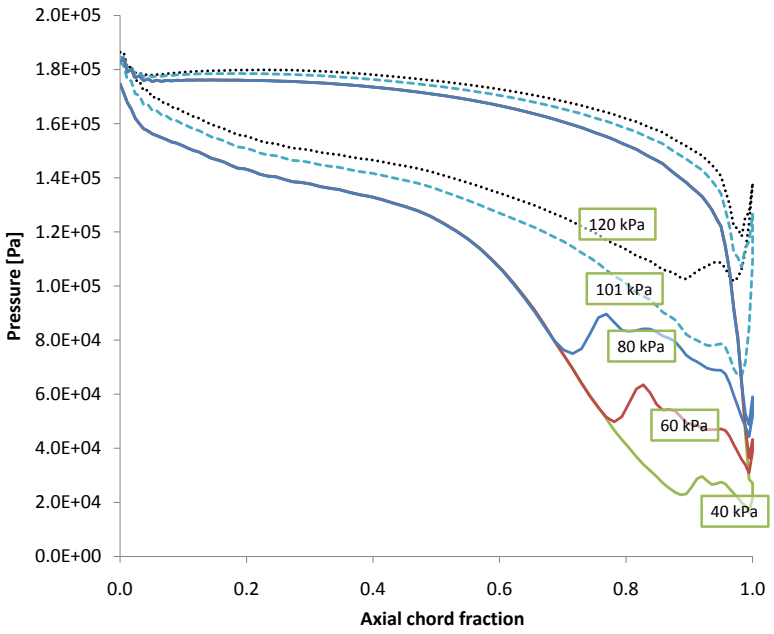

Figure 8.7: Blade surface pressure of tip section of air LP turbine, at different back pressure values (choked and un-choked) and inlet total pressure $140kPa$

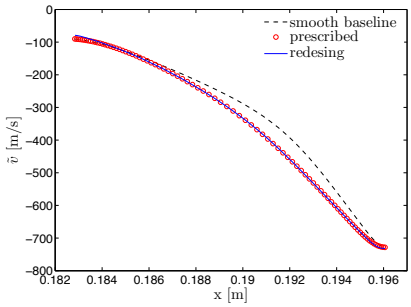

(a) swirl $\tilde{v}$ distributions for test 1

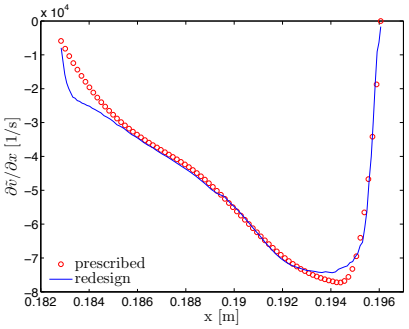

(b) loading $\partial\tilde{v}/\partial x$ for test 1

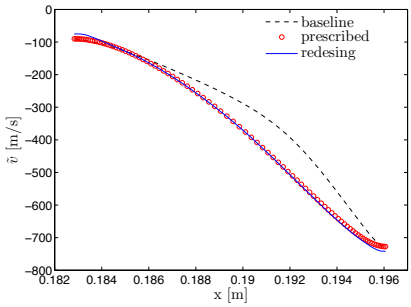

(c) swirl $\tilde{v}$ distributions for test 2

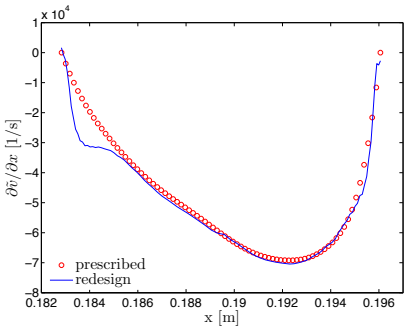

(d) loading $\partial\tilde{v}/\partial x$ for test 2

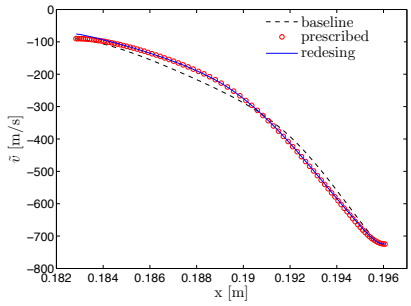

(e) swirl $\tilde{v}$ distributions for test 3

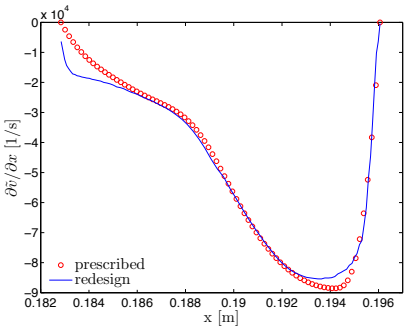

(f) loading $\partial\tilde{v}/\partial x$ for test 3

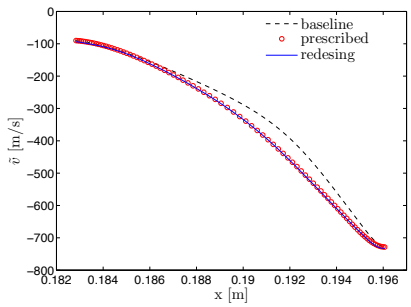

(g) swirl $\tilde{v}$ distributions for test 1 with adjusted inflow

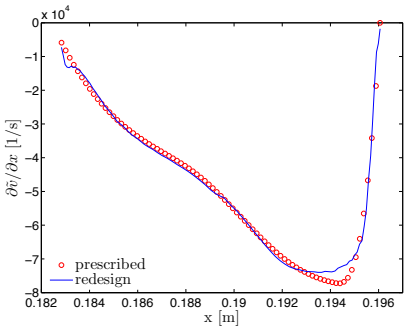

(h) loading $\partial\tilde{v}/\partial x$ for test 1 with adjusted inflow

Figure 8.8: Plots of inverse design tests for LP air turbine

Chapter 9

Redesign of the 3D last stage rotor

9.1 Redesign strategy

9.1.1 Overview and objectives

In this chapter, the long blade of the last stage rotor that has been used as reference in this research will be taken as a starting point for the redesign strategy. This will make use of the newly developed inverse design techniques.
Traditionally, a rotor like the one under consideration is designed by controlling directly the thickness distribution and other geometrical features such as blade angles, LE and TE geometry. More specifically, this rotor was designed by optimization of the 2D sections followed by specially devised stacking techniques. This procedure is the one presented by Senoo et al. [2010]. In their paper the 2D sections have been parametrised through splines, then optimized with a genetic algorithm, after introducing a variety of constraints and carefully selected objectives. The 3D surface was constructed by fitting NURBS surfaces to the stacked 2D profiles. Special attention has been given to the design of the tip section, employing a method of characteristics in order to create the supersonic flow passage geometry, as presented in the paper of Senoo and Ono [2013]. The very high stagger nature of these 2D sections required the development of targeted CFD tools such as the one described by Senoo et al. [2011].

With the above techniques, the resulting state-of-the art rotor displays a remarkable aerodynamic performance. However, this rotor is also known for its geometrical complexity, and in particular one of the biggest unresolved problems of such a geometry is the lack of smoothness of the blade surface. This lack of smoothness is the result of stacking a set of 2D blade profiles that vary so much in thickness, shape and stagger angle along the span. Specifically, many sections require a very complex thickness distribution, with changes in curvature and decambered airfoils. This complexity arises because the main technique employed in order to achieve the desired aerodynamic performance relies on the modification of the airfoil thickness.

The lack of smoothness is considered a drawback of the design, as it affects mechanical performance. Irregularities in the surface create stress concentrations. Furthermore, it adds to manufacturing costs, reduces reliability and makes the blade more prone to erosion related to water droplets build-ups typical of the two phase flows to which this blades are subject.

The main source of stress in long axial turbine blades such as this is usually related to centrifugal forces. The principal countermeasure to this is stacking the 2D profiles on a radial line going through their centre of gravity. Leaning the blade should also be avoided, as this can cause large bending stresses, which have a far greater influence then direct tensile stresses. The blades under consideration also display a high level of twist, so stacking along the centre of gravity also avoids the tendency of the blade to "straighten" under centrifugal tension.

The semi-inverse design techniques such as the one developed in this project, allow to specify a pre-determined thickness distribution, and then control the aerodynamic behaviour of the blade profile through camber line modifications. This means that the blade thickness can now be chosen in order to ensure smoothness of the resulting surface or it can be derived directly from mechanical considerations. This is in contrast with previous techniques that relied on the thickness distribution to control aerodynamics, making it very challenging to simultaneously handle mechanical performance.

The aim set in the present case is to create a redesigned 3D blade which will display a smoother surface and improved mechanical behaviour, with an aerodynamic performance close to or matching the original rotor. Note that the original

rotor is an industrial design resulting from decades of research targeting the achievement of maximum aerodynamic efficiency. The objective of the current exercise is to demonstrate the methodology and show how the surface smoothness can be easily improved and stresses reduced, even by setting a rapidly created smooth thickness distribution. The redesign problem can be considered very successful, since the geometrical and mechanical objectives have been achieved fully, with stage efficiency comparable to the original, resulting from visible improvements in flow structure at some span sections. Further improvements could be achieved with a study on the optimum thickness distribution, and perhaps by setting an optimization strategy in order to exceed the original aerodynamic performance.

9.1.2 Summary of proposed method

The adopted strategy consists of the redesign of individual 2D sections, then stacked along the centre of gravity. The 3D surface is construted by fitting a NURBS surface to the 2D profiles. The NURBS surface is of third degree to ensure continuity of slope gradient.
Specifically, the 2D sections redesign method starts from the smoothing of the complex thickness distribution. This is done by maintaining the LE and TE shape, then fitting a Bezier curve to a few selected points of the original distribution, imposing continuity of slope and curvature at the point of contact with LE and TE. The selection of the mid-chord control points of the thickness distribution was performed in order to remove irregularities in the resulting shape.
Imposing the smooth distribution to the original camber line gives a new blade profile, which is then used as a baseline for the inverse design (this is referred to as the *smooth baseline* for the remainder of the chapter).
Given that the modified thickness has the aim of producing a smoother blade surface with mainly structural considerations in mind, it is no surprise that the aerodynamic capability of the smooth baseline results to be inferior to the original blade.
It is then the objective of the inverse design to achieve a performance comparable

to the original one, by means of camber line modifications.
The approach adopted for this task starts from the flow analysis of the original blade profile and of the smooth baseline. The blade loading shape of the smooth baseline is then used as a starting point for the creation of the swirl velocity prescription. This is slightly modified so that the inlet and outlet values of swirl velocity match those computed with the original geometry, in order to restore the work output lost after the modification of the thickness distribution.
The next section addresses in more detail the 2D inverse design strategy of individual profiles. Then, in the final section of this chapter, the 3D blade is constructed, and the obtained aerodynamic and mechanical performance is measured with the use of commercial software, and compared to the original geometry.

9.2 Design of 2D sections

The design of the 3D rotor is the result of individual redesigns of a few 2D sections. This is considered an appropriate technique, given the small component of radial flow in this kind of turbine blade. In the present case, a simple redesign of a long last stage rotor is attempted, by creating 5 blade profiles which are then stacked along a line going through the centre of gravity of each profile. The aim here is to produce a smooth 3D surface, while maintaining similar aerodynamic and mechanical performance. This means that the complex thickness distributions used to control aerodynamics in the original design need to be simplified, as they resulted in irregularities on the 3D surface of the blade. This is achieved by smoothing the thickness distributions using splines, and then attempting to control the aerodynamics through inverse design.

9.2.1 30% span

The redesign of the profile at 30% span of the long last stage rotor constitutes a good example of the proposed procedure. The normal thickness distribution was smoothed by maintaining the original LE and TE shapes, then fitting a highly-differentiable Bezier curve to very few control points taken from the original thickness distribution. The continuity of slope was imposed at the LE and TE

portions. The original and modified ditributions are shown in figure 9.1a. The new thickness obtained was imposed on the original camber line, to construct the smooth baseline.
The flow analysis on this baseline geometry revealed a change in swirl velocity distribution from the original one, and most notably a reduction in work output due to the change in inlet and outlet swirl velocities.
The aim of the inverse design was therefore to recover the inlet and outlet circumferentially mass averaged swirl $\tilde{v}$ (figure 9.1b). The blade loading distribution corresponding to the prescribed swirl was chosen to be close to the one of the smooth baseline, which already showed some improvement with respect to the original one, in the form of a reduction in peak loading (figure 9.1d). The distribuition was modified so that the original work output could be recovered. This modification was obtained thorugh an iterative routine, which after fitting a spline to the original blade loading curve, moved a few control points simultaneously until the area under the curve produced the required work output. The movement of the blade loading control points is proportional to the magnitude of the swirl velocity meridional derivative at that location (so tha the overall shape of the curve is not distorted).
The inverse design procedure was run, setting convergence of each flow analysis to a RMS density error below 10^{-5}, and an exit criterion for the procedure set to camber point movements inferior to 0.1% of axial chord. This produced, within 15 iterations, a blade with $\tilde{v}$ distribution reasonably close to the prescription (figure 9.1c). As usal there are discrepancies near LE and TE as these portions are only adjusted geometrically. Other discrepancies are due to the choked nature of the flow, which means that small variations in throat area might occur, affecting the quality of the inverse design. The resulting blade profile and comparison in performance are available in section 9.3, where the 3D blade is presented and individual sections are compared.

9.2.2 75% span

The redesign of 75% span is the most successful example of how aerodynamics can be controlled through camber line modification rather than through thickness

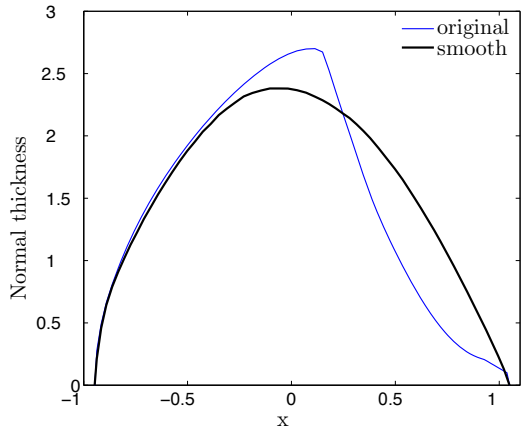

(a) thickness distribution (dimensions removed for confidentiality)

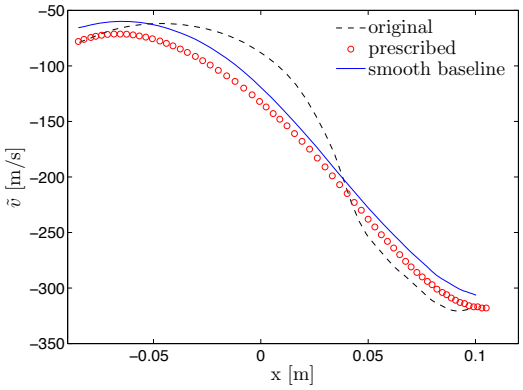

(b) setting the target swirl

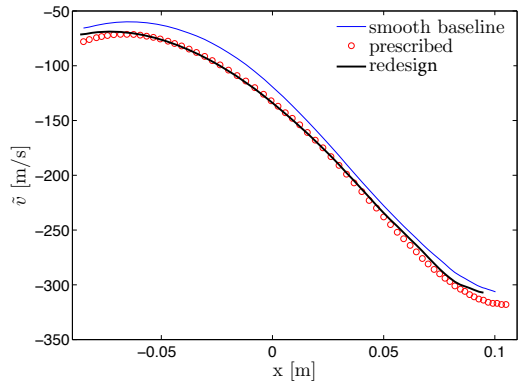

(c) obtained swirl distribution

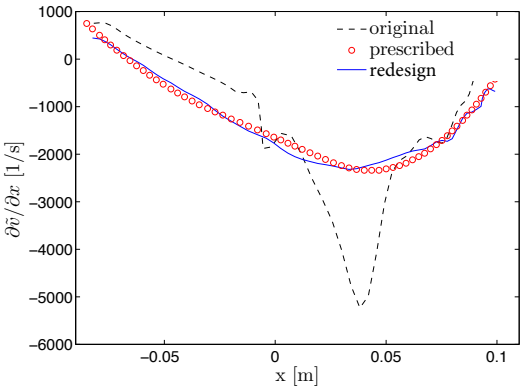

(d) setting the target loading

Figure 9.1: Plots of inverse design strategy at 30% span

distribution. The original thickness distribution for this section was specifically designed to give a convergent divergent flow passage. The resulting suction surface displayed two changes in curvature sign. The transition from this kind of profile to the positively curved ones near the hub causes an uneven 3D suction surface. Smoothing this profile is therefore a key step in obtaining a more uniform surface on the 3D blade.
The normal thickness distribution was modified as shown in figure 9.2a. The procedure is the same as before, with few control points, a high-degree curve and continuity of slope at LE and TE.
As for the previous case, modifying the thickness resulted in aerodynamic changes: the swirl velocity distribution for original and smooth baseline are shown in figure 9.2b, along with the prescribed one: once again the objective here is to maintain the original work output, without changing the blade loading curve excessively. The inverse design procedure was run with same convergence settings and exit criterion as used at 30% span.
Figure 9.2c shows that redesigned and target distributions are reasonably close. The resulting profile was employed in the 3D blade, and a discussion on the geometrical and aerodynamic features of the redesign is provided in section 9.3.

9.2.3 50% span

The blade profile at 50 % span was redesigned with a procedure similar to the one adopted for the previous cases, in sections 9.2.1 and 9.2.2. The normal thickness was modified by imposing a spline distribution onto the original camber line. The thickness distribution is shown in figure 9.3a. The resulting smooth baseline profile can be seen in figure 9.3b, superimposed on the original one.
Once again, the objective was to then inverse design the smooth baseline so that the original inlet and outlet $\tilde{v}$ could be restored. The blade loading distribution of the baseline showed some irregularities, due to a small peak in Mach number at mid-chord. The new blade loading distribution was made by fitting ten control points to the baseline loading curve, and then fitting a 4th degree spline. As before, the loading control points were adjusted iteratively with an automatic

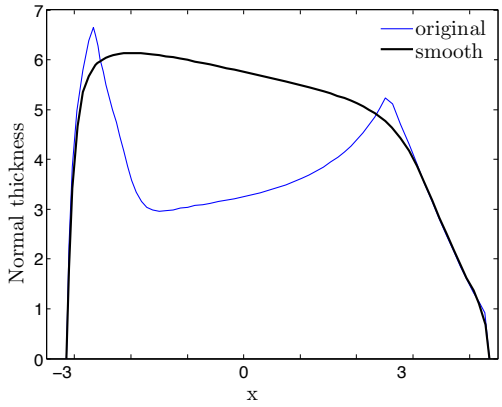

(a) thickness distribution (dimensions removed for confidentiality)

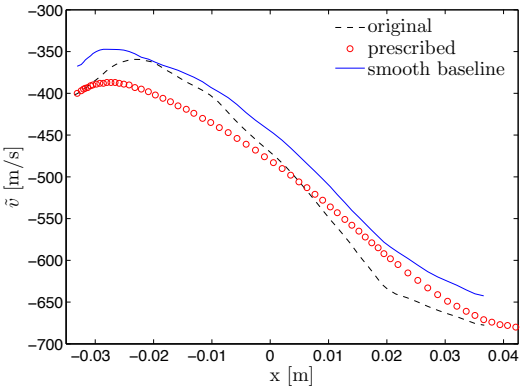

(b) setting the target swirl

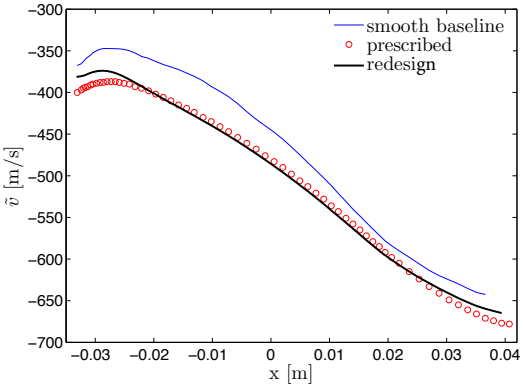

(c) obtained swirl distribution

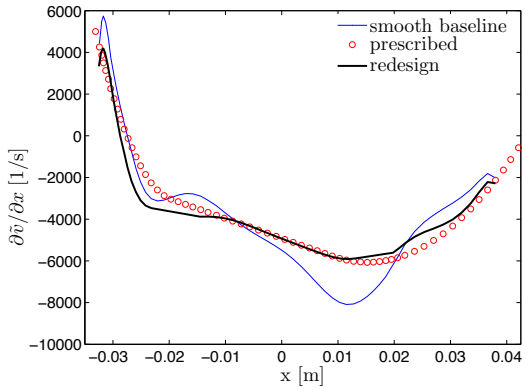

(d) setting the target loading

Figure 9.2: Plots of inverse design strategy at 75% span

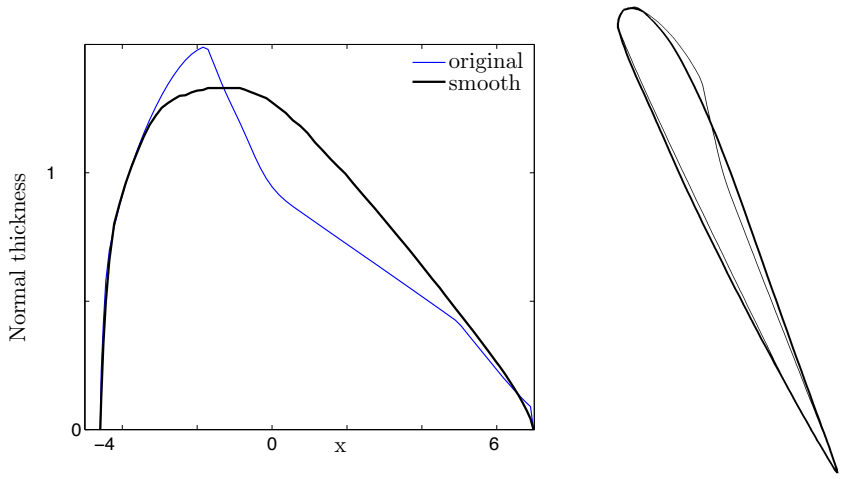

(a) thickness distribution (dimensions removed for confidentiality)

(b) smooth blade superimposed on original

Figure 9.3: Smoothing the 50 %span section

routine in order to achieve the required work output.
Figures 9.4a and 9.4b show the swirl velocity distribution and its meridional derivative respectively for the baseline, target and redesign. The exit criterion for the inverse procedure was set at camber point modifications smaller than 0.2 % of axial chord. This had to be set to be less strict than previous cases because the 50% span revealed to be more sensitive to small changes in throat area, so below a certain tolerance the blade modifications reduce slower than the changes in blade loading, which can cause problems in the convergence of the inverse design. The matching with the target achieved with the above setting is satisfactory, with the usual discrepancies at LE and TE.
How this blade profile performed in the 3D stage simulation is presented in section 9.3.

9.2.4 Hub and Tip

The hub and tip sections showed already a very regular thickness distribution, hence no redesign was needed for the purposes of a smoother 3D surface.
Furthermore the tip section required special design techniques in order to deal

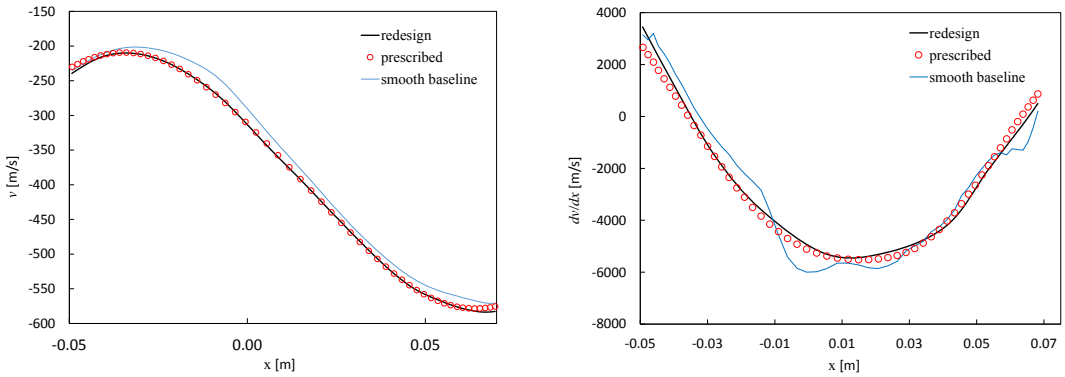

(a) swirl velocity distribution (b) obtained blade loading

Figure 9.4: Redesigning the 50% span smooth section

with shock reflections across its passage, and perhaps inverse design of this section will require coupling of the blade update algorithm with more advanced CFD techniques, which is beyond the scope of this research, but is definitely a topic of future interest.

The hub section did not require any changes in thickness distribution, hence no inverse design to recover the original work output. It was attempted to run an inverse design on this blade profile attempting to extract more work. However the tendency of such a prescription is to simply increase the stagger angle. This increase has to be kept within strict limits at a low-reaction hub section because it can increase the exit kinetic energy loss. Additionally it moves the trailing edge further away from the neutral axis of the blade profile, greatly increasing stresses at that location.

9.3 The 3D blade

9.3.1 Construction of the blade

The 3D blade was constructed using the profiles presented in section 9.2. The centre of gravity (CG) of each 2D profile was computed, and then the profiles were translated along their respective $z = const$ plane, so that all the CG points were

aligned on a line parallel to the z axis. This ensures a considerable reduction in bending stresses under centrifugal forces. The blade surface was then constructed by fitting a NURBS surface to the stacked blade profiles. This was 3rd degree to ensure continuity of curvature which, as seen from Bernoulli applied to a streamline, affects pressure gradients of the flow close to the blade. The trailing edges were closed imposing continuity of slope.
The solid blades can be observed in figures 9.5 and 9.6 where the improved surface smoothness of the redesign can be appreciated. Also notice, later on in figure 9.9, that the streamlines for the flow are approximately parallel to the meridional direction: the negligible component of radial flow confirms the 2D design to be an appropriate strategy for this kind of turbo-machine.

9.3.2 Stage flow simulation: a comparison

A 3D stage simulation with real steam properties was run in Ansys CFX for this case, in order to compare the aerodynamic performances of the original and the redesigned rotors. This is based on a RANS numerical solution with $\kappa - \epsilon$ turbulence model.
Steam tables for the properties of liquid and gas phases of the water mixture were generated using the available tools in the CFX utility. These are based on the IAPWS industrial formulation.
The stator-rotor configuration is shown in figure 9.7. The same stator was employed for both cases. The mesh was constructed in order to have a very long portion of computational domain downstream of the rotor. This portion of outlet domain is referred to as the out-block. Its purpose is to prevent discontinuities from hitting and reflecting at the outlet boundary. This is the only possible method in CFX since Ansys offers a non-reflecting outlet boundary condition only for the Fluent solver, but it is not available for the CFX turbomachinery solver. The overall mesh size in both cases was of about 0.9M nodes for the combined rotor and outlet domain.
The stage simulation was run on a single blade row, with periodic boundary and stage interface between stator outlet and rotor inlet. Convergence was set to RMS mass residuals below 10^{-5}, while the inlet and outlet mass flows were also mon-

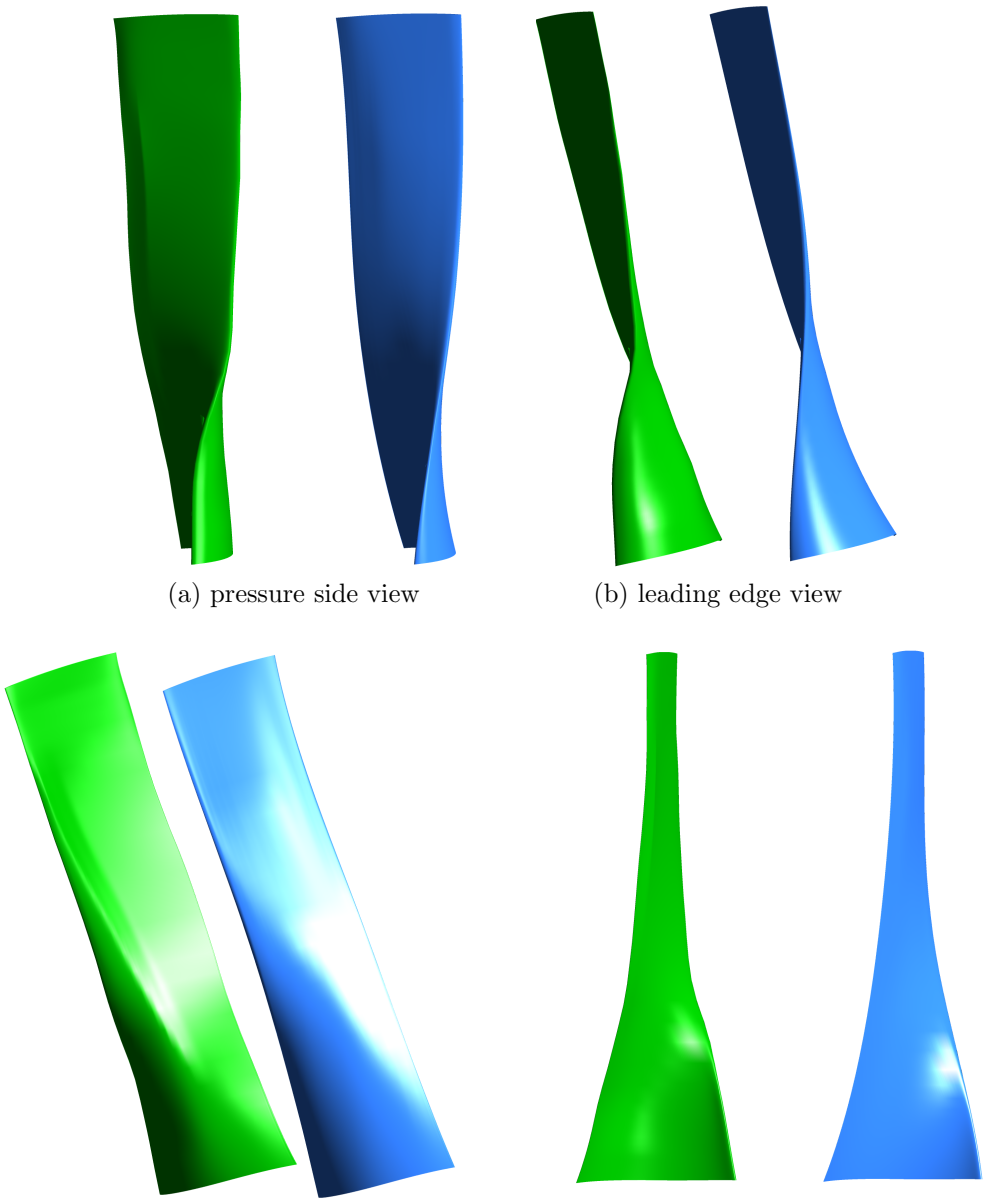

(a) pressure side view

(b) leading edge view

(c) suction side view

(d) meridional plane: pressure side

Figure 9.5: Comparison of original (green, left) and redesigned (blue, right) blade

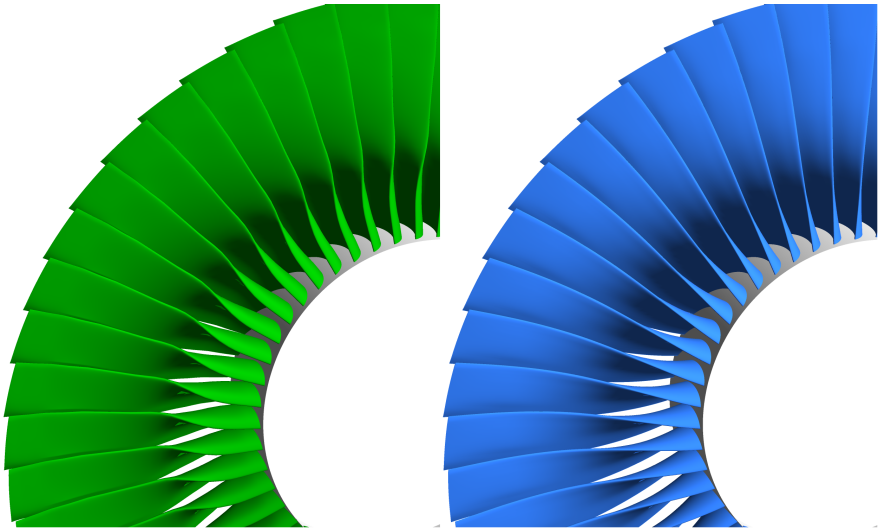

Figure 9.6: Partial view of full rotor, original (green left) and redesigned (blue, right)

itored as an indication of convergence, and oscillations completely disappeared within the first half of the total cumulative time.

The boundary conditions were the same in both cases. At the stator inlet, the stagnation pressure was set at $32kPa$ and the wetness fraction at 0.036 which, assuming phase equilibrium, set the inlet entropy value through the saturation temperature. At the stage outlet the static pressure was set to $5.6kPa$, at $3600rpm$. Both original and redesigned rotors produced, at design point, a power output of $22MW$, which means the first design objective of maintaining work output was achieved.

The efficiency comparison required multiple simulations to be run by changing inlet total pressure values. This is because the last stage rotor always operates under choked flow condition, so the mass flow is not affected by the back pressure (static pressure at rotor outlet). Thus, even though the back pressure experiences seasonal variations due to changes in condenser pressure, this does not affect the mass flow, but only the steam quality at outlet and the overall thermal cycle efficiency rather than the LP turbine alone.

At each different value of inlet total pressure corresponds a mass flow and a stage efficiency value. At the last stage, the total-to-static efficiency is considered, since the outlet kinetic energy is lost.

Because the working fluid is two phase, the turbine efficiency is measured using enthalpy values for the mixture, but the ideal static enthalpy at outlet H_{2s} cannot be computed from isentropic relations. The total-to-static efficiency of the turbine is given by:

$$\eta_{ts} = \frac{H_{o1} - H_{o2}}{H_{o1} - H_{2s}} \tag{9.1}$$

Where the subscript o denotes stagnation values, the 1 inlet values, the 2 outlet values, and the s is an isentropic value. The value of H_{2s} is the value of static enthalpy of the mixture at the outlet static pressure and inlet static entropy. This is computed by finding the inlet static entropy from the mixture using the inlet wetness mass fraction (from the flow solution). Using this value of entropy and the outlet static pressure, the ideal (isentropic) wetness mass fraction at the outlet can be computed. This is then used to find the value of isentropic enthalpy H_{2s}. In this case, all values from the flow solution are taken as circumferentially mass averaged across the whole inlet or outlet.

The resulting efficiency characteristics for original, smooth baseline and redesign are shown in figure 9.8a. It can be seen that simply modifiying the thickness distribution significantly lowered the performance of the stage, and that the inverse design managed to recover to a satisfactory level the high efficiency levels of the original rotor. Efficiency values at off-design are generally speaking higher for lower mass flow rates, but have dropped slightly at high mass flows.

At the design point the computed efficiency of the redesign is 0.3% shy of the original one [1]. The new computed efficiency is slightly lower, but it is a clear improvement from the smooth baseline which showed a work output of $21MW$ and a total-to-static isentropic efficiency 1.6% lower than the original (efficiency characteristics for the three cases are shown in figure 9.8a). Please note that the aim of the redesign was to produce a smooth surface with comparable aerodynamic performance, and improved mechanical behaviour, which has been fulfilled, as will be demonstrated later in the stress analysis.

A closer comparison between original and redesign shows that at some span sections the aerodynamic performance is improved, counter-acted by increased losses at other span sections, resulting in the new efficiency being close but still slightly

[1] Actual values of efficiency not stated upon manufacturer's request

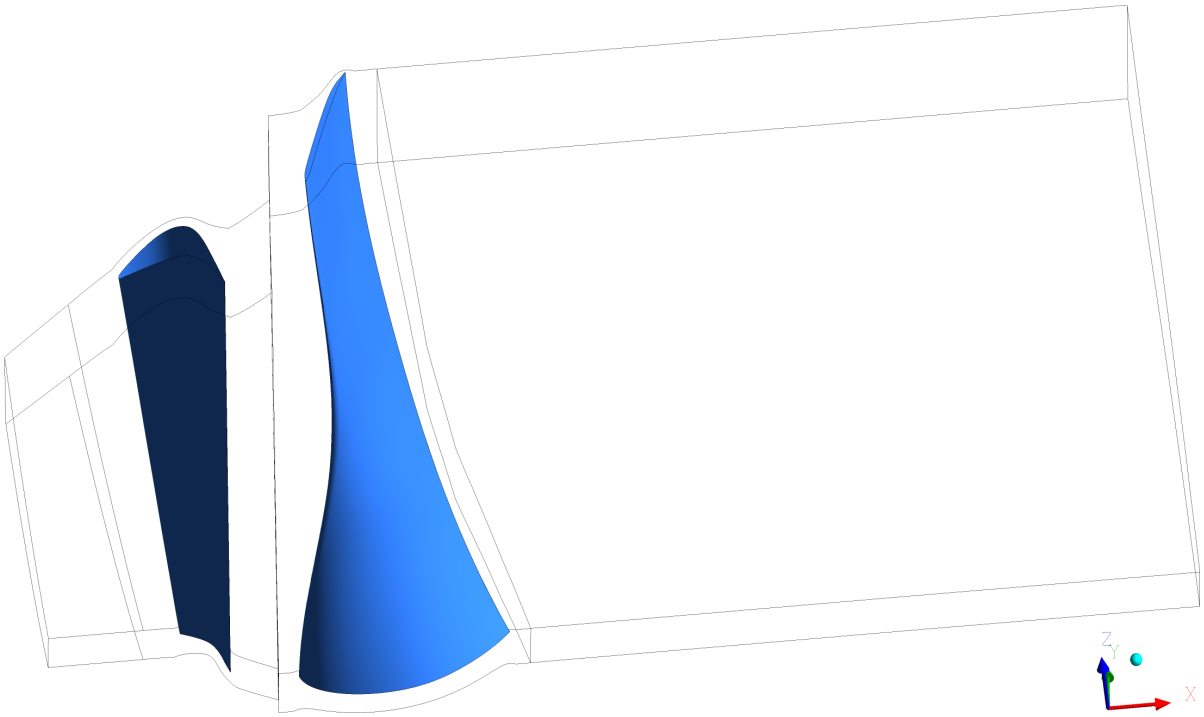

Figure 9.7: Stator-rotor arrangement for the redesign flow simulation; the wireframe delineates the computational domain, including the long out-block

lower than the original (an indication can be provided by the outlet entropy plot of figure 9.8b). The pressure contours for the different span sections are shown in figures 9.10 to 9.14, and the blade surface pressure plots are compared in figure 9.15. A discussion about each span location follows here.

9.3.2.1 30% span

Figure 9.11 shows a comparison between pressure contours of the flow through the original and redesigned rotors. The suction surface of the original profile starts with a large radius of curvature, with a rapid change of slope at mid chord followed by an inversion in curvature sign, which smoothly transitions into the flat portion near the TE. At the location of highest curvature (where there is a sudden change in slope), the flow accelerates rapidly, causing a mild shock and flow separation downstream. The low-pressure wake crosses the pressure side leg of the trailing edge fan. This is a well recognised set of loss generating

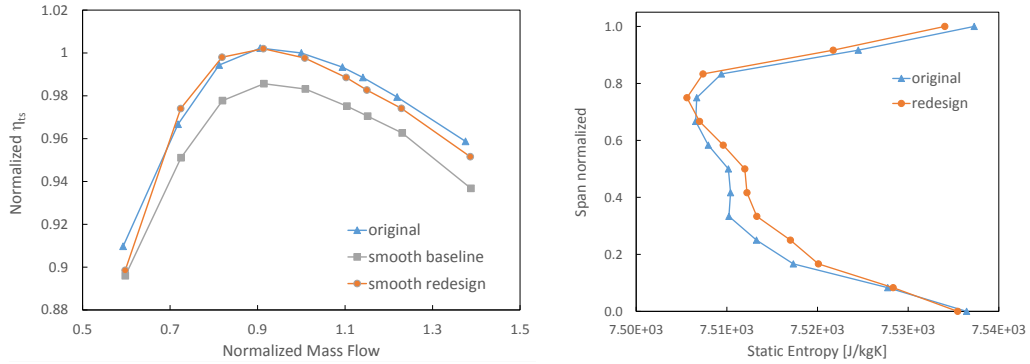

(a) total-to-static efficiency characteristic (b) outlet static entropy comparison

Figure 9.8: Efficiency comparison

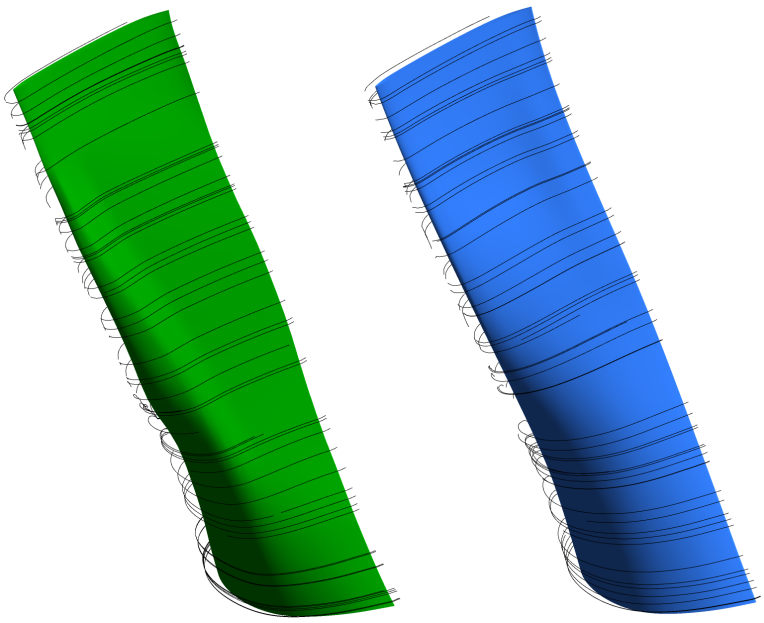

Figure 9.9: Streamline plot at a surface offset 2cm from the blade (original on the left, redesign on the right)

mechanisms. The situation is improved in the smooth redesign: the expansion process is more progressive, the shock at mid chord is eliminated together with the suction side flow separation. This can be observed in the pressure contour plots as well as in the surface pressure chart of figure 9.15b which clearly displays improved suction side flow . The stagger angle has been slightly increased by the inverse procedure, which ensures that the original exit swirl velocity is recovered.

9.3.2.2 5% span

In order to investigate the 2D profile behaviour near the hub, the blade section at 5% span is considered. At this location the endwall flow effects can be considered negligible, so the flow can be considered quasi-2D, and the analysis of the 2D profile becomes meaningful.
As mentioned before, the thickness distribution at the hub section did not require any modifications. However, when constructing the 3D blade by fitting a NURBS surface to the 2D profiles, the blade geometry in between two adjacent profiles is influenced by both sides. This means that even with a completely unmodified hub section, at 5% span the blade profile is affected by the new geometry at 30% span. In this particular case the effect observed by comparing the blade profiles in the plots of figure 9.10, is that the curvature of the blade has been reduced. This affected the work extracted at these sections. As a countermeasure to this, the stagger angle of the hub section was increased very slightly (1.5%). This resulted in the recovery of the work output. This can be observed in the blade surface pressure chart of figure 9.15a, where original and redesign plots are very similar to each other.

9.3.2.3 50% span

At 50% span the situation is very similar to what observed at 30% span. The location of rapid change in slope on the suction surface at approximately mid chord results in flow acceleration upstream of this point, and flow separation downstream. Also in this case the flow shows great improvements in the redesign, as shown in the contours of figure 9.12. The separation has been removed, together with the interaction between the consequent low pressure zone and the trailing

edge fan. Additionally it is noted that also in this case the stagger angle has increased slightly.
Despite the overall improvement in the flow, the redesign shows a flow discontinuity just downstream of the LE (see also the surface pressure plot of figure 9.15c), perhaps due to excessive acceleration at this location and a small flow separation. Ideally this could be removed with a more careful LE geometry design, which cannot be achieved directly with the inverse procedure.

9.3.2.4 75% span

Perhaps the best achievement of this exercise is the new design of the 75% span section. In figure 9.13 the new convergent-divergent passage obtained through camber line modification (rather than using thickness distribution) can be appreciated, along with the elimination of the strong normal shock at the throat (which has been made oblique): this is obvious in the blade loading plot of figure 9.15d. Furthermore, this profile shows the most improvements under a mechanical viewpoint too, as will be seen in subsection 9.3.3. The achievement obtained in the redesign of this span section exemplifies the potential of the new methodology: here, direct control over the blade thickness is available, allowing for a smooth blade profile creation. The aerodynamic behaviour desired is obtained through a completely new geometry, broadening the exploration of the design space.

9.3.2.5 95% span

Finally, near the the tip section, which was left unmodified, the flow shows a clear increase in upstream bow shock. Unfortunately, all the improvements in aerodynamic performance achieved at other span sections are then counter-acted by the increase in losses due to this diminishment of flow quality near at the tip. This is because the region near the tip experiences the highest flow rate and work extraction, which means that an increase in entropy generation at this location has a far greater effect on the overall efficiency than the other sections. Figure 9.8b confirms what just stated: the redesign shows lower outlet values of mass averaged static entropy everywhere along the span, with the exception of the tip section.

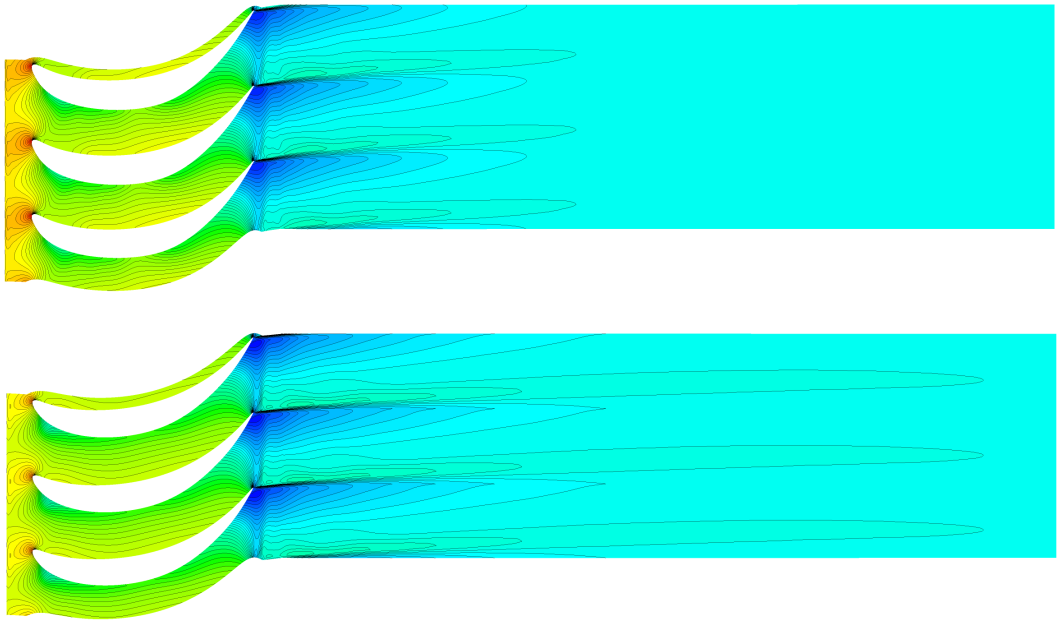

Figure 9.10: Pressure contours for 5% span section (Top: original, bottom: redesign)

However, despite a few trials having been conducted no improved design was found through the inverse design procedure for the tip section. This is probably because of the complex shock structure that was handled in the original design through a careful choice of outlet metal angle. The camber update procedure clearly attempts to reduce this angle in order to achieve the prescribed outlet swirl, failing to account for the optimal shock reflection structure which still to date requires a method of characteristics to be carefully predicted (as seen in Senoo and Ono [2013]).

9.3.2.6 Overall

The 3D plots of pressure contours in figure 9.16 reinforce what presented so far: on the pressure side, clear improvements are visible between 50% and 75% span (the shock strength near LE is reduced), but the shock near the tip (the impinging bow shock) is now stronger. Further improvements are visible on the suction side of the new rotor, at the LE above 50% span.

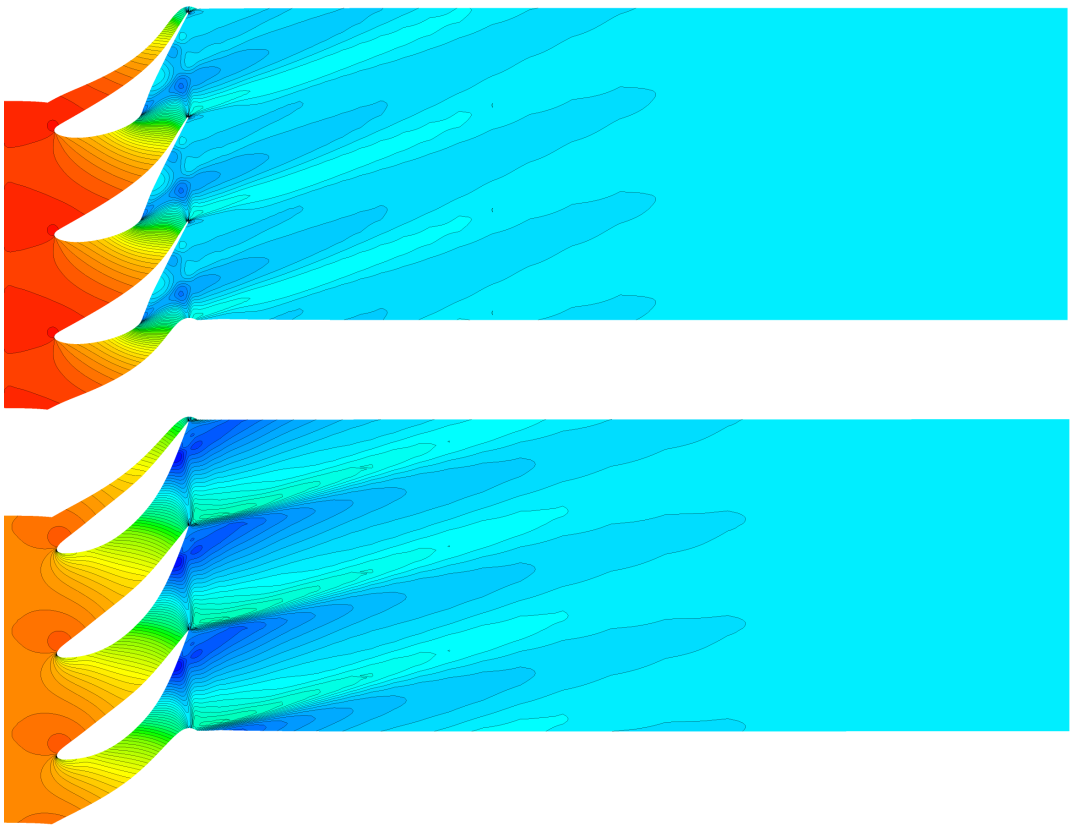

Figure 9.11: Pressure contours for 30% span section (Top: original, bottom: redesign)

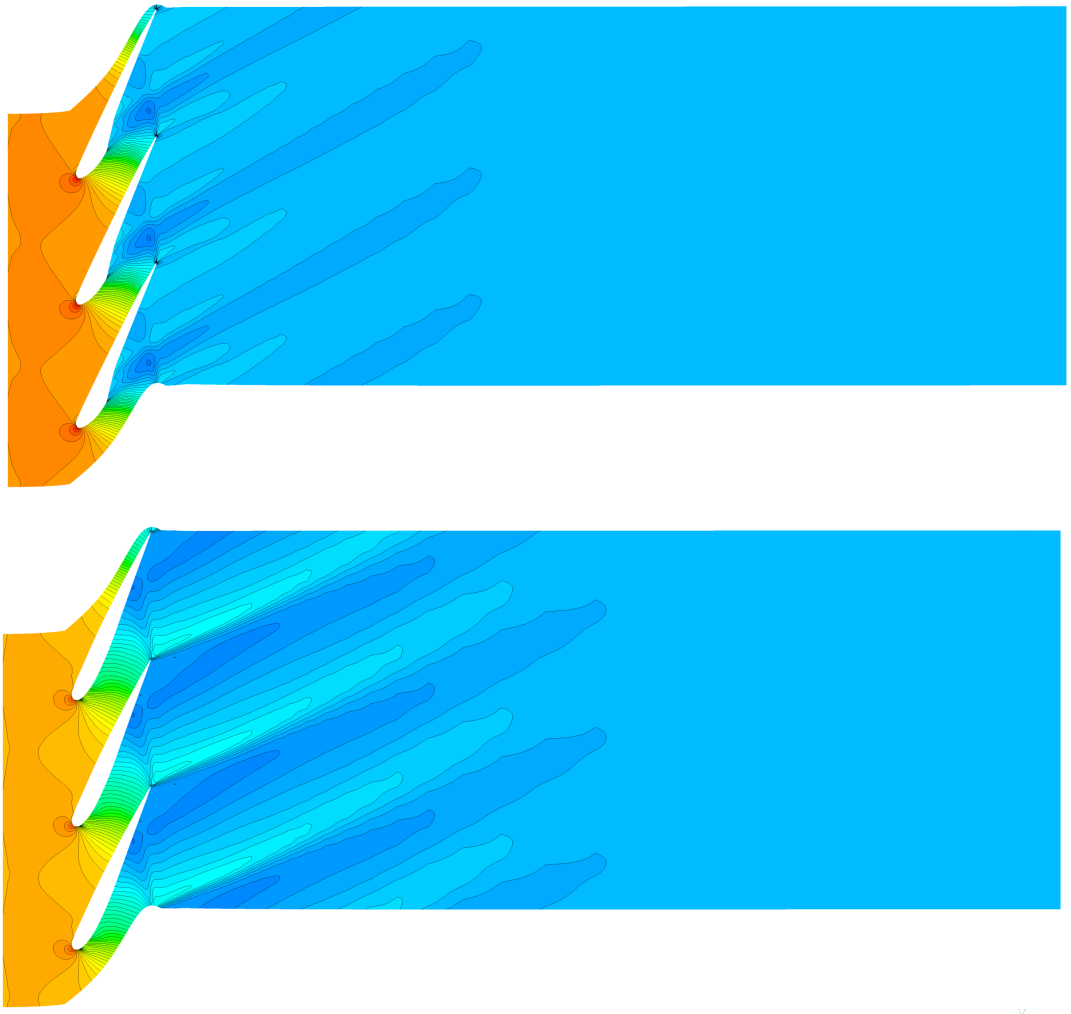

Figure 9.12: Pressure contours for 50% span section (Top: original, bottom: redesign)

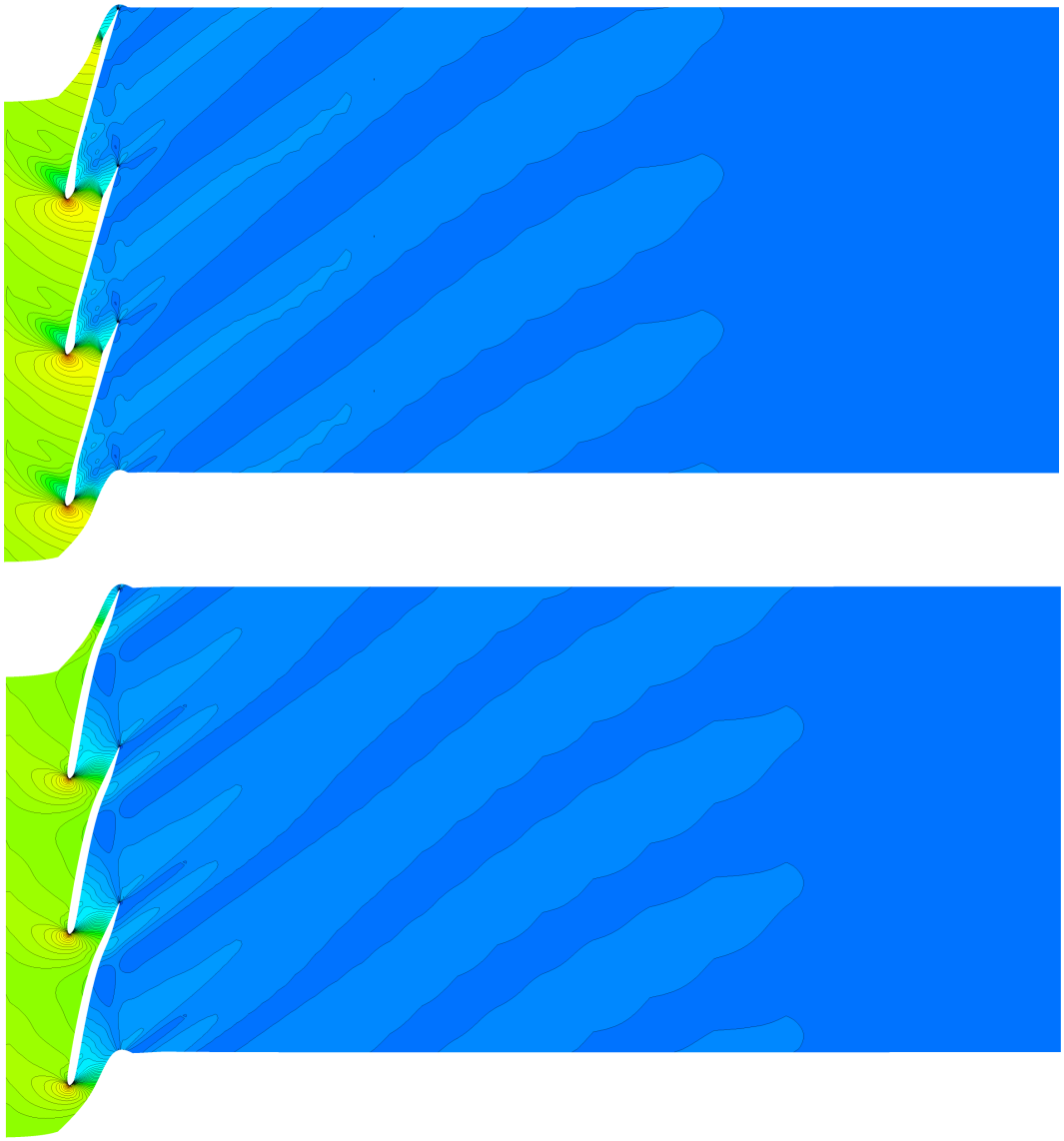

Figure 9.13: Pressure contours for 75% span section (Top: original, bottom: redesign)

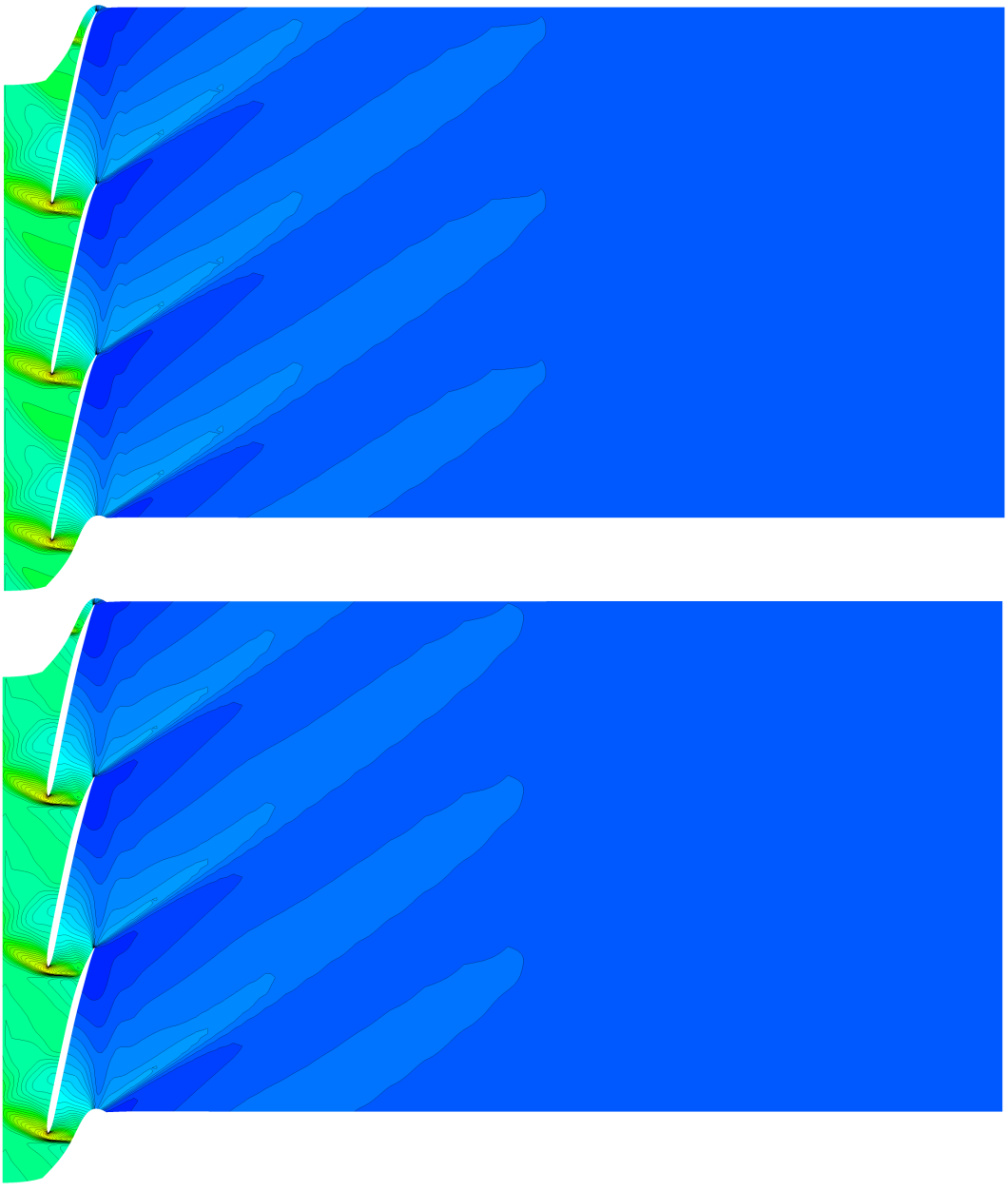

Figure 9.14: Pressure contours for 95% span section (Top: original, bottom: redesign)

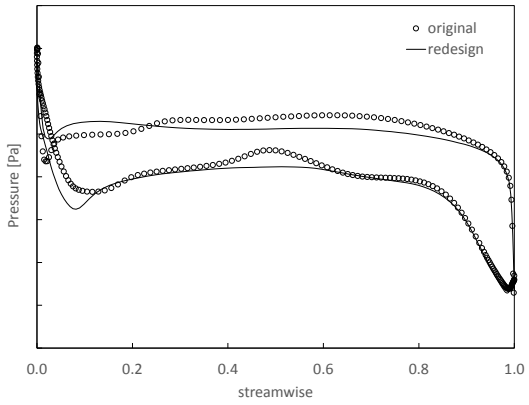

(a) 5 % span

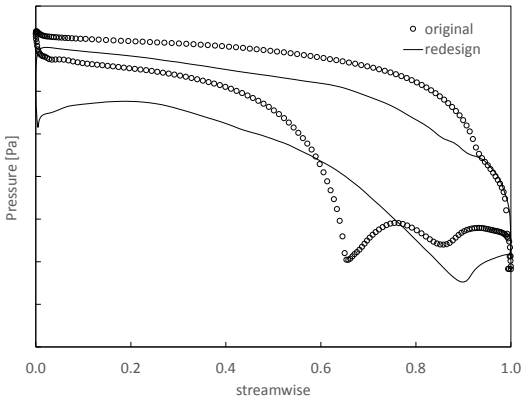

(b) 30 % span

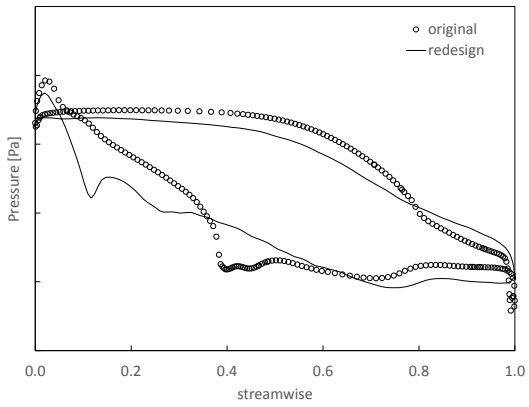

(c) 50 % span

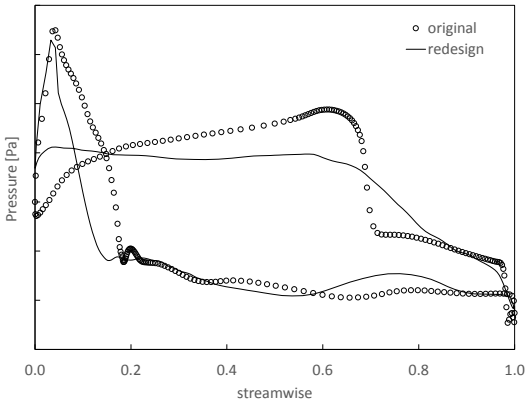

(d) 75 % span

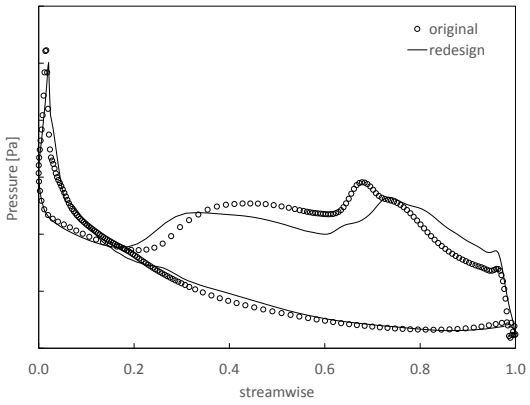

(e) 95 % span

Figure 9.15: Blade surface pressures. Dimensions removed for confidentiality

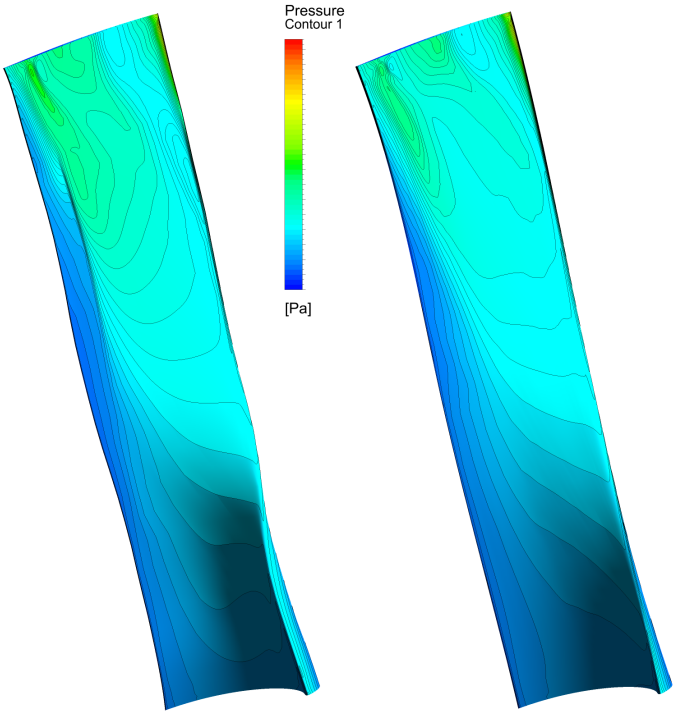

(a) pressure surface

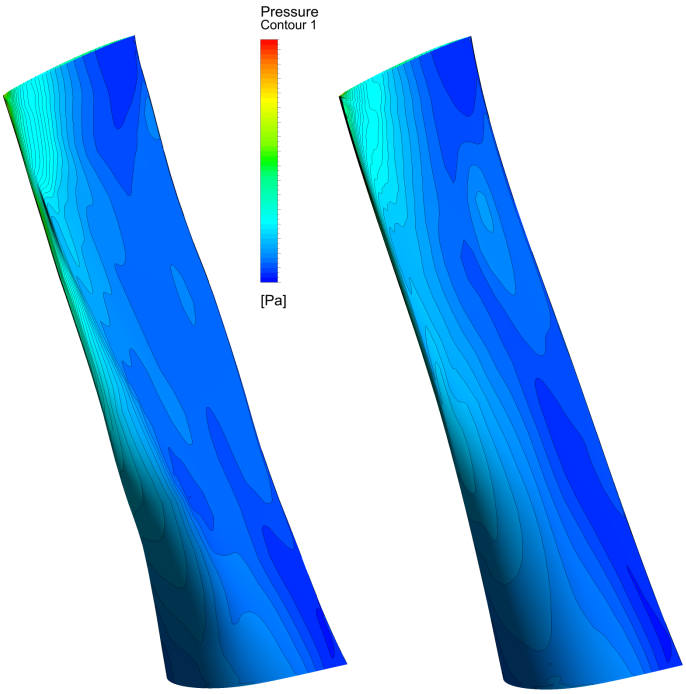

(b) suction surface

Figure 9.16: Surface pressure contours. Original on the left, redesign on the right. Dimensions removed for confidentiality

9.3.3 Centrifugal stresses

The primary source of stress in such a long rotor blade is by far the centrifugal stress. To this, the loading from the flow should be added, but for the purposes of a quick comparison it is enough to consider the bending due to centrifugal force alone.

In an Ansys FEA simulation, both blades where rigidly supported at the hub and a rotational speed of $3600rpm$ was applied. The material used was alloy Ti-Al6-6V-2Sn. The resulting equivalent stress is shown in figure 9.17 for both blades.

As for the aerodynamic case, some locations show improvement and some diminishment. The maximum stress of the new design is reduced by 29%, however the original maximum seems to be due to a stress concentration near the TE of the hub, which could be possibly eliminated when introducing a fillet at the base. The suction side of the redesign in figure 9.17 shows obvious improvement, most notably near about 75% span.

On the suction side there is improvement near 75% span, but a sharp increase in stress just below 50% span. Arguably, given that some extra bending will be added by the flow loading in the direction of rotation, it is better to have reductions in tensile stress on the pressure side than on the suction side (as for the present case), since it is possible that the compression on the suction side due to flow loading induced bending will compensate for this to an extent.

9.3.4 Conclusion

Overall, the new design achieved aerodynamic and mechanical performance comparable in quality to the original one, but with a smoother surface. The ability to specify a normal thickness is key, since structural integrity can be retained during camber updates by the inverse design. Furthermore it allows the imposition of a smooth thickness distribution, and then achieve the required aerodynamic features, such as convergent-divergent passage, through the camber modifications rather than through a complex thickness. The advantage of this is generally appreciated when stacking the 2D profiles and a smooth 3D blade surface is attained, which is generally desirable under a manufacturing viewpoint. More advanced

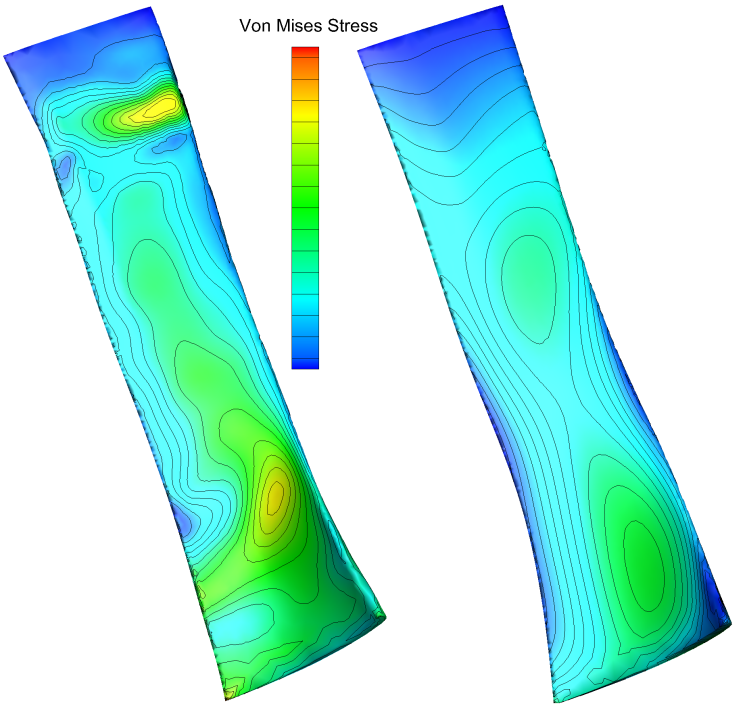

(a) pressure surface

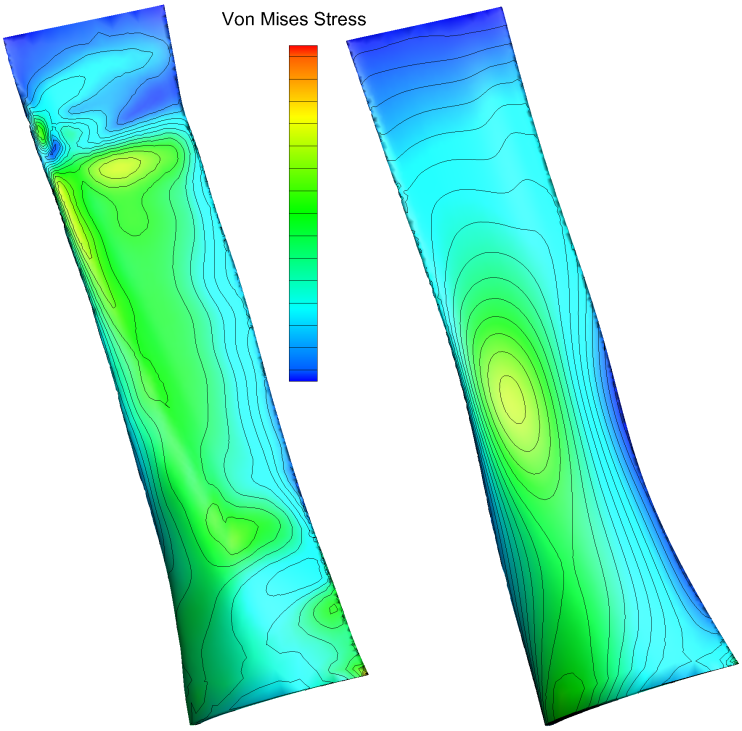

(b) suction surface

Figure 9.17: Equivalent stress (Von Mises). Original on the left, redesign on the right. Dimensions removed for confidentiality

design work is beyond the scope of this research, but possible lines of work can include careful choice of the smooth normal thickness to be imposed, and further investigation of what blade loading prescriptions are optimal for the specific case of the flow though the long last stage rotor.

Chapter 10

Conclusion

10.1 Context

The design tendency in modern last stage rotors of steam turbines is to increase size to the limits allowed by current technology availability and cost. This is done in an attempt to extract as much work as possible before delivering the steam back to the condenser, by minimizing the thermal and kinetic energy of the leaving working fluid. This is of crucial importance given that in a typical supercritical steam power plant the last stage of the LP turbine is responsible for the extraction of 10-15% of the total power output of the cycle.

As a result of this, last stages are characterised by large flow rates and high tip speeds. Rapid steam expansion, transonic and supersonic flow regimes, pressure shocks and expansion fans, all have to be taken into account when designing the long axial blades of this turbo-machine. Additionally the thermal cycle requires expansion of steam below the saturation line, which means that the working fluid enters the last stage already as a two-phase mixture. This provides additional challenges to the design, not only under a flow analyisis viewpoint, but also because the blades have to cope with erosion, braking losses, thermodynamic losses, water build-ups, and possible dynamic excitation due to larger droplets shedding at trailing edge.

The large size of the rotor means that the blade profiles have very different geometrical requirements along the span, from the hub which is closer to impulse flow, to the tip which is typically a high or full reaction turbine airfoil. A whole-

some 3D design of this kind of blade is still at present a demanding task, especially when trying to ensure mechanical reliability and smoothness of the 3D surface. Stacking techniques give control over the 3D aerodynamic behaviour of the blade, for example by controlling lean and sweep. In the case of last stage rotors, however, these techniques are to be avoided for structural reasons, since features such as lean and sweep will result in excessive bending moments in the blade under centrifugal load. Thus, the main 3D feature present in these long blades is a high level of twist, resulting from the large variation in stagger angle from hub to tip, as a consequence of the required radial variation in flow reaction. Precisely this feature, along with the considerable difference in blade profile shape along the span, makes the full geometrical parametrisation of the blade a rather cumbersome endeavour, especially when considering that stacking techniques employed on blades of lower aspect ratio are not applicable in this case. This remark, together with the fact that the radial component of the flow through the last stage rotors considered in this study are negligible in most scenrios, makes it apparent that the use of a 2D profile design method is very suitable and in fact recommended as a starting point of the develompent of a new methodology. In traditional design methds, this apporach implies the parametrization of 2D blade profiles through a variety of techniques, which can be found in past and recent literature. The parametrization is then coupled with a set of performance evaluation techniques, which provide feedback for the iterative design procedure. Inverse design was chosen in the present case because of its distinguishing feature of providing a unified way of parametrising the blade through blade loading coefficients and also providing a more direct control over the aerodynamics of the blade. This latter consideration is a refelction of the fact that most of the aerodyamic behaviour of the turbomachine can be directly correlated to the blade loading.

10.2 Project achievements

Inverse design has been successfully applied in industry over the years, traditionally to radial machines, thin blades, or thick, low-aspect ratio ones. The most widespread technique is the one based on prescription of swirl velocity, coupled

with a potential flow solution.
These traditional inverse methods showed limitations when applied to the long rotors which charactherize the last stage of a steam turbine. The main limitations were linked to two key aspects: the *wet steam flow* and the *geometrical complexity* of the blade. The fact that these turbines operate under steam conditions which are far from ideal gas behaviour, due to the presence of the liquid water phase, made all existing inverse methodologies inaccurate in their flow evaluation component. Additionally it was discovered that traditional methods based on a tangential thickness specification were not suitable for the high stagger blade profiles typical of last stage rotors, due to the high levels of shape distortion resulting from such an inappropriate representaion. This consideration made clear that any blade update algorithm available in literature to the autor's knowledge was not compatible with the blade geometry under consideration. The need for a modified flow solver and a blade update algorithm with foundations on a different blade representation meant that of a novel inverse design approach had to be created, similar to none previously available. This included the evaluation of gas and liquid water properties for the two phase flow and a new blade update algorithm, in which the blade profiles could be represented through a camber line and the blade thickness normal to it (as opposed to tangential). The newly devised method was then applied to the complete redesign of an actual rotor, with improved surface smoothness and mechanical integrity, without compromising aerodynamic performance.

10.2.0.1 Inclusion of steam properties

Running inverse design under a perfect gas assumption will result in the output of geometries that will not operate optimally in a two phase scenario. This is because the surface pressure - and therefore the blade loading - are affected by the release of latent heat when the liquid phase mass fraction increases during expansion.
In this project, the flow solver employed in the inverse design procedure was coupled with steam tables generated specifically for the required range of operating pressures and temperatures, employing the formuations provided by the IAPWS.

The use of a fast look-up method for steam properties is computationally more efficient than evaluating the equations of state at each flow solver iteration, and also far less cumbersome and time consuming than including a non-equilibrium module for the estimate of droplet nucleation and condensation. This method was furthermore considered appropriate for the present case on the basis of two main assumptions. The first is that the expanding steam enters the last stage of the turbine already under two-phase conditions, which is always the case in a broad range of plant operating conditions. The second assumption is of thermodynamic equilibrium between phases. While this is only an idealization when considering the fast expansion rates which characterise the last stage, it is also true that the bulk of the nucleation happens upstream of the stage. Therefore this assumption still provides a more accurate representation of reality, especially with respect to the ideal gas one.
The effect of using a real gas assumption and including two-phase propeties into the inverse design procedure was significant. This is because the blade modifications are driven by differences between a computed and a prescribed flow quantity. Running two invere designs on the same blade, imposing the same blade loading but evaluating the flow under ideal and real gas assumptions respectively, produced different converged geometries. Successive flow analysis on each individual blade proved the improved performance under real gas condition of the former geometry.

10.2.0.2 New blade representation and update algortithm

The problem of available inverse design techniques did not reside only in the flow solver component, but it was inherent to the blade update procedure itself. In the most commonly employed inverse design techniques, the blade profiles are represented by imposing a tangential thickness to a camber line. This technique fails to accurately represent the blade or to effectively reconstruct the profile from a camber line when the stagger angles become too large. Most notable problems encoutered were the distortion in blade shape during the update procedure or the difficulty in modifying considerable portions of the pressure surface in the proximity of the leading edge. An alternative and more suitable representation of

this kind of blades was deemed to be the normal thickness representation, where the thickness distribution is evaluated through segments which are perpendicular to the camber line. While preserving the normal thickness has been used in the past as a design strategy during an inverse procedure, the existing methods which adopted this strategy in the past still relied on a blade update algorithm based on a tangential thickness representation. The level of approximation intoroduced by such an approach caused the inverse procedure to diverge in the case of high stagger blades,or decambered blades. It was therefore necessary to create a new blade update algortihm which laid its fundation on the premise of imposing a normal thickness distribution. This novel method, like previous ones is based on the specification of the circumferentially mass average swirl velocity distribution, with the main differences being the robust imposition of a predetermined normal thickness curve and modification of the camber line using only velocities computed from on the suction side of the blade. This latter characteristic of the method was required because unlike what happened in the tangential thickness methods, using velocity information from suction side and pressure side simultaneously to determine the movement of the camber line could result in lack of convergence of the design procedure, due to the misalignment of the normal thickness vectors with the tangential direction. The methodology proved effective and provides for the very first time a unique tool for the inverse design of this kind of turbomachinery blades.

10.2.0.3 Three-dimensional blade redesign

With the use of the newly devised inverse design technique, an existing 50in last stage rotor was redesigned completely. The main objective of the redesign was the achievement of a smooth 3D surface and improved mechanical performance. The overall strategy consisted of the inverse redesign of a few key 2D sections, which were then stacked along their centre of gravity to form the full 3D blade after fitting a NURBS surface. Having the new inverse design tool available made possible a very innovative approach to the redesign of the blade, consisting of controlling aerodynamic performance through camber line modification while fo-

cusing the selection of the thickness distribution on structural considerations. In this particular case, trying to achieve a smoother surface had the main purpose of reducing stresses under centrufugal forces, improving manufcturability and making the blade less prone to erosion and consequent long term loss of performance. The simple modification in normal thickness distribution, followed by recovery of aerodynamic performance through the prescription of a carefully selected blade loading, made possible remarkable reduction in equivalent stress under centrifugal load, without consequence on the overall efficiency of the stage. While this on its own can be considered a notable achievement, it also opens doors for future work on aerodynamic improvements coupled with stress analysis, in the context of more advanced optimization strategies where the novel inverse desing method will play a key role in the parametrization of the blade profiles and exploration of novel design spaces.

10.3 Further work

10.3.0.1 Including thickness distribution in an optimization strategy

Improvements to the overall blade design could come from a more careful selection of the blade thickness distribution. This could, for example, originate from considerations on the second moment of area, and the response under load. Alternatively, a hybrid strategy could be employed, in which the flow is controlled not only by the camber line modification, but with the influence of aerodynamic requirements also on the thickness distribution. These suggestions could all be part of future research, together with investigations on optimal blade loading prescriptions or combinations of load and thickness distributions, through sensitivity analysis such as design of experiments. This relates closely to possible implementation of the inverse method in automatic optimization strategies. The form adopted by an optimization would depend on the chosen parametrization, objectives and constraints. In this case the parametrezation could take the form of a few constrained control points defining the prescribed blade loading which, in association with a specified thickness distribution, could functionally define

a broad design space for the blade profile geometry. The thickness distribution itself could be manipulated by the optimizer, with the inclusion of meaningful constraints. The objectives of the design problems could span thorugh a variety of multi-disciplinary requirements, relating to fluid mechanics, stress analisys or manufacturing considerations.

10.3.0.2 Work on flow solvers

Additional work could be also carried out in the investigation of the most effective type of flow solution in the context of an inverse design procedure. The modularity of the blade update algorithm allows the coupling with other solvers, perhaps based on different grid topologies, or unstructured meshes. Also, the blade update itself could be conceptually modified in order to work with viscous solutions. Of interest could be to what extent the accuracy of inverse design solvers can be increased within practical limits. It should not be forgotten that inverse design remains an interim design tool, and to achieve the final geometry more often than not requires further refinement, in terms of LE and TE geometries, endwalls, fillets, shroud design and other features. Thus, in contrast to what just suggested, another interesting research would be on the coupling of the new normal thickness blade update with a more rapid flow evaluation methods, such as potential methods, as opposed to more accurate time-marching methods. This could take the time for complete inverse designs of a new geometry down to few seconds on a modern multi-core workstation (rather than the minutes required by time-marching methods), making automatic optimization more attractive for the creation of a radically new baseline geometry.

10.3.0.3 Work on 2D and 3D blade update algorithm

Other aspects of the current project that could be the basis of future work are the possible extension to a 3D inverse method, where a 3D flow solution is used to update a camber surface, and then through a thickness distribution the 3D

blade surface could be constructed. Notably, this provides the designer with the ability of specifying the spanwise work distribution, with remarakble control over the overall aerodynamic perfomance of the blade.
Finally, in more general terms, the normal thickness blade representation could be used as the basis of conceptually different blade update techniques. An interesting example would be the prescription of a pressure jump Δp, similar to the modern ones based on virtual velocities rather than on transpirating walls. This is because some blade update formulae based on transpirating walls were already developed in the course of this research, but due to the assumptions needed in the imposition of the boundary conditions during the flow solution, they proved to be incompatible with the type of blade profiles considered here, and are generally speaking not recommended.

Appendix A: Non-equilibrium wet flow calculations

.1 Introduction

As it is often the case in last few stages of LP turbines, rapid expansions cause the steam to suddenly cross the saturation line, i.e. it becomes *supersaturated* (or "subcooled"). This is a non-equilibrium state, since the steam gas-phase is at a pressure and temperature in the equilibrium two-phase region, but the liquid phase has not appeared yet. The gas can expand in the subcooled region until a critical supersaturation is reached, after which water droplets will nucleate and subsequently grow in size.

The condensation of steam onto growing droplets happens through an irreversible heat transfer process from the droplet to the surrounding vapour. This causes *thermodynamic losses* that must be accounted for when designing LP turbines. Additional losses directly linked to wetness are the so called *moisture losses*, i.e. those due to droplet drag and impact, or blade corrosion.

Furthermore, *indirect losses* are caused by the effects of condensation on the aerodynamics of the turbine flow, by changing blade loading, flow angles, shock structure and effectively causing off-design operation.

Possibly one of the most noticeable non-equilibrium effects on aerodynamics is the *condensation shock*, i.e. a sudden rise in pressure at the onset of nucleation due to sudden release of latent heat of condensation. This effect can be captured computationally only by using models of the nucleation and growth of water

droplets.
The advantage of this theory over the equilibrium case of the previous chapter, is the ability to deal with flows that enter the turbine dry (superheated or subcooled), and expand into a nucleating region. Also, if the steam is already wet at inlet, secondary nucleation might be captured where expansion rates are rapid enough to cause it. Finally, non-equilibrium methods allow the estimation of droplet size spectrum, helping designing against moisture losses. The disadvantages over the equilibrium calculations are the computational complexity, the theoretical uncertainties due to the relative novelty of these techniques, and the scarcity of experimental data to validate computer codes.

.2 Computation of non-equilibrium effects

.2.1 Structure of the nucleating wet-flow computation

The computation of condensing steam flows generally involves the numerical solution of the governing equations of fluid flow (e.g. 3.4) coupled with "wetness" equations derived from classical nucleation theory, which predict droplet formation and growth. This coupling is achieved as follows.
The wetness fraction and liquid specific internal energy are periodically computed by a set of wet steam procedures, and passed on to the time marching flow solver, which in turn makes available a new solution for the mixture internal energy and density. From these, the gas internal energy and density are found from the relationships:

$$e = (1 - y)e_g + ye_l \tag{1}$$

$$\frac{1}{\rho} = \frac{y}{\rho_l} + \frac{1 - y}{\rho_g} \approx \frac{1 - y}{\rho_g} \tag{2}$$

Where y is wetness fraction, and the subscripts l and g stand for liquid and gas phase respectively.
The values of gas pressure and temperature are then looked up on a table of stored p, T for the given ρ_g and e_g coordinates.

It is assumed that the mixture pressure is approximately equal to the partial pressure of the gas phase and that no slip occurs between the two phases.

Considering a single group of droplets, the nucleation rate J will determine the number of droplets formed:

$$N^{t+\delta t} = N^t + J\delta t \tag{3}$$

And the growth rate will determine their size (radius r). The wetness fraction is thus:

$$y = \frac{4\pi}{3}\rho_l N r^3 \tag{4}$$

.2.2 Description of equations

.2.2.1 Nucleation rate

Condensation of subcooled steam occurs through the nucleation and growth of water droplets. This growth process can proceed spontaneously only when the free Gibbs energy of the system is reduced. When considering randomly formed clusters of water molecules in subcooled steam, an initial increase in size requires an increase in Gibbs energy due to the energy stored as surface tension on the droplet. The classical expression for the change of Gibbs free energy ΔG for a spherical droplet of radius r is:

$$\Delta G = 4\pi r^2\sigma - \frac{4}{3}\pi r^3 \rho_l R T_g \ln S \tag{5}$$

where σ is the liquid surface tension, ρ_l is the liquid density, and S is the supersaturation ratio, i.e. the ratio between gas pressure and saturation pressure at the gas temperature. Only when a cluster reaches the critical radius the volume term in (5) will be reducing faster than the increase in surface tension. Growth then becomes a thermodynamically favourable process. The Kelvin-Helmholtz

critical radius is given by:

$$r_* = \frac{2\sigma}{\rho_l R T_g \ln S} \tag{6}$$

The rate at which droplets of critical radius are formed by random agglomeration of water molecules is modelled by the nucleation theory. The classical nucleation rate equation with correction for non-isothermal assumption made by Kantrowitz [1951] and correction for partial pressure of clusters by Courtney [1961] is:

$$J = \frac{q}{1+\theta}\left(\frac{2\sigma}{\pi m}\right)^{\frac{1}{2}} \frac{\rho_s(T_g)}{\rho_l} \exp\left(-\frac{4\pi\sigma r_*^2}{3k_b T_g}\right) \tag{7}$$

Where q is a condensation coefficient set to 1 in this case, m is the mass of a water molecule, $\rho_s(T_g)$ is saturation density at gas temperature T_g, and k_b is the Ludwig Boltzmann's constant. The isothermal correction factor θ formulated by Kantrowitz [1951] was rearranged by Bakhtar et al. [1980] as follows:

$$\theta = \frac{q\rho_g}{\alpha_r}\left(\frac{RT_g}{2\pi}\right)^{\frac{1}{2}}\left(\frac{h_{fg}^2}{RT_g^2} - \frac{h_{fg}}{2T_g}\right) \tag{8}$$

Where α_r is the heat transfer coefficient for a droplet of radius r, and h_{fg} is enthalpy of evaporation. A modified version of the above with an approximation for low pressure steam specific heat ratio $\gamma \approx 1.32$ is given by Young [1992]:

$$\theta = \frac{2(\gamma-1)}{R(\gamma+1)}\left(\frac{h_{fg}^2}{RT_g^2} - \frac{h_{fg}}{2T_g}\right) \tag{9}$$

.2.2.2 Growth rate

As water molecules condense on existing water droplets, latent heat is released to the liquid, raising the droplet temperature with respect to the surrounding vapour. This temperature differential allows the heat to be transferred back to the surrounding, hence growth to proceed. The rate of latent heat release and hence the rate at which the droplets grow is therefore controlled by the speed at which the energy can be transferred from the liquid to the vapour. Using the expression by Jackson and Davidson [1983], neglecting interphase slip and

considering only small changes in the liquid enthalpy between adjacent points on the computational streamline, the expression for growth can be written as:

$$\frac{Dm}{Dt} = 4\pi r^2 \alpha_r \frac{(T_l - T_g)}{(h_g - h_l)} \tag{10}$$

Or, in terms of radius:

$$\frac{Dr}{Dt} = \frac{\alpha_r (T_l - T_g)}{\rho_l (h_g - h_l)} \tag{11}$$

Where α_r is the heat transfer coefficient at radius r. A general expression adapted for any droplet size was suggested by Gyarmathy, and is used by Bakhtar et al. [2005] in the form:

$$\alpha_r = \frac{k_g}{r(1 + 3.18\mathrm{Kn})} \tag{12}$$

Or, as seen on Young [1992]:

$$\alpha_r = \frac{k_g}{r\left(1 + 3.78(1-\nu)\frac{\mathrm{Kn}}{\mathrm{Pr}}\right)} \tag{13}$$

Where k_g is the thermal conductivity of steam, Kn is Knudsen number given by $\mathrm{Kn} = \lambda/2r$, and Pr is Prandtl number $\mathrm{Pr} = (c_p \mu)/k_g$. The mean free path of a vapour molecule is given by:

$$\lambda = \frac{1.5\mu\sqrt{RT_g}}{p_g} \tag{14}$$

With μ representing the dynamic viscosity of the steam. The empirical correction factor is:

$$\nu = \frac{RT_s(p_g)}{h_{fg}} \left[\beta - 0.5 - \left(\frac{2-q}{2q}\right)\left(\frac{\gamma+1}{2(\gamma-1)}\right)\left(\frac{RT_s(p_g)}{h_{fg}}\right)\right] \tag{15}$$

Where β is an empirical parameter taking values between 0 and 5.
In order to integrate the growth equation (11), an expression for the liquid temper-

ature is required. An approximation devised by Gyarmathy was used by Bakhtar et al. [2005] in the form:

$$T_l = T_s(p_g) - \Delta T \frac{r_*}{r} \tag{16}$$

Where ΔT is the subcooling. A modified version was used by Young [1992]:

$$T_l = T_g + \frac{\Delta T(1 - r_*/r)}{1 - \nu\delta} \tag{17}$$

Where δ is given by:

$$\delta = \frac{3.78 - \mathrm{Kn/Pr}}{1 + 3.78\mathrm{Kn/Pr}} \tag{18}$$

.2.3 Implementation approaches

Equations 3 and 11 can be integrated with a variety of techniques. The two most successful and commonly employed methods are presented here.

.2.3.1 Lagrangian method

Even though the flow equations are solved in an Eulerian frame, equations 3 and 11 describe changes in a Lagrangian frame of reference, i.e. following the moving droplets (assuming no interphase slip). It seems therefore natural to integrate them along flow streamlines. The original method by Bakhtar et al. [1980] used short local streamline segments, and Young [1982] adopted full length streamlines from inlet to outlet. One advantage of this approach its modularity, i.e. flow and wetness calculations are decoupled; the solver makes available the pressure-time history along streamlines (any flow solver can provide data for this), and this is the only information needed by the *wetness module* which in turn outputs the wetness fraction (the name"black box" used by Guha and Young [1991] renders the idea rather well: pressure-time is the input and wetness the output).
Another advantage is the ability to retain droplet size spectrum, by integrating the equations for different droplet groups arranged by size, should a polydispersed distribution be needed.

.2.3.2 Method of moments

Hill [1965] first proposed a method for computing wetness by adding four equations to be solved simultaneously with the flow equations in the time-marching procedure. These are the first four moments of the droplet size distribution, where the zeroth moment represents the conservation of droplet number, the first the "total radius", the second conservation of liquid surface, and the third the conservation of volume (hence it is proportional to wetness fraction).
Simultaneous integration of the conservation of mass, momentum and energy with the addition of the four moments yields a solution for nucleating two-phase flow. This approach is more elegant than the Lagrangian method, but not as suitable for prediction of droplet size description, even though polydispersed calculations have been carried out with this method by White and Hounslow [2000]. For many applications, however, droplet size information is not needed.

.2.3.3 Choice of method

A more detailed comparison between different approaches in the implementation of droplet nucleation on growth equations can be found in the paper by White [2003].
An initial choice had to be made for the current case between the two methods listed above. The moment method is very attractive due to simplicity, neatness and reduced computational cost. However, it was opted for the Lagrangian approach, because a flow solver was already in place and no significant modification was needed as opposed to the moments method which required the addition of equations in the time marching procedure. This modularity seemed useful also because the wetness module could then be coupled with any other existing solver or inverse design code. Furthermore, possible developments into polydispersed flow raised interest for their novelty in inverse design.

.3 Integration procedure: Lagrangian monodispersed case

Equations (3) and (11) represent the nucleation rate of water clusters and the growth rate of existing droplets in a frame moving with the vapour particles. The integration is therefore performed along streamlines at a finite number of time intervals. In order to perform this discrete integration, the temperature, pressure and droplet spectrum are needed at the beginning of each time increment, and the pressure at the end of the increment is available from the pressure-time history along the streamline. Thus, the key evaluations to be performed by the procedure moving along the streamline are the variation in wetness fraction and the variation in subcooling across each time increment.
In rapid nucleation zones, the variation in wetness comes in the form of growth of existing droplets and nucleation of new clusters, but this is not necessarily always the case.
As the procedure moves along the streamline updating subcooling and wetness, three cases can be encountered, after having evaluated r_* and J at the new location:

1. Dry steam and negligible nucleation (J below a specified limiting value)
2. Wet steam and negligible nucleation
3. Wet steam and nucleation occurring

.3.1 Case 1: Dry non-nucleating

If steam enters the flow passage superheated, condensation might not occur until rapid expansion in the cascade brings the vapour in the subcooled region. Thus, following the variation in pressure experienced by a fluid particle along a streamline, the subcooling needs to be updated at every location. This procedure continues while the vapour remains superheated, or while the nucleation rate J is considered negligible (i.e. below a limiting value).
The subcooling evolution equation used to update the vapour subcooling at each

location on the streamline is a combination of the Lagrangian form of the energy equation:

$$\frac{Dh}{Dt} = \frac{1}{\rho}\frac{Dp}{Dt} \tag{19}$$

With the following standard thermodynamic relationship:

$$dh_g = c_p dT_g + \left(\frac{1 - \alpha_g T_g}{\rho_g}\right) dp \tag{20}$$

Where α_g is the coefficient of thermal expansion of the gas phase. Combining (19) with (20) and defining the subcooling as $\Delta T = T_s - T_g$ yields:

$$\frac{D(\Delta T)}{Dt} = \frac{DT_s}{Dt} - \frac{\alpha_g T_g}{\rho_g c_p}\frac{Dp}{Dt} \tag{21}$$

Therefore, the subcooling can be computed at each time step using the pressure-time history and applying (21) in discrete form.

.3.2 Case 2: Wet non-nucleating

Steam might enter the flow passage already wet but in equilibrium or with values of subcooling too low for new nucleation. Similarly, after rapid condensation has occurred in the cascade, the subcooling of the vapour phase can reduce to negligible values (always measured in terms of nucleation rate J), which means that the mixture is reaching equilibrium.

In the situations above, the subcoolng evolution is obtained by combining the Lagrangian energy equation (19) for the mixture, with (20) and the Clausius Clapeyron equation. This, together with the droplet growth equation, is integrated analytically over small time increments, assuming several properties to be constant (over the small time increment) in non-nulceating flow. This method was suggested by Young [1984], and further details are available in Guha and Young [1991]. The semi-analytical solutions for the subcooling (22) and wetness

(27) at the end of a time increment are:

$$\Delta T = \Delta T_0 e^{-t/\tau} + \tau \left(F\dot{P} + \frac{\Delta T_{cap}}{\tau} \right) (1 - e^{-t/\tau}) \tag{22}$$

Where ΔT_0 is the subcooling at the beginning of the time increment and the pressure gradient is $\dot{P} = D(\ln P)/Dt$. The thermal relaxation time τ is given by:

$$\tau = \frac{(1-y)c_p r^2 \rho_l A}{3k_g y} \tag{23}$$

Where k_g is the thermal conductivity of the gas, and A is given by:

$$A = \frac{1}{1 + 4\mathrm{Kn}} + 3.78(1-\nu)\frac{\mathrm{Kn}}{\mathrm{Pr}} \tag{24}$$

The capillary subcooling ΔT_{cap} is given by:

$$\Delta T_{cap} = \frac{2\sigma T_s}{\rho_l r h_{fg}} \tag{25}$$

And the factor F is given by:

$$F = \frac{p}{(1-y)c_p \rho_s} \left(\frac{cT_s}{h_{fg}} - (1-y)(\alpha_g T_g)\frac{\rho_s}{\rho_g} \right) \tag{26}$$

Where c is the specific heat capacity of the mixture $c = (1-y)c_p + yc_l$. The updated wetness fraction at the end of the increment is:

$$y = y_0 - \frac{(1-y)c_p \Delta T_{cap}}{h_{fg}\tau} t + \frac{(1-y)c_p \tau}{h_{fg}\tau} \cdot \left[(\Delta T_0 - \Delta T) + \left(F\dot{P} + \frac{\Delta T_{cap}}{\tau} \right) t \right] \tag{27}$$

In the case of monodispersed flow, the average radius is then updated using the relation $y = 4\pi r^3 \rho_l N$, assuming constant number of droplets N.

.3.3 Case 3: Wet nucleating

When the subcooling reaches values that yield high nucleation rates, equation (11) needs to be integrated to give the grown radius of the existing droplets, while the nucleation rate (7) is integrated to give the number of new droplets of critical radius r_* nucleated over the time interval, together with an expression for the subcooling evolution. The growth equation and subcooling evolution are rearranged by Guha and Young [1991] in the form:

$$\frac{Dr}{Dt} = \frac{k_g(T_l - T_g)}{r\rho_l A(h_g - h_l)} \tag{28}$$

Where A is given by (24). The subcooling evolution is:

$$\frac{D(\Delta T)}{Dt} = F\frac{D(\ln p)}{Dt} - \frac{(\Delta T - \Delta T_{cap})}{\tau} \tag{29}$$

Where the factor F is given by (26).
Since rapid growth is occurring, vapour properties can not be considered constant across the time increment . Equations (28) and (29) are therefore integrated simultaneously by means of a 4th order Runge Kutta method. This yields a new value of radius for the existing droplets (in case of monodispersed flow, only one droplet group is present), and a value of temperature at the end of the time increment (from the subcooling).
It is assumed that newly nucleated droplets have negligible effect on the change in wetness fraction and subcooling, hence the nucleation rate is integrated separately, and the new droplets are added at the end of the increment. In the monodispersed case this simply means mass averaging existing and new droplets to yield a common average radius.
The number of newly nucleated droplets is found either by assuming constant J at its initial value, or by using an average value across the increment. Young [1992] suggests that for high nucleation zones, a good approximation is that $\ln(J)$ rather than J itself varies linearly with time. In the present case the averaging

takes the form:

$$\bar{J} = \exp\left[0.5 \ln\left(J_{i-1} J_i\right)\right] \tag{30}$$

.4 Problems

The above procedure was implemented in a computer code. Several difficulties were encountered, including the validation and dealing with rotating flows, or complex and highly staggered blade profiles. Furthermore it was realised that the need for streamline tracking would be highly impractical for LSB, especially if a future 3D or multistage development was desired. Also, the cumbersome nature of the Lagrangian approach makes it difficult to create a robust and versatile computational method. The computational cost also revealed to be very high, which is not ideal in an iterative inverse design procedure

A great time fraction of the project was spent developing the computer code for this method, hence the theory and methodology were presented in this chapter for reference. The lack of validation on the results makes them not publishable here.

Further reasons for abandoning the work on the Lagrangian non-equilibrium model were:

- It was realised that the equilibrium model was enough for the LSB under consideration, since the inflow was completely wet and secondary nucleation was considered a negligible aspect by the manufacturer.

- Work was being carried simultaneously on the inverse design methodology; It was discovered that the existing inverse design software could not cope with the LSB geometries. The priority had therefore to shift to the creation of a new inverse design procedure. This had not been foreseen at the start of the project, hence why so much work had been put into the non-equilibrium effects, which can be considered of secondary importance here.

- The need for a new inverse design method eventually required the need for a new solver. This would create an opportunity for the inclusion of the

moments of droplet formation, creating a more elegant solution to the non-equilibrium problem. This method was used in steam turbine analysis by Senoo and White [2012].

The work was thus abandoned, with the idea of coming back to it in case a successful new inverse methodology had been developed and implemented also for the two-phase equilibrium flows. With most probability, the recommended approach would now be the method of moments.

Appendix B: The non-periodic mesh attempt

In order to alleviate the high shear introduced in the mesh at high stagger, a non-periodic mesh was developed, by redistributing the boundary points as shown in figure 1a: A few extra mesh points are added to the lower inlet periodic line, and the same number of points is added to the outlet upper periodic line, so that the total number of streamwise mesh points is the same on upper and lower boundaries, and a H-mesh can be created; the number of points to be added to the lower inlet and upper outlet periodic lines can be specified when generating the mesh. This greatly improves the orthogonality of the mesh (shear is reduced). Some example of meshes are shown in figure 2. However, the solver increases in complexity, as interpolation of the flow variables is now needed at the periodic boundaries. It is clear form figure 1a that one side of the periodic boundary will have a coarser mesh than the other side. In order to impose exactly the same distribution of values of a given variable, the maximum resolution is limited to the coarser mesh. Therefore at each x-coordinate of the coarse side, the value of each variable is interpolated between points on the fine side; the new (coarse) average distribution is then computed. Finally, the values are interpolated back from the coarse average to the fine mesh: resolution is lost, but identical distribution of values is ensured at the boundary. Figure 1b illustrates the interpolation procedure. After running a few simulations at high stagger sections, it was noted that this approach was creating inaccuracies in the solution. Simple interpolation has been successfully implemented before by Arnone et al. [1992]. However, in his

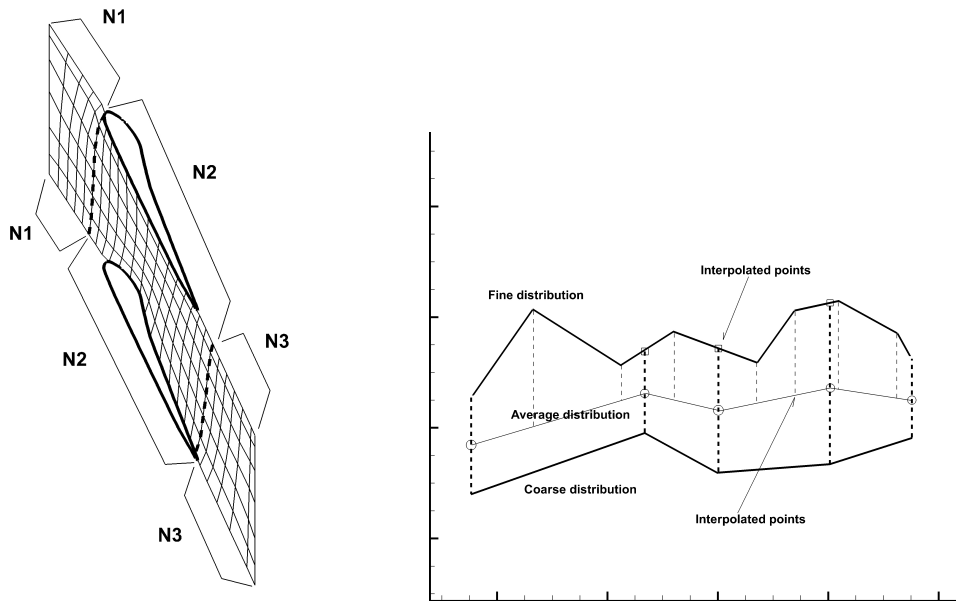

(a) the upper and lower boundary points redistribution

(b) interpolating flow variables at the periodic boundary

Figure 1: Defining the non periodic boundaries

case a C-grid was employed, so that the non-periodicity of the mesh was limited to the outlet region; most importantly, the periodic boundaries were moved as far away (circumferentially) as possible from the wake line and from the shock locations. As mentioned by Arnone, and as observed in the present case, a discontinuity crossing the non-periodic boundary causes errors. The major problem in this case is the unsuitable location of the periodic lines; at the tip, for example, the upstream bow shock location falls across the periodic line. Furthermore, the very high stagger angle does not allow for a C-mesh option similar to the one used by Arnone. The method was thus abandoned, but the incompatibility between periodic boundary interpolation and flow discontinuities is certainly a result of interest.

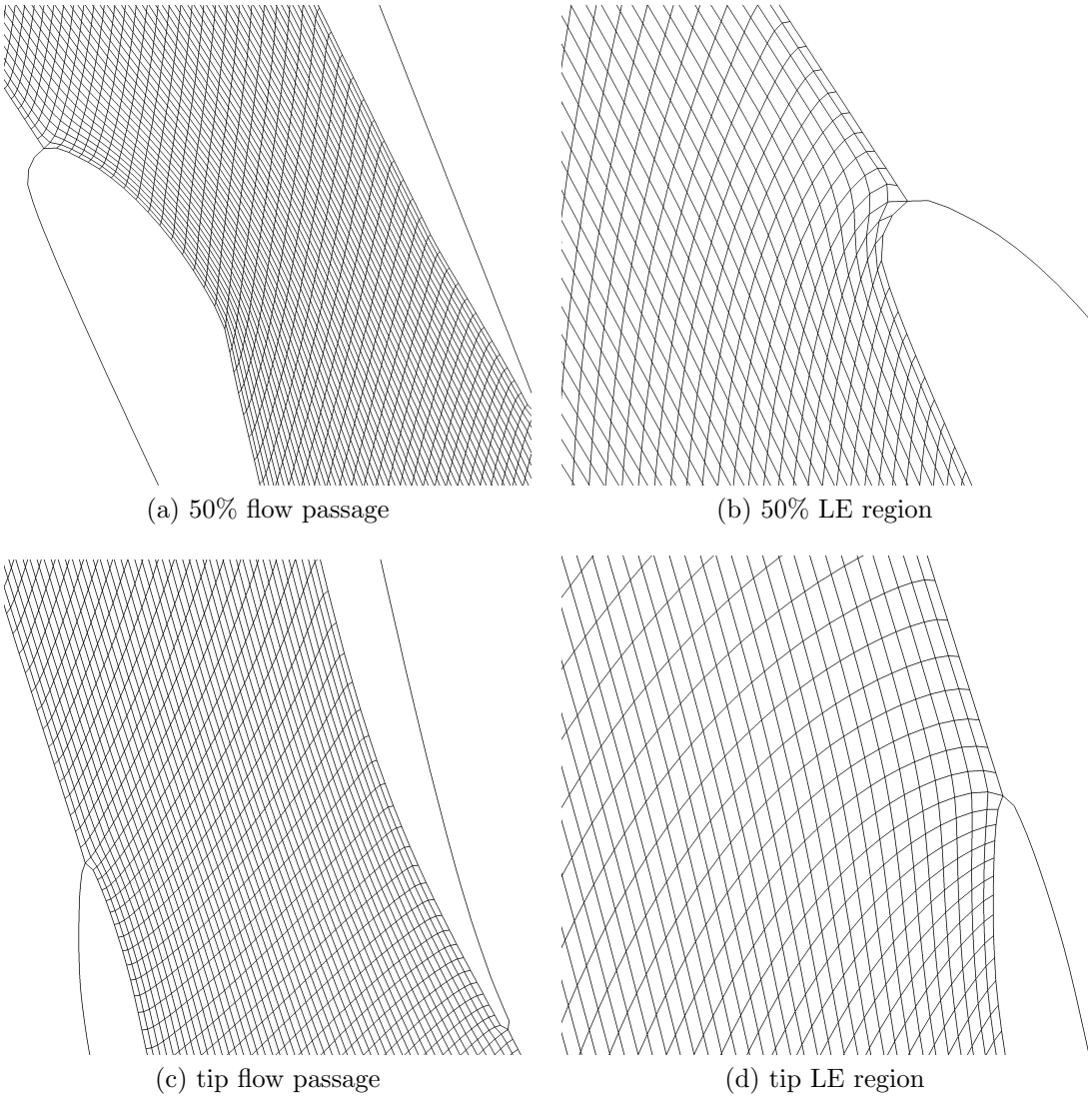

(a) 50% flow passage

(b) 50% LE region

(c) tip flow passage

(d) tip LE region

Figure 2: Defining the non periodic boundaries

Appendix C: Transpirating, Δp based inverse method with normal thickness definition

.5 Blade update formula

The Δp method seemed the appropriate initial choice as no circumferential averaging of rV_θ is necessary (hence no interpolation needed when using arbitrary mesh). This method also avoids having to deal with open or overlapping TE (occurring when prescribing surface static pressure). In the Δp method, the solid wall boundary condition is replaced with a transpirating wall boundary condition (described in section .6). The target Δp is imposed which will result in transpiring fluxes: the relative velocity vectors on the blade surfaces are therefore not tangential to the blade profile until the geometry matches the Δp prescription. The amount of transpiration is used as a measure of the geometrical modification needed. With this in mind, the formula to modify the camber line accordingly is derived as follows. Defining the vector tangential to the blade surface at each point:

$$\mathbf{T} = T_x\hat{\boldsymbol{i}} + T_y\hat{\boldsymbol{j}}$$

The blade surface was described in terms of upper and lower profiles ($\mathbf{r}^+$ and $\mathbf{r}^-$) in (**??**). The tangent to $\mathbf{r}$ will be the derivative with respect to its arc length σ

(which has to be computed from the set of points):

$$\mathbf{T}^{\pm} = \frac{d\mathbf{r}^{\pm}}{d\sigma^{\pm}}$$

Then:

$$\mathbf{T}^{\pm} = \frac{ds}{d\sigma^{\pm}} \left[\frac{d}{ds}(c_x \pm t_x)\hat{\boldsymbol{i}} + \frac{d}{ds}(c_y \pm t_y)\hat{\boldsymbol{j}} \right] \tag{31}$$

The surface velocity, or relative velocity vector is defined as:

$$\mathbf{V}^{\pm} = u^{\pm}\hat{\boldsymbol{i}} + v^{\pm}\hat{\boldsymbol{j}} \tag{32}$$

Then the tangency condition is:

$$|\mathbf{V} \times \mathbf{T}| = 0 \tag{33}$$

This is the starting point of the derivation. Evaluating the cross product:

$$\mathbf{V} \times \mathbf{T} = \begin{vmatrix} \hat{\boldsymbol{i}} & \hat{\boldsymbol{j}} & \hat{\boldsymbol{k}} \\ T_x & T_y & 0 \\ u & v & 0 \end{vmatrix} = \hat{\boldsymbol{k}}(T_x v - T_y u)$$

Hence the tangency condition becomes:

$$T_x v - T_y u = 0 \tag{34}$$

This will be used later when updating the surface velocities after imposing the Δp condition. Now, substituting components of (32) and (31) into (34) yields:

$$\frac{ds}{d\sigma^{\pm}} \left[v^{\pm} \frac{d}{ds}(c_x \pm t_x) - u^{\pm} \frac{d}{ds}(c_y \pm t_y) \right] = 0 \tag{35}$$

This can be rearranged to give an expression for c_y; the axial position c_x of the camber points is kept constant so that the axial chord will not change. Thus,

(35) is written as:

$$\frac{d}{ds}(c_y \pm t_y) = \frac{v^{\pm}}{u^{\pm}}\frac{d}{ds}(c_x \pm t_x)$$

And adding upper and lower surface:

$$2 \cdot \frac{dc_y}{ds} = \frac{v^+}{u^+}\frac{d}{ds}(c_x + t_x) + \frac{v^-}{u^-}\frac{d}{ds}(c_x - t_x) \tag{36}$$

Integrating this expression from a chosen "stacking" point (upstream and downstream of it), gives the updated y coordinates (c_y) of the camber line. Repeated application of (36) will tend to the geometry corresponding to the prescription, by virtue of the fact that the surface velocities are made progressively more tangent to the blade by using (34) to evaluate $v^{\pm}$ at the transpirating wall boundaries.

.6 Transpirating walls

The transpirating wall boundary condition (BC) differs from the solid wall BC as the normal fluxes are not set to zero. Furthermore, the wall pressure is updated so that the required $\Delta p = p^+ - p^-$ is imposed. Here, two different methods of treating this boundary condition are suggested. Before going into the details of these two methods, a few more observations should be made. The pressure jump is $\Delta p = p^+ - p^-$ which, in the current normal thickness definition, uses pressures $p^{\pm}$ on either side of the normal thickness direction. In the tangential thickness definition, the Δp was related directly to torque, because the difference was taken on a line aligned with the circumferential direction. This is not the case for the normal thickness, hence no direct relationship to torque is available. Additionally, since both x and y coordinates of surface points are changing during the blade update (in the tangential method the x-coordinates of the blade points were fixed), the pressure jump will be imposed at slightly different locations during the blade modification. In other words, even if the camber points are kept at the same axial location, the arc length intervals are changing, hence the Δp distribution with respect to arc length is "stretched" as a consequence. However,

as the blade converges to the target, this effect should become negligible.

.6.1 Method of averages

In this approach, the blade average values of a variable are used as a base for imposing the pressure jump or the tangency condition. By blade average value it is intended the average between upper and lower blade surface value of a variable, at a given camber point location. The pressure is therefore updated as:

$$p_{av} \leftarrow \frac{1}{2}\left[(p^+)^* + (p^-)^*\right]$$

$$(p^\pm)^{t+1} \leftarrow p_{av} \pm \frac{1}{2}\Delta p$$

where the $*$ superscript indicates values obtained from the solution of the discretised Euler equations, and the t superscript refers to the time iteration. The surface velocities:

$$(u^\pm)^{t+1} \leftarrow (u^\pm)^*$$

$$v_{av} \leftarrow \frac{1}{2}\left[(v^+)^* + (v^-)^*\right]$$

$$(v^\pm)^{t+\frac{1}{2}} \leftarrow u^\pm \frac{T_y^\pm}{T_x^\pm} \tag{37}$$

$$\Delta v^\pm \leftarrow (v^+)^{t+\frac{1}{2}} - (v^-)^{t+\frac{1}{2}} \tag{38}$$

$$(v^\pm)^{t+1} \leftarrow v_{av} \pm \frac{1}{2}\Delta v^\pm$$

Note that using absolute velocities in (37) is not incorrect (even though equation (34) was derived in relative frame), since the blade rotational speed will cancel out in (38). Additionally, the density can be set to the average value (Dang et al. [2000]):

$$(\rho^\pm)^{t+1} \leftarrow \frac{1}{2}\left[(\rho^+)^* + (\rho^-)^*\right]$$

which can in some cases improve the quality of the transpirating solution. Finally,

the variables depending on p and v need to be updated, namely ρv, e, ρe, h.

.6.2 Method of characteristics

This method was introduced by Leonard and Van den Braembussche [1992], then extended to rotating blades by Demeulenaere and Van den Braembussche [1998] and adapted to Δp prescription by Dang et al. [2000]. The transpirating walls are treated as inflow/outflow boundaries. For relatively small geometry modifications it can be assumed that the normal component w_n of transpiring relative velocity will always be subsonic. Therefore, the eigenvalue $w_n + a$ will correspond to a wave propagating out of the domain (a is speed of sound), and $w_n - a$ to a wave propagating in the domain (normal direction is positive going out of the domain). Thus, one boundary condition is always imposed (for the negative eigenvalue $w_n - a$), namely the pressure jump prescription. For the positive eigenvalue no condition is imposed, but the corresponding compatibility relation must be satisfied:

$$(C^{\pm})^{t+1} = (C^{\pm})^{*} \tag{39}$$

Where the characteristic C is:

$$C = \rho a w_n + p \tag{40}$$

Subtracting the lower surface equation from the upper in (39) gives:

$$(C^{+})^{t+1} - (C^{-})^{t+1} = (C^{+})^{*} - (C^{-})^{*} \tag{41}$$

which can be expanded introducing (40), and with the assumption (Dang et al. [2000]) that the normal velocities on upper and lower surfaces are equal (at given camber point location):

$$w_n^{+} = w_n^{-} \equiv w_n$$

Then (41) becomes:

$$(w_n)^{t+1}(\rho^+ c^+ + \rho^- c^-) = -\Delta p^{t+1} + (C^+)^* - (C^-)^* \tag{42}$$

where Δp^{t+1} is the prescribed Δp, and all the other variables are taken from the latest Euler solution (the asterisk also indicates latest solution, but for a variable that needs to be updated). Equation (42) is used to update the normal velocities w_n. These in turn are used to compute $p^{\pm}$ from (40). Having new values of static pressure allows the evaluation of the temperature and tangential (to wall) velocity component from standard isentropic relationships. Once again, all remaining variables dependent upon pressure and velocity need to be updated at the end of the above procedure.

.7 Inverse design implementation and problems

.7.1 Summary of strategy

The key components in the inverse design strategy are:

- **The Euler solver** with transpirating wall boundary conditions: this computes the flow solution and gives the transpiring velocities at the walls when the geometry does not match the pressure jump prescription.
- **The blade update algorithm** modifies the blade camber by using information from the transpiring velocities.
- **The re-meshing routine**, capable of reconstructing the blade by imposing the specified normal thickness, and subsequently creating a new mesh for the Euler solver.

The strategy includes the following steps:

1. Mesh generation
2. Computation of vectors normal and tangential to blade surface

3. Initial conditions evaluation (1^{st} run) or initialization from file (successive runs)

4. Euler solution with transpirating walls (converged solution then stored to file)

5. Camber update

6. Blade reconstruction

7. Remeshing and back to step 2, for a specified number of loops

.7.2 Test cases: blade recovery

In blade recovery, the original blade profile is modified arbitrarily, and then a test inverse design is run by imposing the original Δp distribution. Under ideal circumstances, this should result in the original blade being recovered. The convergence of the Euler solver during design was set to reach a good proportion of the fully converged solution, in order to minimise the number of calls to the re-meshing routine. An alternative approach would be to update the blade every few time steps, so that the geometry is modified gradually during convergence. The high computational cost of the discrete solution of the elliptic equations governing the mesh makes this second choice not of practical interest.
The blade recovery was tested at different sections, but an optimum set up has not been achieved. As can be observed from figure 3a and 3b, the first few iterations rapidly bring the blade very close to the target (green). However, once the blade profile is close to target, small oscillations start occurring, which can result in either some error being introduced (and possibly lack of convergence) or convergence to an offset blade geometry. This seems to be caused by the misalignment of the blade surface velocities with the tangent to the blade profile, even when the geometry is close to target. This suggests some possible problems with the transpirating models. The most notable issues are the lack of convergence of the characteristic based transpirating model at the hub section (perhaps due to the assumption made by Dang et al. [2000] of equal normal velocities on upper and lower profiles, which might give problems with high curvatures), and the

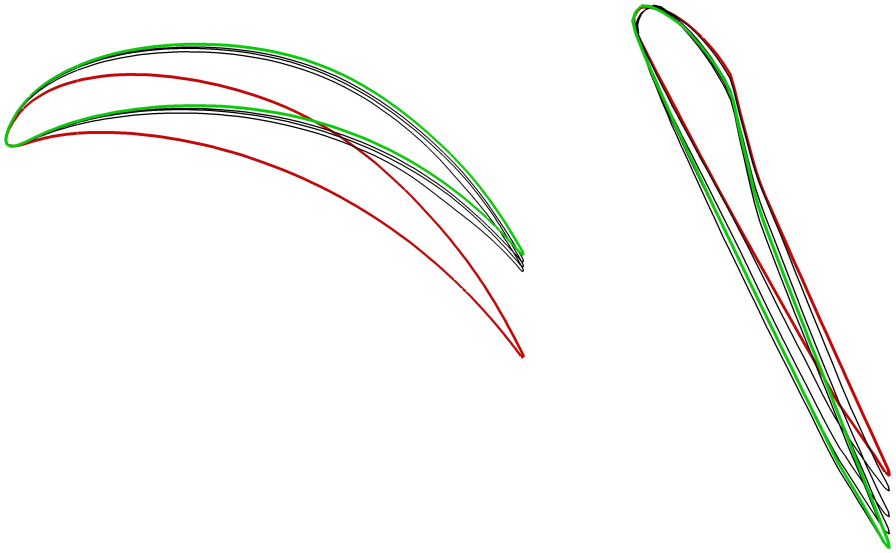

(a) hub (b) 50% span

Figure 3: Original (green), modified (red), and few intermediate geometries (black) of blade recovery

presence of singular discontinuities in the surface velocity vectors at high stagger, usually in correspondence to some decambering or high pressure gradients. Other hypotheses on factors influencing the inaccuracy of the design procedure are:

- The current Δp is specified in the camber normal direction, so having no direct correlation with the work output might affect the physics of the transpirating solution
- The Δp is imposed at each camber point according to index, rather than at a fixed axial position (even though the camber points have fixed axial position, the blade profile points do not) ; this, however, should not have a major effect since the average axial position of the blade profile points is conserved.
- The methods used to treat transpirating walls might be inaccurate when using normal thickness definition, as they were presented originally (Dang and Isgro [1995], Dang et al. [2000], Tiow [2000], Tiow and Zangeneh [2000]) for tangential thickness. Some assumptions made by those authors such as

equal normal transpiring velocity on pressure and suction surface points corresponding to a given camber point (Dang et al. [2000]), are not justified in a physical way, but were made by the authors for convenience of the derivation. The fact that these assumptions worked in the tangential specification does not guarantee their suitability for the current case.

- A final note is made on the LE reconstruction method: LE regions are not modified by the blade update; instead, the short portion of LE camber is extrapolated as a straight line, and the original normal thickness is imposed. This can result in inaccuracies, as some differences are introduced in the flow solution. Discrepancies in LE shape can be observed in figure 3b.

.8 Problems of transpiration method

As noted in the previous section, one of the main concerns with the transpiration model is the reliance on very accurate capturing of transpirating fluxes.
A simple test was performed whereby a blade profile was analysed, and then its measured pressure jump Δp was imposed as target in the inverse design procedure. This should have resulted in zero transpirating normal fluxes at the walls, hence no camber modification. However, some changes occurred in the blade. Further investigation revealed that a very small normal flux component was still present at the walls, which was picked up by the sensitive blade update algorithm. At first, few considerations were made on the possible causes of this related to the imposition of the permeable wall boundary condition. Tests conducted with solid wall boundary condition showed that at the walls the slip condition (imposed during the all round-flux computation by setting normal wall mass fluxes to zero) resulted automatically in tangential vectors. However, the inaccuracy of the numerical solution resulted in a in-exact alignment between the wall velocities and the direction tangential to the profile. This inaccuracy is inherent to the discretised numerical scheme, and it is usually negligible under an analysis viewpoint, but it becomes relevant when considering the blade update algorithm. Trying to fix the problem by imposing tangency would not work in the Δp method, as this relies on the existence of the normal transpirating fluxes. Also, a cut-off

normal flux magnitude was considered: negligible fluxes were set to zero, in order to avoid unnecessary blade modifications. This method, however, did not lead to the required loading prescription, as it is not possible to assess whether the normal flux is due to numerical errors or due to the permeable wall condition. Thus, even though the newly devised transpiration based update algorithm effectively modified the blade towards the target in very few iterations, the presence of small normal fluxes also when the geometry was essentially coinciding with the target resulted in unwanted further modifications. This possibly leads to eventual divergence due to growing fluxes with advancing time step (especially at high-curvature profiles), or convergence to a slightly offset blade, which in the case of transonic sections is not acceptable due to the extreme sensitivity of transonic flows to small geometric modifications.

References

S. Abraham, K. Panchal, S.V. Ekkad, and W. Ng. Measurement of aerodynamic losses for turbine airfoil cascades with varying pitch, operating under transonic conditions. In *Proceedings of ASME Turbo Expo 2012*, 2012. 13

D.G. Ainley and G.C.R. Mathieson. An examination of the flow in blade rows of axial flow turbines, 1955. Aeronautical research council reports and memoranda 2891. 11

P. Amtsfeld, M. Lockan, D. Bestle, and M. Meyer. Accelerated 3d aerodynamic optimization of gas turbine blades. In *Proceedings of ASME Turbo Expo 2014*, 2014. 17

A. Arbabi and W. Ghaly. Inverse design of turbie and compressor stages using a commercial cfd program. In *Proceedings of ASME Turbo Expo 2013*, 2013. 27, 28

A. Arnone, M.S. Liou, and L.A. Povinelli. Navier-stokes solution of transonic cascade flows using nonperiodic c-type grids. *Journal of Propulsion and Power*, 8(2):410–417, 1992. 179

A. Ashgar, W.D.E Allan, M. LaViolette, and R. Woodason. Influence of a novel 3d leading edge geometry on the aerodynamic performance of low pressure turbine blade cascade vanes. In *Proceedings of ASME Turbo Expo 2014: Turbine Technical Conference and Exposition*, 2014. 10

F. Bakhtar, F. Mohammadi, and M.T. Tochai. An investigation of two-

dimensional flows of nucleating and wet steam by the time-marching method. *Int. Journal of Heat and Fluid flow*, 2:5–18, 1980. 169, 171

F. Bakhtar, A.J. White, and H. Mashmoushy. Theoretical treatments of two-dimensional two-phase flows of steam and comparison with cascade measurements. In *Proc. IMechE vol.219 Part C: Mechanical Engineering Science*, 2005. 170, 171

F. Bertini, M. Credi, M. Marconcini, and M. Giovannini. A path towards the aerodynamic robust design of low pressure turbines. In *Proceedings of ASME Turbo Expo 2012*, 2012. 23

A.M. Binnie and J.R. Green. An electrical detector of condensation in high velocity steam. *R. SOc. Phil. Tran.: Mathematical, Physical and Engineering Sciences*, 354(1704):59–88, 1942. x, 61, 62

J. E. Borges. *Three-dimensional design of turbo-machinery*. PhD thesis, Cambridge university, 1986. 25

P. Boselli and M. Zangeneh. An inverse design based methodology for rapid 3d multi-objective/multidisciplinary optimization of axial turbines. In *Proceedings of ASME Turbo Expo 2011: Power for Land, Sea and Air, Vancouver, Canada*, 2011. 22, 25

J. Burman. *Geometry parameterisation and responce surface-based optimization of aero-engine compressors*. PhD thesis, Lulea University if Technology, 2003. 19

B. Chen and X. Yuan. Advanced aerodynamic optimization system for turbomachinery. *ASME Journal of Turbomachinery*, 130(2), 2008. 21

R. Corral and G. Pastor. Parametric design study of turbomachinery airfoils using highly differentiable splines. *Journal of Propulsion and Power*, 20(2): 335–343, 2004. 19

D. Corriveau and S.A. Sjolander. Influence of loading distribution on the performance of transonic hp turbine blades. *ASME Journal of Turbomachinery*, 126: 288–296, 2004. 13

W.G. Courtney. Remarks on homogeneous nucleation. *Journal of Chemichal Physics*, 35:2249–2250, 1961. 169

T. Dang and V. Isgro. Euler-based inverse method for turbomachine blades part 1: Two-dimensional cascades. *AIAA journal*, 33(12):2309–2315, 1995. 28, 189

T. Dang, S. Damle, and X. Qiu. Euler-based inverse method for turbomachine blades part2: Three-dimensional flows. *AIAA journal*, 38(11):2007–2013, 2000. 27, 86, 185, 186, 188, 189, 190

A. Demeulenaere and R. Van den Braembussche. Three-dimensional inverse method for turbomachinery blading desing. *ASME Journal of Turbomachinery*, 120:247–255, 1998. 26, 27, 186

B. H. Dennis, I. N. Egorov, Z.X. Han, G.S. Dulikravich, and C. Poloni. Multi-objective optimization of turbomachinery cascades for minimum loss, maximum loading, and maximum gap-to-chord ratio. In *AIAA/NASA/USAF/ISSMO Symposium on Multidisciplinary Analysis and Optimization, Long Beach, CA*, 2000. AIAA paper 2000-4876. 21

J. D. Denton. Loss mechanisms in turbomachines. *ASME Journal of Turbomachinery*, 115:621–656, 1993. 13, 20

J. D. Denton, , and N. Cumpsty. Loss mechanisms in turbomachines. In *Proceedings of the IMechE Conference on Turbomachinery Efficiency and Improvement*, 1987. IMechE Paper No. C260/87. 20

Joslyin H.D. Hardin L.W. Dring, R.P. and J.H. Wagner. Turbine rotor-stator interaction, 1982. ASME paper 82-GT-3. 45

R. Fox, P. J. Pritchard, and A. T. McDonald. *Introduction to fluid mechanics*. John Wiley and Sons Inc., New York, 7th edition edition, 2009. 20

D. Grossmann and B. Juttler. *Volumetric Geometry Reconstruction of Turbine Blades for Aircraft Engines*, pages 280–295. Springer-Verlag, 2012. 95

A. Guha and J. B. Young. Time-marching prediction of unsteady condensation phenomena due to supercritical heat addition. In *Proc. of I.Mech.E. Turbomachinery: Latest developments in a changing scene, London*, 1991. Pages 167-177. 171, 174, 176

M. Hasenjager, B. Sendhoff, T. Sonoda, and T. Arida. Three dimensional aerodynamic optimization for an ultra-low aspect ratio transonic turbine stator blade. In *Proceedings of ASME Turbo Expo 2005: Power for Land, Sea and Air, Reno-Tahow, Nevada, USA*, 2005. 21

S. Havakechian and J. Denton. 3d blade stacking strategies and understanding of flow physics in low pressure steam turbines part i - 3d stacking mechanisms. In *Proceedings of ASME Turbo Expo 2015*, 2015. 16, 17

W. R. Hawthorne and C. S. Tan. Design of turbo-machinery blading in 3d flow by the circulation method: a progress report. *ICIDES-II*, pages 354–361, 1987. 25

W.R. Hawthorne, C. Wang, C.S. Tan, and J.E. McCune. Theory of blade design for large deflections: Part 1 two dimensional cascade. *ASME Journal of Engineering for Gas Turbines and Power*, 106:346–353, 1984. 25, 66

P.G. Hill. Condensation of water vapour during supersonic expansion in nozzles. *Journal of Fluid Mehcanics*, 25(3):593–620, 1965. 172

P.G. Hill. A unified fundamental equation for the thermodynamic properties of H2O. *J. Phys. Chem. Ref. Data*, 19(5):1233–1274, 1990. 50

P.G. Hill, K. Miyagawa, and J.D. Denton. Fast and accurate inclusion of steam properties in two- and three-dimensional steam turbine flow calculations. In *Proc. IMechE vol.214 Part C: Mechanical Engineering Science*, 2000. 14, 57, 60

D.G. Holmes and S.S. Tong. A three-dimensional Euler solver for turbomachinery blade rows. *ASME Journal of Engineering for Gas Turbines and Power*, 107: 258–264, 1985. 36

J. H. Horlock. *Axial Flow Turbines: Fuid Mechanics and Thermodynamics*. Butterworths, London, 1966. 20

IF97. *Revised release on the IAPWS Industrial Formulation 1997 for the thermodynamic properties of water and steam*. International Association for the Properties of Water and Steam, 2007. www.iapws.org. ix, xvi, 50, 51

R. Jackson and B.J. Davidson. An equation set for non equilibrium two phase flow, and an analysis of some aspects of choking, acoustic propagation, and losses in low pressure wet steam. *Int. Journal of Multiphase flow*, 9:491–510, 1983. 169

A. Jameson, W. Schmidt, and E. Turkel. Numerical solution of the Euler equations by finite volume methods using Runge-Kutta time-stepping schemes. In *AIAA Fluid and Plasma Dynamics Conference Palo Alto, CA, June 23-25, 1981*, 1981. 32, 34, 35, 38, 39, 40

A. Kantrowitz. Nucleation in very rapid vapour expansion. *Journal of Chemichal Physics*, 19:1097–1100, 1951. 169

R. Kiok, F. Lenthaus, N.C. Baines, and C.H. Sieverding. The transonic flow through a plane turbine cascade as measured in four European wind tunnels. *ASME Journal of Engineering for Gas Turbines and Power*, 108:277–284, 1986. 44, 111

T. Korakianitis. Prescribed-curvature-distribution airfoils for the preliminary geometric design of axial turbo-machinery cacades. *ASME Journal of Turbomachinery*, 115:325–333, 1993. 19

K. Kosowski and C. Tucki. Application of artificial neural networks in investigations of steam turbine cascades. *ASME Journal of Turbomachinery*, 132, 2010. 22

D. T. Lee. Medial axis transformation of a planar shape. *IEEE transactions on pattern analysis and machine intelligence*, PAMI-4(4):363–369, 1982. 95

O. Leonard and R. Van den Braembussche. Design method for subsonic and transonic cascade with prescribed Mach number distribution. *ASME Journal of Turbomachinery*, 114:553–560, 1992. 26, 27, 186

M.J. Lighthill. A new method of two dimensional aerodynamics design. *Aeronautical Research Council*, 1945. London Reports and Memoranda 2112. 24

J. Lu, C. Zhang, and Z. Feng. Aerodynamic optimization and inverse design of 2d and 3d turbine cascades using the discrete adjoint method. In *Proceedings of ASME Turbo Expo 2013*, 2013. 22

R.W. MacCormack and A.J. Paullay. Computational efficiency achieved by time-splitting of finite-difference operators. In *10th Aerospace Sciences Meeting, San Diego, CA, January 17-19, 1972*, 1972. AIAA Paper 72-154. 34

P.W. McDonald. The computation of transonic flow through two-dimensional gas turbine cascades, 1971. ASME paper 71-GT-89. 34

A. J. Medd, T. Q. Dang, and Larosiliere L. M. 3d inverse design loading strategy for transonic axial compressor blading. In *Proceedings of ASME Turbo Expo 2003*, 2003. 27

A.J. Medd. *Enhanced inverse design code and development of design strategies for transonic compressor blading*. PhD thesis, Syracuse University, 2002. 27, 30, 86, 95

K. Miki, A. Subramaniyan, M. Pai, and P. Balasubramanyam. Probabilistic oprimization of two-phase flow using bayesian models. In *Proceedings of ASME Turbo Expo 2014*, 2014. 23

M. Moore and C.H. Sieverding. *Aerothermodynamics of low pressure steam turbines and condensers*. Hemisphere Publishing Corporation, 1987. 12

M. Nakamura. A method for obtaining shockless transonic flows past two-dimensional airfoils whose profiles are partially modified from a given arbitrary profile. *Trans. Japan Soc. Aero. Space Sci*, 23(62):195–213, 1981. 24

A. F. Nemnem, M. G. Turner, K. Siddappaji, and G. Marhsall. A smooth curvature-defined meanline section option for a general turbomachinery geometry generator. In *Proceedings of ASME Turbo Expo 2014*, 2014. 19

G.Y. Nieuwland. Transonic potential flow around a family of quasi-elliptical aerofoil sections, 1967. National Aerospace Laboratory report NLR-TR-T172. 24

O. Oksuz and I. S. Akmandor. Advanced aerodynamic optimization system for turbomachinery. *ASME Journal of Turbomachinery*, 132:041009.1–041009.14, 2010. 21

H. Ono, S. Senoo, T. Kudo, and K. Murata. The effects of the tangential leans for the last stage nozzles of steam turbine. In *Proceedings of ASME Turbo Expo 2013: Turbine Technical Conference and Exposition, San Antonio, Texas, USA*, 2013. 13

A. Oyama, M. Liou, and S. Obayashy. Transonic axial-flow blade shape optimization using evolutionary algorithm and three-dimensional navier-stokes solver. In *AIAA/ISSMO Symposium on Multidisciplinary Analysis and Optimization, Atlanta, GA*, 2002. AIAA Paper 2002-5642. 21

J. H. Page, O. Hield, and P. G. Tucker. Inverse design of 3d multi-stage transonic fans at dual operating points. In *Proceedings of ASME Turbo Expo 2013*, 2013. 27, 28

M. Parvizinia, C. Berlich, F. Truckenmller, and H. Ster. Numerical and experimental investigations into the aerodynamic performance of a supersonic turbine blade profile. In *Proceedings of ASME Turbo Expo 2004: Power for Land, Sea and Air, Vienna, Austria*, 2004. 12

M. Pini, G. Persico, and V. Dossena. Robust adjoint-based shape optimization of supersonic turbomachinery cascades. In *Proceedings of ASME Turbo Expo 2014*, 2014. 22

I. Popovic, J. Zhu, W. Dai, S.A. Sjolander, T. Praisner, and E. Grover. Aerodynamics of a family of three highly loaded low-pressure turbine airfoils: mea-

sured effects of reynolds number and turbulence intensity in steady flow. In *Proceedings of ASME Turbo Expo 2006*, 2006. 13

C. Prakash, D.G. Cherry, H.W. Shin, J. Machnaim, L. Dailey, R. Beacock, D. Hlastead, A.R. Wadia, S. Guillot, and W.F. Ng. Effects of loading level and distribution on lpt losses. In *Proceedings of ASME Turbo Expo 2008*, 2008. 13

L.J. Pritchard. An eleven parameter axial turbine airfoil geometry model, 1985. ASME paper 85-GT-219. 18

J. H. Rogers and Y.R. Mayhew. Thermodynamic and transport properties of fluids, fifth edition, 1995. Blackwell Publishing. 58

D. Schrack, M. Schneider, M. Fraas, M.G. Rose, and S. Staudacher. Unsteady secondary flow in a low pressure turbine with integrated 3d design. In *Proceedings of ASME Turbo Expo 2013*, 2013. 14

S. Senoo and H. Ono. Development of design method for supersonic turbine aerofoils near the tip of long blades in steam turbines part 2: Configuration details and validation. In *Proceedings of ASME Turbo Expo 2013: Turbine Technical Conference and Exposition, San Antonio, Texas, USA*, 2013. 13, 22, 130, 148

S. Senoo and A.J. White. Non-equilibrium unsteady wet-steam condensation modelling: Computations for a steam turbine cascade and a nozzle, 2012. Presented at the Baumann Centenary Conference, September 2012, Cambridge, UK. 178

S. Senoo, K. Ogata, T. Nakamura, and N. Shibashita. Three-dimensional design method for long blades of steam turbines using fourth-degree nurbs surface. In *Proceedings of ASME Turbo Expo 2010: Power for Land, Sea and Air, Glasgow, UK*, 2010. 22, 130

S. Senoo, K. Sakakibara, T. Kudo, and N. Shibashita. A numerical method for turbulent flows in highly staggered and low solididty supersonic turbine

cascades. In *Proceedings of ASME Turbo Expo 2011: Power for Land, Sea and Air, Vancouver, Canada*, 2011. 12, 130

K. Siddappaji, M. G. Turner, and A. Merchant. General capability of parametric 3d blade design tool for turbomachinery. In *Proceedings of ASME Turbo Expo 2012*, 2012. 19

D. Simurda, M. Luxa, P. Safarik, J. Synac, and M. St'astny. Aerodynamic investigations of root sections of long rotor blades applied at the last stages of steam turbines. In *Proceedings of ASME Turbo Expo 2012*, 2012. 12

H. Sobieczky, N.J. Yu, K.Y. Fung, and A.R. Seebass. New method for designing shock-free transonic configurations. *AIAA journal*, 17(7):722–729, 1978. 24

T. Sonoda, T. Arima, M. Olhofer, B. Sendhoff, F. Kost, and P.A. Giess. A study of advanced high-loaded transonic trubine airfoils. *ASME Journal of Turbomachinery*, 128:650–657, 2006. 21

R.L. Sorenson. A computer program to generate two-dimensional grids about airfoils and other shapes by the use of poisson's equation, 1980. NASA Technical Memorandum, Technical Paper N80-26266. 102

M. Stanciou, M. Marcelet, and J.-M. Dorey. Numerical investigation of condenser pressure effect on last stage operation of low pressure wet steam turbines. In *Proceedings of ASME Turbo Expo 2013: Turbine Technical Conference and Exposition, San Antonio, Texas, USA*, 2013. 9

J.D. Stanitz. General design method for three dimensional channels with prescribed velocity along the channel walls, 1953. NACA report No.1115. 24

J. Starzmann, M. Casey, and F. Sieverding. Non-equilibrium condensation effects on the flow field and the performance of a low pressure steam turbine. In *Proceedings of ASME Turbo Expo 2010: Power for Land, Sea and Air, Glasgow, UK*, 2010. 15

J.L. Steger and R.L. Sorenson. Automatic mesh-point clustering near a boundary in grid generation with elliptic partial differential equations. *Journal of Computational Physics*, 33:405–410, 1979. 101, 102, 107

A. Stein, D. Hofer, J. Filippenko, and J. Slepski. Aerodynamic design of transonic tip sections. In *Proceedings of ASME Turbo Expo 2010: Power for Land, Sea and Air, Glasgow, UK*, 2010. 10

H.J. Stetter. *Analysis of discretization methods for ordinary differential equations*, volume 23 of *Tracts in Natural Phylosophy*. Springer-Verlag, New York, 1973. 39

W.T. Tiow. *Inverse design of turbomachinery blades in rotational flow*. PhD thesis, University College London, 2000. 66, 189

W.T. Tiow and M. Zangeneh. A three-dimensional viscous transonic inverse method. In *Proceedings of ASME Turbo Expo 2000, Munich, Germany*, 2000. Paper 2000-GT-0525. 28, 32, 66, 85, 189

J. W. Van Den Burg, J. G. M. Kuerten, and P. J. Zandbergen. Improved shock-capturing of jamesons scheme for the euler equations. *Int. Journal for Numerical Methods in Fluids*, 15:649–671, 1992. 110

M. Van Rojii and A. Medd. Reformulation of a three-dimensional inverse design method for application in a high-fidelity cfd environment. In *Proceedings of ASME Turbo Expo 2012*, 2012. 27, 28

R. Vazquez and D. Torre. The effect of mach number on the loss generation of lp turbines. In *Proceedings of ASME Turbo Expo 2012*, 2012. 13

R.J Volino. Effects of endwall boundary layer thickness and blade tip geometry on flow through high pressure turbine passages. In *Proceedings of ASME Turbo Expo 2014*, 2014. 14

B. Walther and S. Nadarajah. Constrained adjoint-based aerodynamic shape optimization of a single stage transonic compressor. In *Proceedings of ASME Turbo Expo 2012*, 2012. 22

P. Wang and M. Zangeneh. Aerodynamic and aeroacustic optimization of a transonic centrifugal compressor. In *Proceedings of ASME Turbo Expo 2014: Turbine Technical Conference and Exposition*, 2014. 22, 25

A.J. White. A comparison of modelling methods for polydispersed wet-steam flow. *International Journal for Numerical Methods in Engineering*, 57:819–834, 2003. 14, 172

A.J. White and M.J. Hounslow. Modelling droplet size distributions in polydispersed wet steam flows. *Int. Journal of heat and mass transfer*, 43:1873–1884, 2000. 172

J. B. Young. The spontanous condensation of steam in supersonic nozzles. *PhysicoChemical Hydrodynamics*, 3(1):57–82, 1982. 171

J. B. Young. Semi analytical techniques for investigating thermal non-equilibrium effects in wet steam turbines. *Int. Journal of Heat and Fluid flow*, 5(1):57, 1984. 174

J.B. Young. Two-dimensional, nonequilibrium, wet-steam calculations for nozzles and turbine cascades. *ASME Journal of Turbomachinery*, 114:569–579, 1992. 169, 170, 171, 176

X. Yuan, T. Tanuma, X. Zhu, Z. Lin, and D. Nomura. A cfd approach to fluid dynamic optimum design of steam turbine stages with stator and rotor blades. In *Proceedings of ASME Turbo Expo 2010*, 2010. 22

M. Zangeneh. *Three-dimensional design of radial inflow turbines*. PhD thesis, Cambridge university, 1988. 25

M. Zangeneh. A compressible three-dimensional design method for radial and mixed flow turbomachinery blades. *Int. Journal of Numerical Methods in Fluids*, 13:599–624, 1991. 25, 66

M. Zangeneh, B. DaCosta, and K. Dakeshkahna. Multi-objective automatic optimization strategy for design of waterjet pumps, 2008. Presented at the RINA Waterjet Propulsion Conference, December 2008, London. 22, 25

M. Zangeneh, Daneshkhah K. Amarel, N., and Krain. Optimization of 6.2:1 pressure ratio centrifugal compressor impeller by 3d inverse design. In *Proceedings of ASME Turbo Expo 2011: Power for Land, Sea and Air, Vancouver, Canada*, 2011. 25

T. Zoric, I. Popovic, T. Praisner, S.A. Sjolander, and E. Grover. Comparative investigation of three highly loaded lp turbine lp airfoils: Part i - measured profile and secondary losses at design incidence. In *Proceedings of ASME Turbo Expo 2007*, 2007. 13